Quantum Dot Photonics

by

Laura A. Kinnischtzke

Submitted in Partial Fulfillment of the

Requirements for the Degree

Doctor of Philosophy

Supervised by Professor A. Nick Vamivakas

Department of Physics and Astronomy
Arts, Sciences, and Engineering
School of Arts and Sciences

University of Rochester
Rochester, New York

2017

to jj

always with me

always with you

Table of Contents

Biographical Sketch

Laura Ann Kinnischtzke was born in Bismarck, ND. She attended the University of Minnesota in Minneapolis, graduating in May 2011 with a Bachelor of Science in Physics, and a minor in mathematics. During her undergraduate studies, she was awarded an Undergraduate Research Opportunity to study the capacitance of ionic liquids with Professor Allan Goldman. She began her graduate studies at the University of Rochester in Fall 2011. A year into the PhD program in Physics, she joined the burgeoning group of a new faculty member at The Institute of Optics - Professor Nick Vamivakas. This group started with a modest vision to study light-matter interactions in zero-dimensional quantum dots, and this thesis is the result of much of this foundational effort. She received a Masters of Arts degree in Physics from the University of Rochester in 2013, and was awarded a Cold Science Exploration award from Montana Instruments Corporation in 2017 for her work in quantum dot sensing.

Publications

1. **Graphene mediated Stark shifting of quantum dot energy levels**
   Laura Kinnischtzke, Kenneth Goodfellow, Chitraleema Chakraborty, YiMing Lai, Antonio Badolato, Stefan Falt, Werner Wegscheider, and Nick Vamivakas. *Applied Physics Letters* **108**, 211905 (2016).

2. **Voltage-controlled quantum light from an atomically thin semiconductor**

   Chitraleema Chakraborty, Laura Kinnischtzke, Kenneth M. Goodfellow, Ryan Beams, and A.N. Vamivakas, *Nature Nanotechnology* **10**, 507-511 (2015).

Conference Proceedings

1. **Imaging Potential Energy Landscapes with Quantum Dots**

   Laura Kinnischtzke and Nick Vamivakas *American Physical Society (APS) March Meeting, New Orleans, LA* (March 2017)

2. **Graphene-based electrostatic control of InAs quantum dots**

   Laura Kinnischtzke, Kenneth Goodfellow, Chitraleema Chakraborty, YiMing Lai, Antonio Badolato, Stefan Falt, Werner Wegscheider, and Nick Vamivakas *Optical Society of America (OSA) Frontiers in Optics/Laser Science, Rochester, NY* (October 2016)

3. **Magneto-photoluminesence study of InAs quantum dots emitting at 1150 nm**

   Laura Kinnischtzke, Yi-Ming Lai, Tanya Malhotra, Nick Vamivakas, and Antonio Badolato *APS March Meeting, San Antonio, TX* (March 2015)

Acknowledgments

Jack O'Neill: Something wrong?
Samantha Carter: No. I've just never blown up a star before.
Jack: Well, they say the first one's always the hardest.

Stargate SG-1

Thank you to my committee - Judy, Miguel, Nick Bigelow and Nick Vamivakas - for taking the time to read this thesis and prepare meaningful feedback. Additionally, I'm very much indebted to a number of faculty members for their care in lectures, and availability outside the classroom - Carlos Stroud, Joe Eberly, Ashok Das, Andrew Jordan, Steve Teitel and Antonio Badolato.

Of course this thesis is largely shaped by my adviser, Nick Vamivakas. In being the first crop of students through his experimental optics lab, I have experienced an interesting mix of setting up the costly, shiny new equipment and scrounging through retired lab setups (mostly from Nick George and Carlos Stroud's equipment) to make the experiments possible. Along the way, I managed to assemble a diverse set of skills and self-reflections in addition to producing a little physics. Thanks Nick!

The work of being a graduate student is a burden greatly eased by generous and caring staff. Laura Blumkin is a paperwork wizard, half-time counselor/coach, and

next to Nick V., the most influential person in getting me to the stage of this thesis. In addition, Rich and Dave in the computing center always have an open door, Lori Russell, Nolene Votens and Adrienne Snopowski have been invaluable in running the Wilmot Labs. Jim Mitchell and Alex Mann have always kept the cleanroom in good working order and been there to help calm my fears about whatever scheme I am about to execute. Per Adamson and Brian McIntyre deserve so much more than just a sentence in this thesis - but next to Nick and my labmates, I have learned the most about optics and nano-fab from the two of you.

I have learned much of my lab skills from those around me - for this I want to thank Ryan Beams, Tanya Malhotra, Chitraleema Chakraborty, and Levi Neukirch. In addition, the (extended) group members have made the Vamivakas Group an exciting place to work - including Kenny Goodfellow, Robby Petit, Steve Person, Dallas Smith, XiaoFeng Quian, Sajal Dhara, Alex Kitt, and Necdet Basran. For the incoming students, I trust we have collectively laid the groundwork for your projects to accelerate through what were growing pains for us.

I've been fortunate enough to discover Rochester through the eyes of many fellow graduate students. Starting with a wonderful set of roommates for a first year student, David and Sarah Starling and Amy Wakim, stretching to game nights, movie nights, crafting nights, and the requisite Halloween and summer parties. To all who have provided much needed social entertainment - including, but not limited to: Evan Ranken, Amanda Davis, and Joe Murphree; Maitreyi Jayaseelan, Justin Schultz, Justin and Samantha Dressel, Erik and Ashley Garcell, Emily and Jeff Kleykamp, Phil Lewalle, Ben Ecker, Eva and Paul, Aku and Meghan, Sara Bucht, Marissa Adams, Diana Knyazeva and Angela Knyazeva (particularly for the outdoor exercise). An organic movement among graduate students studying problems in quantum optics has gained a large amount of traction thanks to Areeya Chantasari and Bethany

Little, for which I am very grateful.

My family has supported me in this journey since before I came to Rochester, and I owe much of my curiosity to the early microscope and crystal growing kits that hung around our basement.

Abstract

We report on several experiments using single excitons confined to single semiconductor quantum dots (QDs). Electric and magnetic fields have previously been used as experimental knobs to understand and control individual excitons in single quantum dots. We realize new ways of electric field control by changing materials and device geometry in the first two experiments with strain-based InAs QDs. A standard Schottky diode heterostructure is demonstrated with graphene as the Schottky gate material, and its performance is bench-marked against a diode with a standard gate material, semi-transparent nickel-chromium (NiCr). This change of materials increases the photon collection rate by eliminating absorption in the metallic NiCr layer. A second set of experiments investigates the electric field response of QDs as a possible metrology source. A linear voltage potential drop in a plane near the QDs is used to describe how the spatially varying voltage profile is also imparted on the QDs. We demonstrate a procedure to map this voltage profile as a preliminary route towards a full quantum sensor array. Lastly, InAs QDs are explored as potential spin-photon interfaces. We describe how a magnetic field is used to realize a reversible exchange of information between light and matter, including a discussion of the polarization-dependence of the photoluminesence, and how that can be linked to the spin of a resident electron or hole. We present evidence of this in two wavelength regimes for InAs quantum dots, and discuss how an external magnetic field informs

the spin physics of these 2-level systems. This thesis concludes with the discovery of a new class of quantum dots. As-yet unidentified defect states in single layer tungsten diselenide (WSe_2) are shown to host quantum light emission. We explore the spatial extent of electron confinement and tentatively identify a radiative lifetime of ~ 1 ns for these single photon emitters.

Contributors and Funding Sources

This work was supervised by a dissertation committee consisting of Professors Judy Pipher (Department of Physics and Astronomy), Nick P. Bigelow (Department of Physics and Astronomy), Miguel Alonso (The Institute of Optics) and A. Nick Vamivakas (The Institute of Optics). Funding for the research was provided in part by the following grants and organizations:

NSF - EFRI - EFMA - 1542707

NSF - DMR -1553788

AFOSR- FA9550-16-1-002

DMR-1309734

Institute of Optics

List of Tables

List of Figures

List of Acronyms

QD	quantum dot
SAQD	self-assembled quantum dot
s,p,d	atomic orbitals
S, J	electron, hole spin angular momentum
M	electron and hole composite spin angular momentum
pL, PL	photoluminescence
FWHM	full width half max
μ-PL	micro-photoluminescence
CCD	charge coupled device
NA	numerical aperture, $\sin\theta$, where θ is the half-angle of the light cone
GV	gate voltage
MBE	molecular beam epitaxy
CVD	chemical vapor deposition
NIR	near Infra Red
QCSE	quantum confined Stark effect
X^0	neutral exciton
X^{1+}	positively charged trion
X^{1-}	negatively charged trion

SEM	scanning electron microscope
QHE	quantum Hall effect
NV	nitrogen vacancy
ODMR	optically detected magnetic resonance
2DEG	2 dimensional electron gas
APD	avalanche photodiode
TMDC	transition metal dichalcogenide

Chapter 1

Quantum Dot Physics

A quantum dot in any form can be thought of as a highly engineered defect in an otherwise perfect (semiconductor) lattice, growing out of semiconductor materials research spanning decades. The zero-dimensional nature represents the culmination of the road of confinement, which starts with an unconfined (three-dimensional) bulk material. A free electron in a semiconductor is understood through the fundamentals of the semiconductor band structure and density of states. From this, the concepts of conduction band, valence band, holes, and bound states of electrons and holes (excitons) follow. In order to understand the atomic-like discrete energy spectra of a semiconductor quantum dot, it is therefore necessary to discuss how these bulk quantities play out in lower dimensions.

1.1 Stranski-Krastanov Artificial Atoms

The quantum dots used in this thesis are grown by molecular beam epitaxy (MBE) in a process called self-assembly. To activate this process, we first choose appropriate III-V binary and tertiary material pairs (e.g., InAs/GaAs, InP/GaInP) whose lattice

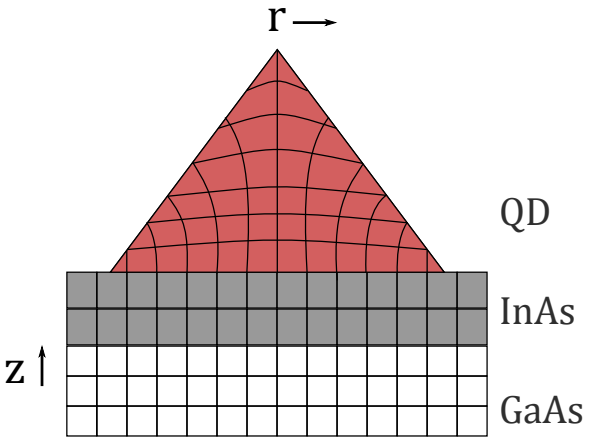

Figure 1.1: Cartoon of the self-assembly process. Squares represent unit cells for InAs (gray) and GaAs (black). The first mono-layer of InAs on GaAs is lattice-matched to the GaAs substrate, although highly strained. This causes subsequent growth to form islands of InAs, resulting in the self-assembled quantum dot.

constants differ by a few to ten percent. In this thesis, we focus on the material pair InAs/GaAs, which have lattice mismatch of 7%. The MBE growth is controlled to the point of where one can achieve mono-layer crystallization, resulting in extremely pure lattices. However, in self-assembly, the first mono-layer of InAs that crystallizes on top of GaAs is significantly strained from the lattice constant difference. As the next mono-layer is added, a spontaneous phase transition occurs to form small islands of InAs instead of subsequent smooth layers. This process is known as the Stranski-Krastanov method, and can result in islands as small as 10 nm (radius) by 5 nm (height). An un-capped island is shown in Figure 1.1 where the squares represent unit cells for the indicated material. For most studies not involved with characterizing the shape of the islands, a capping layer of GaAs is placed on top of the InAs. These three layers form the heart of a QD-based heterostructure, but additional materials can be grown both before and after the QD layer, and some will be discussed in later chapters. In principle, the mean separation between individual self-assembled quantum dots (SAQDs) is random, but a significant research thrust is

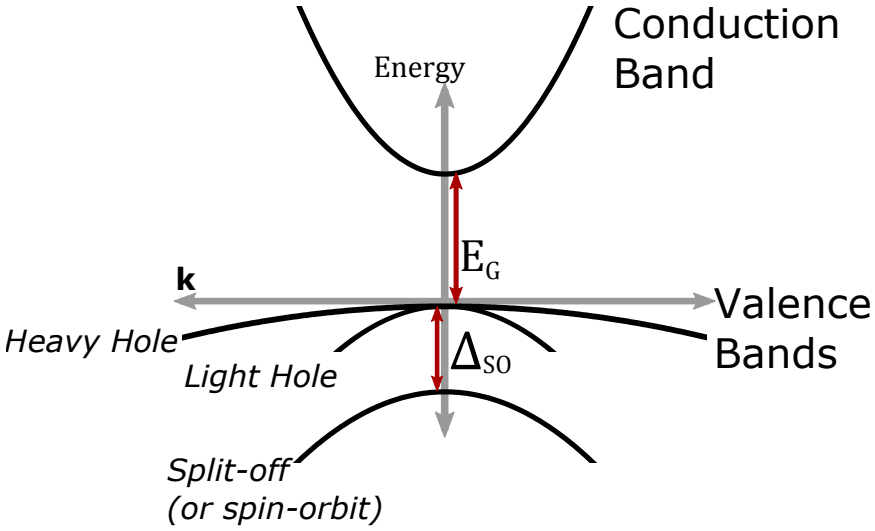

Figure 1.2: Bulk semiconductor band structure near **k**=0 in the k-dot-p perturbation theory. Each band shown is doubly degenerate for a total of eight bands.

being made to 'seed' the growth of the islands, for instance by first etching trenches into the GaAs substrate. In regions between the SAQDs, residual mono-layers of InAs form a quantum well, known as the 'wetting layer'. Optical studies of the light emission from SAQDs are based on the recombination of an electron and a hole, and the energy of the outgoing photon is indicative of the environment which hosted the electron and hole. In bulk semiconductors, the term 'exciton' is used to refer to an electron and a hole bound to each other, in analog to the hydrogen atom. As we will see, confinement can play a larger role than the binding of the single particles, however, due to historical reasons we will continue to refer to excitons when discussing optical emission from the QDs.

In order to arrive at a satisfactory model for optical emission from a SAQD, we need to understand the single particle (electron and hole) wavefunctions and energy eigenvalues. These essential quantities can be derived from the bulk material characteristics, as the single particle confinement will be strongest in the growth direction which mimics the structure of a (Type-1) quantum well. Thus, parameters such as

the conduction band minima, valence band maxima, bandgap, and effective mass will be useful in describing the decidedly disordered lattice structure that is a QD. A brief discussion of semiconductor band structure, in the eight-band k-dot-p theory, is presented before considering confinement effects.

1.2 Band Structure: Briefly

When a large number of identical atoms is arranged into a lattice, the outer-most electrons become de-localized from their respective atomic nuclei, and move freely throughout the lattice. These electrons move in a periodic potential given by the positively charged nuclei at the fixed lattice sites. Calculating the motion of these free electrons, as a function of their momentum, is the subject of band structure theory. We start by considering the electronic wavefunction , $\psi(\mathbf{r})$ (Bloch wave function):

$$\psi_{n,\mathbf{k}}(\mathbf{r}) = e^{i\mathbf{k}\cdot\mathbf{r}} u_{n,\mathbf{k}}(\mathbf{r}), \tag{1.1}$$

where $\mathbf{r}$ is the position, $\mathbf{k}$ is the crystal wave vector, u is a function with the same periodicity as the crystal lattice, and n, the principal quantum number, refers to the band index. Our perturbation method allows us to write the Schrödinger equation for the nearly-free electrons as an unperturbed Hamiltonian of free electrons, with the crystal wave vector and momentum as a perturbation:

$$H = H_0 + H_k^{'}, \tag{1.2a}$$

$$H_0 = \frac{p^2}{2m} + V, \tag{1.2b}$$

$$H_k^{'} = \frac{\hbar^2 k^2}{2m} + \frac{\hbar \mathbf{k}\cdot\mathbf{p}}{m}. \tag{1.2c}$$

In this way, we can take the Bloch wavefunction to be that of a free electron around small $\mathbf{k}$. Figure 1.2 shows the parabolic conduction band and valence band(s) at the $\mathbf{k} = 0$ point for a direct gap semiconductor, with the values for GaAs and InAs at room temperature shown in Table 1. The conduction band wavefunctions have an s-like character ($n = 0, l = 0, j = l + s = s = 1/2$), and the angular momentum is consistent with this as $|\mathbf{S}_{CB}| = 1/2$, with projections onto the growth axis ($\mathbf{z}$) of $S_z = \pm 1/2$, thus making the conduction band doubly degenerate.

The valence band character is dominated by p-type orbitals ($n = 1 \rightarrow l = 0, 1; s = 1/2, j = l + s = 3/2, 1/2$) with three values of angular momentum, each with a double degeneracy in the z-projections for a total of 6 bands:

$$|\mathbf{J}| = 3/2, J_z = \pm 3/2,$$

$$|\mathbf{J}| = 3/2, J_z = \pm 1/2,$$

$$|\mathbf{J}| = 1/2, J_z = \pm 1/2.$$

In principle these six bands would be degenerate in energy. However, as is evident in Figure 1.2, the spin-orbit interaction ($\mathbf{J} = \mathbf{L} \cdot \mathbf{S}$) decreases the energy of the $|\mathbf{J}| = 1/2$ bands relative to the $|\mathbf{J}| = 3/2$ bands. Thus this band earns its nickname, the split-off band. Values for Δ_{SO} for GaAs and InAs (at room temperature) are also shown in Table 1.1. The remaining two bands are termed 'light hole' and 'heavy hole' due to the effective mass of each band, which corresponds to the spin-projections of $J_z = \pm 1/2$ and $J_z = \pm 3/2$, respectively.

	E_G (eV)	$\Delta_{SO}(eV)$
GaAs	1.42	0.34
InAs	0.354	0.41

Table 1.1: Direct-gap and split-off energies for InAs and GaAs

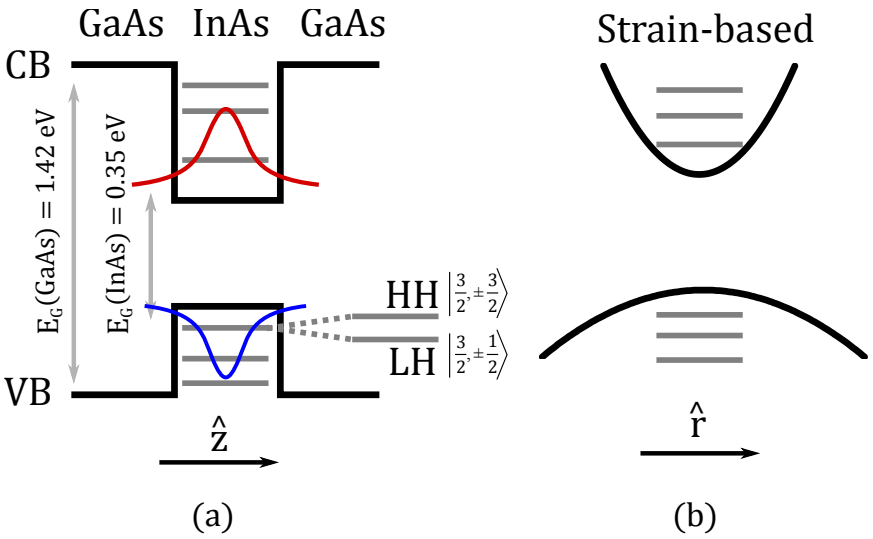

Figure 1.3: (a) Conduction band minimum and valence band maximum for GaAs and InAs, showing how the growth direction confinement mimics that of a quantum well. Single particle states for electrons and holes are shown in the InAs layer. (b) Depending on the exact size of the quantum dot, confinement in the in-plane direction is often approximated as a parabola, and the single-particle states those of a quantum harmonic oscillator.

1.3 Confinement

Self-assembled quantum dots confine electrons and holes separately, thus stretching the traditional definition of an exciton. To arrive at single-particle confinement in all three dimensions, we consider the growth direction and in-plane direction. Recall that the physical size and shape of our InAs SAQD is that of a lens, roughly 5 nm in height (growth direction) and 15 - 40 nm across. As shown in Figure 1.3(a), the abrupt change in material parameters in the growth direction creates a step-like potential, reminiscent of a quantum well. The more gradual change in material parameters follows the shape of the InAs islands for in-plane confinement, which can be approximated as a two-dimensional harmonic oscillator. Thus, in each dimension, a series of discrete energy levels for both the electron and hole are formed, with energy levels equally spaced by the characteristic energies $\hbar\omega_e$ and $\hbar\omega_{hh}$, each in the 10s of meV range. The exact characteristic energies vary from dot to dot, as the size of the dot varies. This has significant consequences for optical recombination of electrons and holes, implying that each dot will have a unique set of optical resonances. Nomenclature for these discrete states follows that of atomic shell spectroscopic notation, with the energy levels closest to the conduction band minima (for electrons) and valence band maxima (for holes) called the s-shell states, with the next highest being p-shell, etc.

In Figure 1.4 (a), we show the occupation of the valence band and conduction band for the neutral (negatively charged) exciton configuration on the top row (bottom row). In the neutral exciton, the electron ($\downarrow$) occupies the ground state of the conduction band and the hole ($\Uparrow$) sits in its ground state in the valence band. Each of these states are doubly degenerate, admitting both spin projections in the single particle ground states. Recombination of an electron and hole from these states results in

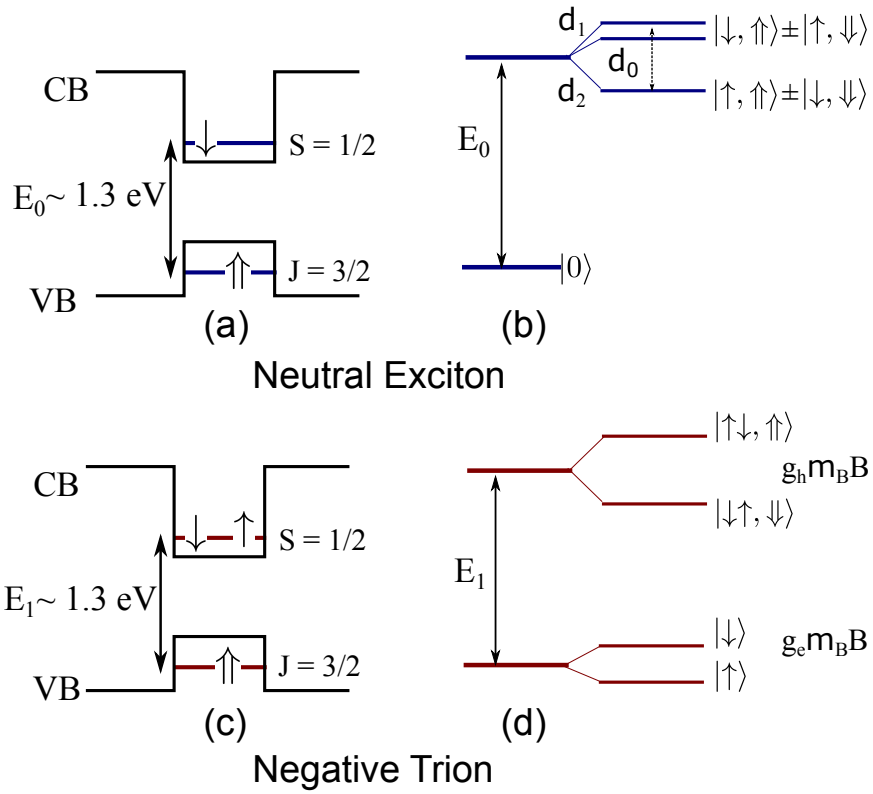

Figure 1.4: Occupation of the conduction and valence band in the single-particle picture for the exciton (a) and trion (c). The trion forms a closed spin state in the conduction band. (b),(d) Atomic energy level notation for neutral exciton and negative trion. The ground state refers to the occupation of the dot without optical excitation, and the excited state corresponds to the occupation of CB and VB shown in (a),(c). The fine structure (right-hand portion) will be detailed elsewhere and is shown here as a prelude.

s-shell photoluminesence. If we were to add another electron to the conduction band, we would have a closed shell for the electron states and this second electron would take on the opposite spin (↑). This is shown in the lower panel for the negatively charged exciton, or trion (since there are three particles). Radiative recombination takes place between the electron and hole of opposite spin projections, as will be discussed below at length regarding angular momentum conservation. Multi-excitons can have a variety of configurations depending on the number of single particles. For instance, if two electrons and two holes were present in the dot, both the electron and hole shells would be filled. Any further multi-exciton states would result in filling higher-lying states, resulting in radiative recombination at higher energies.

1.4 Two Level Systems

We have established the physical basis for exciton confinement in SAQDs in the single-particle picture, and started to explore the atomic-like character. An important model in atomic physics is that of the two-level system, which is often an approximation based on fine and hyperfine sublevels of an atom's electronic energy configurations. SAQDs make excellent two-level systems due to the strong adherence to optical selection rules set for in the dipole-allowed interband optical transitions. The atomic picture of energy levels for the exciton and trion are shown in Figure 1.4(b). In this picture, the ground state refers to the QD energy without optical excitation, and the excited state corresponds to the occupation of electrons and holes seen in Figure 1.4(a). Both the excited and ground states are now referred to with the use of bra-ket- notation, as will be the case throughout the rest of this thesis. Note that the trion has a charged ground state, which can be exploited for quantum technologies. We also hint at the fine structure of each of these transitions (exciton and trion), as

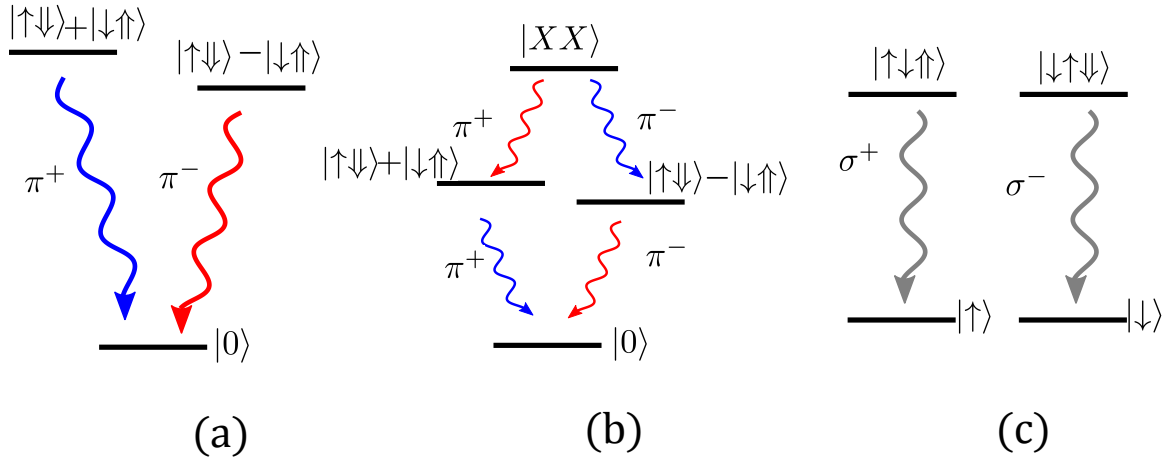

Figure 1.5: (a) Neutral exciton transition can be seen as a three-level system. (b) Bi-exciton cascade (c) Charged exciton as a degenerate two-level system.

the energy levels are branched out to the right of the main transitions. This will also be discussed below.

From the band structure and single particle confinement discussed above, electrons confined in the QD carry spin angular momentum, $|S| = 1/2$ and heavy-holes $|J| = 3/2$. The arrangement of the electron and heavy hole spin govern the optical emission process, which is considered in the electric dipole approximation. We begin considering the composite spin system for the neutral exciton, $M = S_Z + J_Z$ in terms of the z-projections of the single particle states which can take on $S = |\uparrow\rangle$ or $|\downarrow\rangle$ and $J = |\Uparrow\rangle$ or $|\Downarrow\rangle$. There are four total arrangements shown in Table 1.2.

Electron-hole exchange interaction breaks the degeneracy of the $M = 1$ and $M = 2$

M	$\lvert S_z, J_z\rangle$
1	$\lvert\uparrow,\Downarrow\rangle$
1	$\lvert\downarrow,\Uparrow\rangle$
2	$\lvert\uparrow,\Uparrow\rangle$
2	$\lvert\Downarrow,\Downarrow\rangle$

Table 1.2: Possible combinations of angular momentum projections for the two-particle state of the neutral exciton.

states. Since circularly polarized light carries angular momentum of ± 1, the $M = 1$ states are optically active in a straightforward way, and the light emission is polarized in the circular basis (left or right -handed) according to the spin projection. Although the + 1 and -1 states should be degenerate transitions, fine structure in the energy levels is observed due to the electron-hole exchange interaction. Additionally, the eigenstates hybridize, along with the polarization selection rules, to give off linearly polarized light. The resulting energy level structure and eigenstates are shown in Figure 1.5(a), where the linear polarization states (π^+, π^-) are indicated on the relevant transitions. This is an example of a three-level V system since the ground state is an empty QD. A more complete picture of the fine structure is given in Chapter 4.

The bi-exciton is shown in Figure 1.5(b), consisting of two electrons and two holes as mentioned in the previous section. Interestingly, the bi-exciton is a cascaded system whereby the system loses energy first by having one electron hole pair recombine, landing the system into one of the two exciton fine structure states just discussed. Precluding any further excitation back into the bi-exciton state, the residual exciton then radiatively recombines. This process results in two photon emissions which are highly correlated in polarization state. The two recombination events are temporally offset from each other as the biexciton is a real state and has a finite lifetime of a few ns.

The singly charged excitons (Figure 1.5(c)) are perhaps the most straightforward example of a two-level system in a SAQD. The electron-hole exchange interaction is more complex due to the three composite particles rather than two, thus there is very little perturbation of the excited state, and the two spin projections are degenerate without a magnetic field. We will explore the fine structure of the negative trion in Chapter 4 as a method to encode the photon polarization in an electron spin.

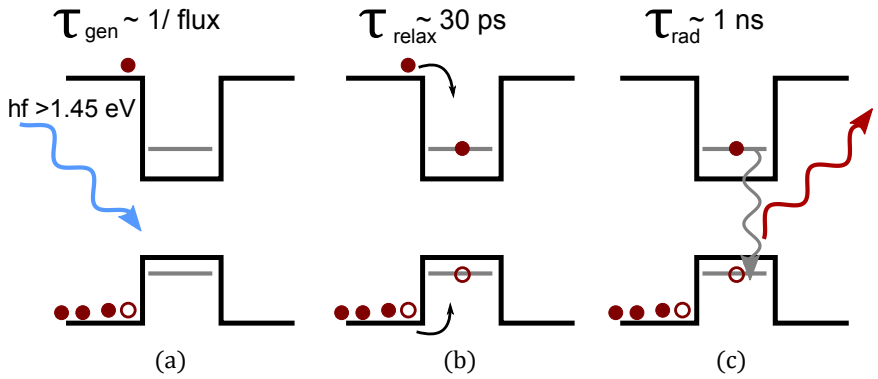

Figure 1.6: (a) Absorption of incident light ($hf > 1.45$ eV, the bandgap of GaAs) promotes an electron in the valence band of GaAs to the conduction band, at a rate proportional to the incident light intensity. (b) The electron and hole non-radiatively relax into the quantum dot. (c) Electron and hole recombination after 1 ns, resulting in an outgoing photon of lower energy than the incoming photon.

1.5 Photoluminesence Spectroscopy

To experimentally access the optical transitions described above, non-resonant optical excitation (photoluminesence) is used to generate excitons within a single QD. The main advantages of this technique are that it requires little sample preparation, and can discriminate different regions of the QD wafer (high density vs. low density) with great accuracy. Because each SAQD will differ slightly in size and shape from the rest, the optical resonances can vary as much as 20nm ($\approx$ 30meV) from one dot to the next. Individual resonances can be as narrow as a few μeV - thus, non-resonant excitation is a necessity before advancing to resonant excitation.

The cyclic nature of photoluminesence is shown in Figure 1.6 using the band diagrams from Figure 1.4, and illustrating the process for a neutral exciton formation in the QD. In Figure 1.6(a), a photon with energy greater than $E_g^{GaAs} = 1.45$ eV is incident on the heterostructure, and absorbed by the semiconductor matrix surrounding the QD. This promotes an electron from the valence band to the conduction band. The incident photon flux is proportional to the intensity of the incident laser, which

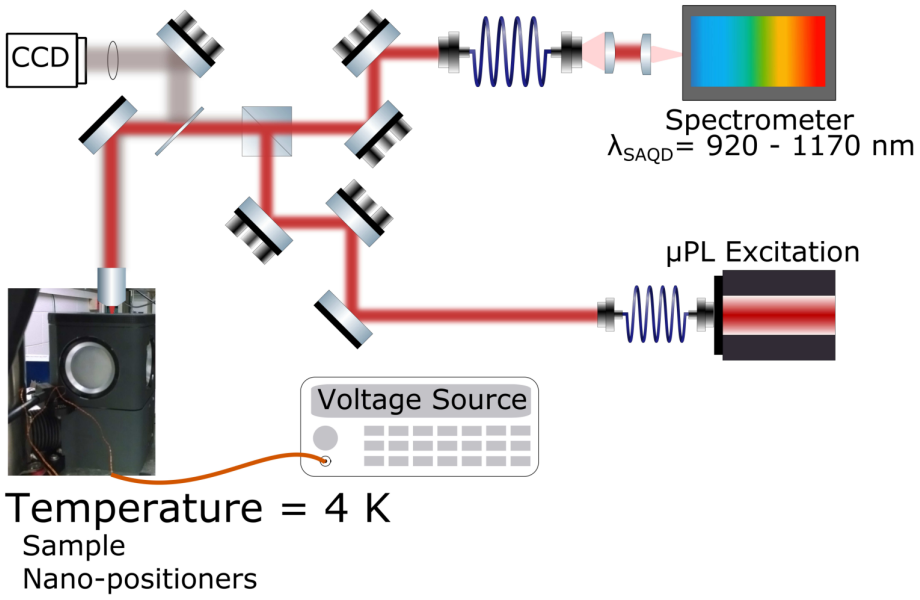

Figure 1.7: Schematic of a micro-photoluminesence spectroscopy experiment for samples at cryogenic temperatures (4 Kelvin). Above-band laser light (780 nm) is sent to the sample through a high NA (0.7) objective. Light is collected from the sample and spatially filtered using an optical fiber, resulting in diffraction-limited interrogation area. The fiber is sent to a spectrometer where the light from the sample is dispersed by a grating and detected by a CCD (not shown).

leads to excitons being generated with a rate $\frac{1}{\tau_{gen}} \propto$ laser intensity. In Figure 1.6(b), single particles created outside (but near) the QD quickly (20 -30 ps) non-radiatively relax into the confined states of the QD. After the characteristic lifetime (radiative lifetime, $\sim$ 1 ns) of the confined exciton, the electron and hole annihilate, resulting in photon emission - Figure 1.6(c). Due to energy and momentum conservation rules, the energy (wavelength) and polarization of this out-going photon reflect the QD environment, as discussed above.

Photoluminesence is the process by which we generate light from the QD environment. Implementation of photoluminesence for spectroscopy requires a minimum amount of hardware for excitation and collection. For our experiments, a confocal microscope, schematically shown in Figure 1.7, is used to identify regions of single QD

emission. The microscope uses the core of an optical fiber (NA=0.12, d$\approx 6\mu m$) as the confocal rejection mechanism in the collection paths. A high NA objective (0.7) in conjunction with the confocal paths allows diffraction-limited excitation and collection from a ≈ 1 μm spot, thus promoting our technique to micro-photoluminesence (μ-PL) spectroscopy. The collected photons are sent to a 0.75m focal length imaging spectrometer for spectral analysis, and the schematic can be found in Figure 5.4. The CCD camera used for detection is either a silicon CCD (for spectra above 1.1 eV) or InGaAs CCD (for spectra around 1.1 eV). In both cases, the spectral resolution we can achieve in this setup is 30μeV. For lifetimes of 1 ns, we can expect a lifetime-limited PL linewidth of ≈ 1 μeV. Thus, in the basic setup, all the QD spectra shown are resolution-limited by the chosen detection method.

At room temperature, the semiconductor environment is readily active with vibrational excitation (phonons). This can work against the quantum confinement of the QDs, and results in broad PL spectra as there are many non-radiative processes which can add or subtract energy from the excited state. To work with strongly confined excitons, the samples are loaded into a close-cycle pulse tube cryostat with optical access from the top of the sample, and experiments are carried out at 4 Kelvin. The reduction in thermal population of phonons increases the amount of PL ending up in the zero-phonon mode, which is the one we took such care to describe in previous sections. Two models of optical cryostat are used in this thesis. The Montana Instruments Cryostation (with a side-view of vacuum chamber) is shown in the schematic of Figure 1.7. A second pulse-tube cryostat (attoDry 1000) hosts a superconducting coil, and samples are loaded in the bore of the coil to permit magnetic field studies up to 7 Tesla. In both cryogenic environments, the sample sits on top of nano-scale positioning piezo stages (for all three axes) to access different regions of the sample.

Transition	Delta Energy (meV)	Direction
XX	1-2	red
X^{1+}	0.5-1.5	blue or red
X^{1-}	4-6	red

Table 1.3: Values of relevant exciton energies relative to the neutral exciton

1.6 Exciton Identification in Single QD spectra

We have discussed the fine structure within an individual species of exciton, but the different exciton species are also non-degenerate in energy. In modeling the neutral exciton, we have already included components of the Coulomb interaction and exchange interaction. But, when the system complexity is increased by adding more particles to the excited state of the QD, these considerations have to be revisited. Identification of different excitonic spectral features is a main goal of non-resonant μ-PL spectroscopy, and there are two main heuristics used for InAs SAQDs. First, characteristic energy scales have been identified for excitons carrying N electrons or holes relative to the neutral exciton, as well as the neutral bi-exciton. Table 1.3 lists the average values measured in our experiments, consistent with other reports in the literature [1–4].

Second, the response to increase in (non-resonant) laser intensity can be described with a population evolution model. The laser power is mapped to a generation rate of electron-hole pairs, and if the radiative lifetime of an exciton is longer than the exciton generation rate, a second exciton pair can be captured before the first pair decays. This can lead to a cascaded photon decay, with the bi-exciton recombination correlated to the exciton recombination. Decay from the $(i+1)$th multiexciton to the

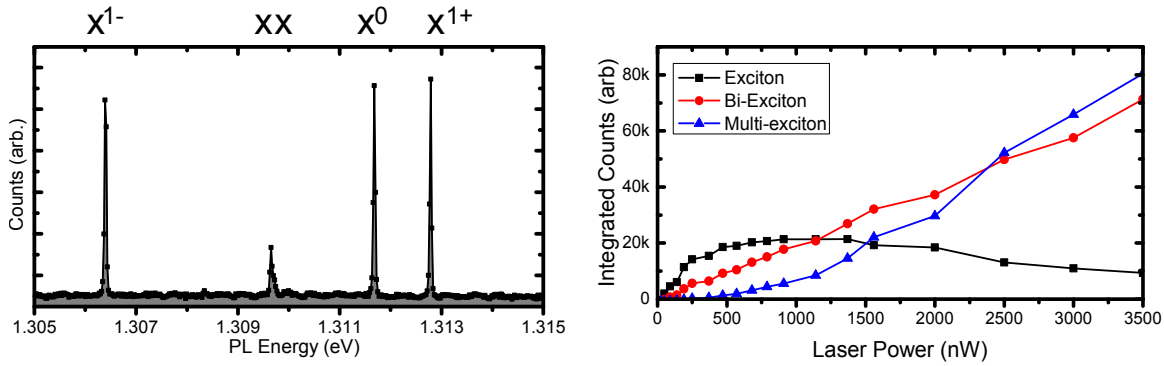

Figure 1.8: (a) Spectral features from indicated excitonic features in a single quantum dot. (b) Power dependence of PL intensity

ith exciton gives a set of coupled rate equations [5],

$$\frac{dn_i}{dt} = G(t)n_{i-1} - \frac{n_i}{\tau_i} + \frac{n_{i+1}}{\tau_{i+1}} - g_{i+1}.$$

Restricting ourselves to at most a bi-exciton (two electron-hole pairs), and with a cw laser, solving for the steady-state population gives:

$$n_1 = \frac{G\tau_1}{1 + G\tau_1 + G^2\tau_1\tau_2} \approx G\tau_1(1 + G\tau_1),$$

$$n_2 = \frac{G^2\tau_1\tau_2}{1 + G\tau_1 + G^2\tau_1\tau_2} \approx G^2\tau_1\tau_2(1 + G\tau_1).$$

where τ_i is the radiative lifetime of the ith multiexciton, G is the photo-generation rate, n is the probability to find the ith multiexciton, and g is the potentially non-radiative decay rate to the $(i-1)$th exciton.

Using the binomial approximation, we can see that photon emission from single excitons (X^0, X^{1-}, X^1) will increase linearly with increasing laser power, whereas a bi-exciton, XX, will have a quadratic dependence. Additionally, saturation phenomena are briefly seen as the PL counts from each exciton species will first increase, reach a maximum, and then decrease as the next highest exciton species becomes populated.

1.7 Conclusions

We have established the physical nature of self-assembled InAs quantum dots by describing the growth mechanism and understanding how electrons and holes are confined. The confinement creates a unique type of exciton, which radiatively recombines. Charged excitons and multiexcitons can also be created. Photoluminescence spectroscopy is the main experimental technique used in this thesis.

Chapter 2

Voltage Control of InAs QDs

In addition to controlling the luminescence intensity, tunable optical emission is a requirement for any proposed devices utilizing the quantum light emission from a quantum dot. In this chapter, we describe the two-fold impact of creating an opto-electronic diode out of the QD heterostructure. We focus on a Schottky diode, and describe how the diode allows for controllable charging of the QD ground state, as well as providing an experimental knob which can shift the PL emission energy of the QDs.

We saw in Chapter 1 that SAQDs are inherently heterostructures based on mature semiconductor growth, processing and fabrication. This makes them natural candidates to monolithically incorporate into novel nano-optoelectronic devices. Of particular interest is the ability to apply an electric field across the quantum dot in a controllable manner. [1,6,7] Stark shifting the QDs electronic structure is a crucial ingredient in applications ranging from solid state quantum optics, [8–11]quantum information science, [12–15] and metrology [16,17] to integrated nanophotonics, [18–22] and new approaches to achieve this electrical control are desirable. In the latter half of this chapter, we show how graphene, an emergent material, can be used as the

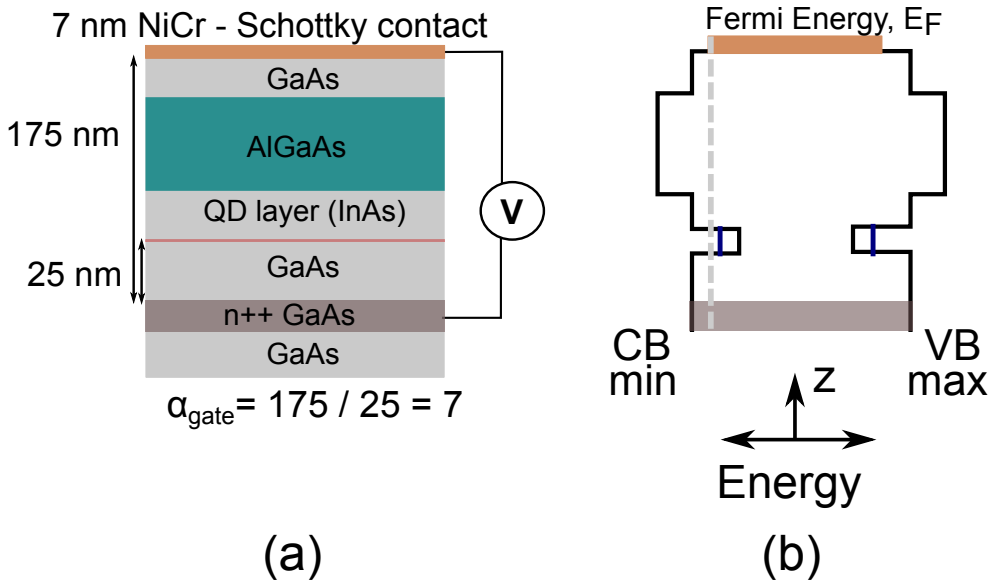

Figure 2.1: (a) Wafer growth sequence for n-i-Schottky QD diode showing the tuning parameter α. (b) Energy band parameters for the material sequence shown in (a). The Fermi energy (grey dotted line) is pinned throughout the layers according to the back contact, the n++ GaAs layer.

Schottky gate material in a straightforward demonstration.

2.1 Heterostructure Description

In the previous chapter, we focused the physical description of the SAQDs as an epitaxial layer on top of a slightly lattice mismatched material. We extend the heterostructure description to include two electrodes, one above and one below the SAQD layer, to create the standard diode. In keeping with the literature, a bias voltage across QD diodes will be referred to as a gate voltage.

The molecular beam epitaxy growth sequence is as follows. Highly doped (Si) GaAs is grown on top of an insulating GaAs substrate, followed by an intrinsic GaAs tunnel barrier (25-35 nm depending on the sample), then the InAs QD layer, followed by a capping layer of GaAs. An insulating layer of AlGaAs is next, followed by a final

layer of GaAs. The layer structure, with the growth in the z-direction, is shown in Figure 2.1. The parameter α is used below to consider the reduction of gate voltage at the QD level.

Processing the 2-inch wafers after MBE growth results in a Schottky diode by depositing a metallic layer on the top GaAs surface. For devices made at UR Nano, electron beam evaporation is used, in conjunction with a shadow mask on the sample surface, to deposit 7 nm of nickel-chromium (NiCr) alloy. Ohmic contact to the buried n-doped layer is made by making a controlled scratch on the surface of the GaAs (where there is no NiCr), and pressing a small dot of indium onto the scratch. Annealing for 10 min in nitrogen (N2) gas on a hot plate set at 100^oC results in indium diffusion to the bottom of the heterostructure. The device is then connected to external leads with silver paint. A first order test of the device is done by measuring the current passing through the heterostructure as a function of a DC voltage. The non-linear, rectifying characteristics are shown in Figure 2.2(b). The region between approximately -0.5 V to + 0.5V is linear with a small slope (1 nA / 0.1V), and this represents the dark current of the device. The linear region also corresponds to the bias window which provides voltage control to excitons in the QD layer, since an appreciable current in the non-linear regions implies that electron and hole recombination from the QD layer is suppressed, as the charges are swept to the electrodes.

2.2 Single Charging Events

When the QDs are tunnel coupled to a Fermi sea of electrons as described above, it allows for single charging of the ground state (i.e., without optical excitation) of the

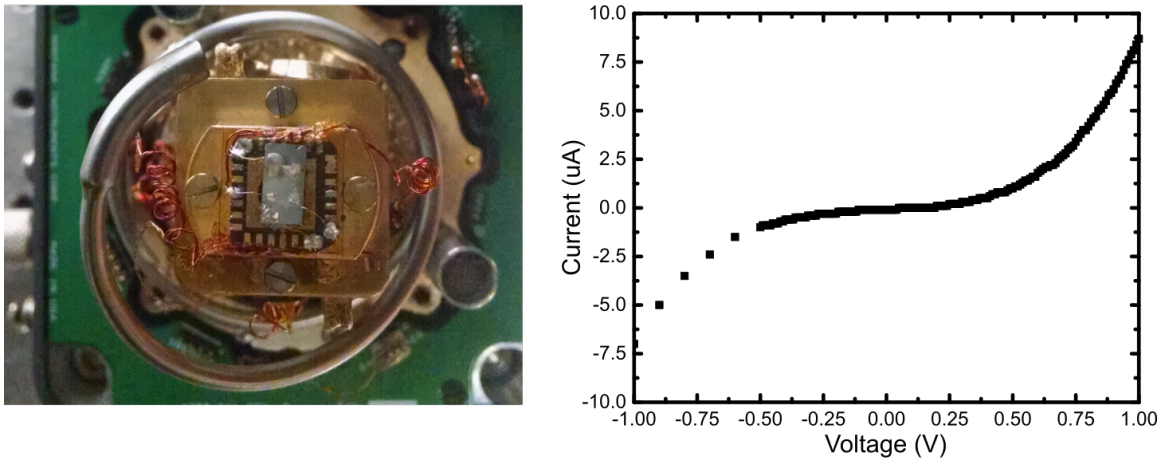

Figure 2.2: (a) Photograph of a fabricated device, mounted on an electrical chip carrier with breakout wires. (b) Current-voltage characteristics at room temperature showing diode characteristics. QD energy tuning is expected for regions of no current flow.

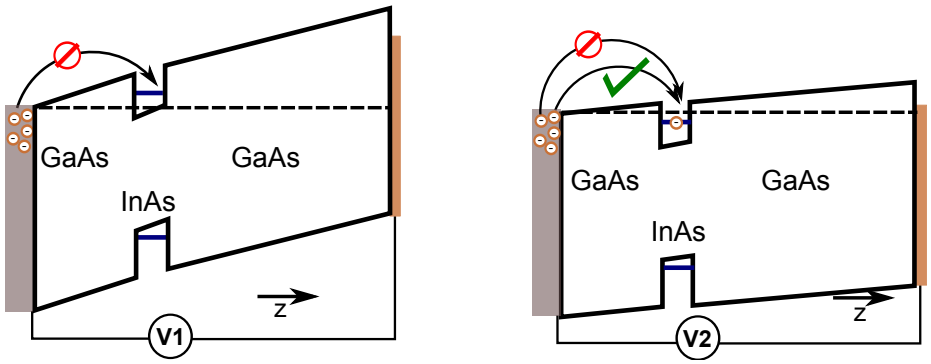

Figure 2.3: CB and VB showing electron and hole levels in the band structure picture, where the AlGaAs spacer is omitted for simplicity. The tunneling rate from the back contact is affected by the relation of the electron energy level to the Fermi energy level, which is modulated by adjusting the external voltage to shift the bands across the entire device.

quantum dot. The electrostatic energy of the QD is

$$E = \frac{Q^2}{2C} - Q\alpha V_g, \tag{2.1}$$

where C is the capacitance of the dot, α is the height of the tunnel barrier divided by the total separation of the plates, and V_g is the applied gate voltage. Tunneling due to thermal fluctuations is strongly suppressed at 4 Kelvin (ie, $\frac{e^2}{2C_0} >> k_bT$. Multiple, sequential tunneling events at a particular gate voltage V_g are suppressed due to the repulsive Coulomb energy $\frac{(Ne)^2}{C_0}$ between the charge in the dot and the charge in the Fermi sea - otherwise known as a Coulomb blockade. Therefore, we can expect there to be a range of gate voltages where a stable charge in the ground state exist. We can estimate this range by first classically estimating the dot as a metallic sphere, $C_0 = 4\pi\epsilon\epsilon_r R_0$. For a dot radius R_0 of 5 nm, $C_0 \approx 7$ aF, giving a charging energy of 26 meV. A quantum mechanical calculation [23] gives 30 meV as the charging energy for a dot radius of 25 nm.

In Figure 2.4, we present PL spectra as a function of the device bias - where we have scaled the applied gate voltage to the electrostatic energy using the electrostatic conversion in Equation 2.2.

$$eV_{el} = \alpha V_g. \tag{2.2}$$

The red boxes represent 27 meV bands, and we observe a single feature pronounced in each charging range - this corresponds to recombination from a charged exciton, to the indicated ground state. Note that a positively charged ground state is due to electron tunneling out of the dot - a neutral exciton is generated but the electron tunnels out before optical recombination. Thus, a hole is left in the QD, creating a charged ground state. For the neutral ground state, a weak PL signature can be seen

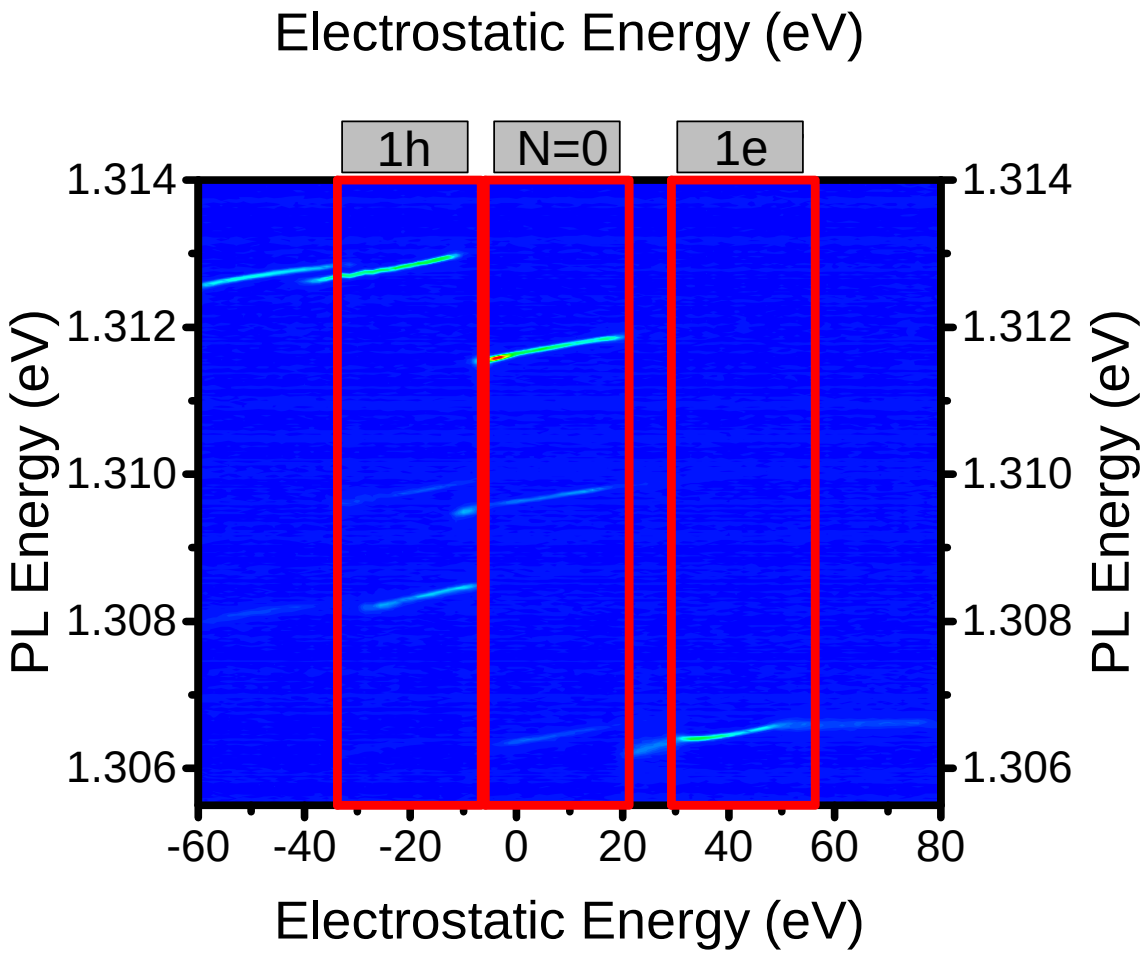

Figure 2.4: PL spectra recorded as the external voltage is changed. X-axis has been scaled to local QD potential energy using Equation 2.2. Coulomb blockade plateaus are easily visible, and are highlighted by the red boxes. The ground state for each charging plateau is identified as single charging events result in abrupt changes in PL energy. In transition from X^{1+} to X^0 emission at roughly -8 meV, the PL at approximately 1.313 eV shifts down by roughly 1.5 meV, and at +20 meV the X^0 to X^{1-} transition is accompanied by a shift of approximately 5 meV in the PL spectra.

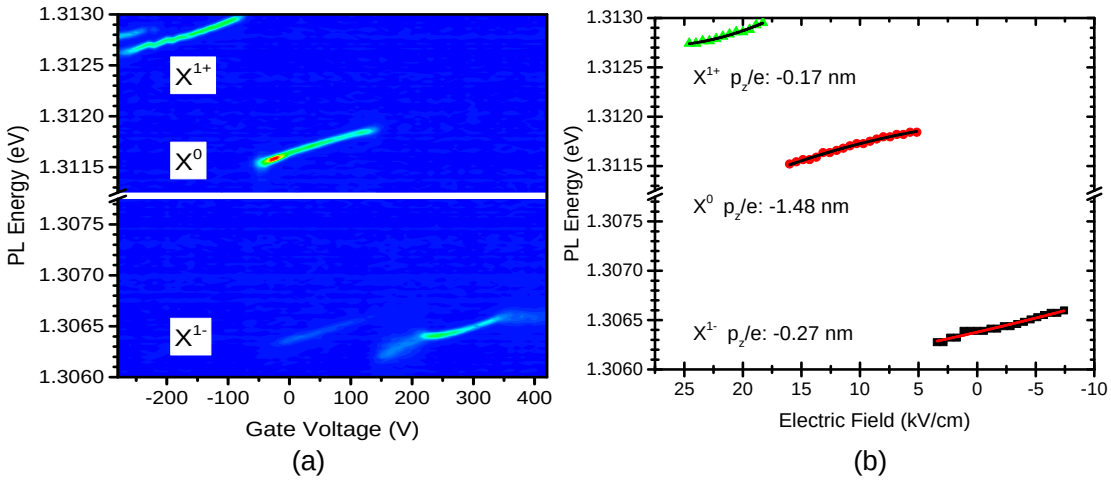

Figure 2.5: (a) PL spectra as gate voltage is tuned, with external voltage as the labeled axis. Graph is scaled to examine X^{1+}, X^0 and X^{1-} features, each of which display ≈ 0.3 meV of spectral tuning within the charging plateau. (b) Individual exciton features are fit to the quantum confined Stark effect, which gives the transition dipole moment, $\frac{p_z}{e}$.

from the bi-exciton. In the negative trion (1e ground state) charging plateau, the PL first appears broadened and with reduced intensity before regaining the resolution-limited linewidth. This is due to details of the electron tunneling, which will not be covered here.

2.3 Quantum Confined Stark Effect

In addition to control over the ground state charge of the quantum dot, QDs used in photonic devices require detailed control over the emission energy of the individual exciton features - most often to tune the QD resonance through a cavity mode. In Figure 2.4, we can see that the emission energy is tunable with applied voltage. Across a single charging plateau for the neutral exciton, as in the inset of Figure 2.4(a), we can achieve approximately $\frac{\Delta E}{\Delta V} = \frac{350}{200}\frac{\mu eV}{mV} \approx 1.75\frac{\mu eV}{mV}$ of tuning on a single exciton feature before the next charging event.

The physical nature of this tuning lies in the response of the single particle states to the (static) electric field applied along the growth direction (**z**). Within the effective mass approximation, and k dot p approach, the electron and hole wavefunctions are confined in the **z** (growth) direction such that they are stacked on top of each other, leading to a permanent dipole moment, **p**. The exact arrangement of electron and hole wavefunctions can vary depending on the dot composition and structure. [24] Thus, both positive and negative dipole moments have been observed - corresponding to either the hole or electron residing in the apex of the hemispherical dot model.

Since the electric field is applied strictly in the growth direction (neglecting fringing fields at the edges of the Schottky contact), we can use the well-established quantum-confined Stark effect (including our linear term due to the permanent dipole moment) to measure the dipole moment and polarizability of each excitonic transition [24]:

$$E = E_0 - p_z \cdot F_z + \beta \cdot F_z^2, \tag{2.3}$$

where p_z represents the dipole moment in the growth direction, and β is the polarizability. Let's now relate the field to the voltage. Using geometrical, capacitive considerations:

$$F = -\frac{V_{bi} - V_{applied}}{d}. \tag{2.4}$$

With this convention, a negative electric field points from the wetting layer to the surface. A positive field points from the surface to the back contact, d is the distance between top and bottom contacts (175 nm), and V_{bi} is the built-in voltage resulting from the metal-semiconductor interface at the surface of the device. Applying this model to the voltage-dependent PL we have seen so far, the dipole moments for X^{1+}, X^0 and X^{1-} are reported in Figure 2.5.

2.4 Graphene Gate vs. NiCr Gate

Throughout the last decade the remarkable optical and electronic properties of graphene have been explored. [25] Graphene electron mobilities have been reported approaching 10^6 cm^2 V^{-1} s^{-1}, and single layers exhibit 2.3% absorption per layer across a broad spectrum. [26, 27] It has been recognized that as a semi-metal, graphene and few layer graphene flakes are attractive candidates for electrical contacts to nanophotonic devices as graphene minimizes optical loss while simultaneously allowing for GHz electrical control. [28, 29] Further, the maturation of the graphene opto-electronics enterprise has resulted in robust procedures to transfer graphene and few layer flakes from handle substrates to target devices. [30, 31] It is therefore natural to inquire if graphene can be incorporated into quantum dot devices in a meaningful way.

Conventional electrical control of InAs self-assembled quantum dots has relied on p-i-n or Schottky diodes as discussed in the previous section. Recent work has confirmed rectifying behavior in GaAs/graphene diodes. [32, 33] In this work, we use single to few layers of graphene as the top gate in a Schottky field-effect device to electrically control the optical response of individual InAs quantum dots. An added benefit of unlocking the potential of graphene for quantum dot electrical control is a path toward low loss electrical contacting of quantum dots in photonic crystal circuitry. [34]

2.4.1 Sample Description and Graphene Transfer

The quantum dot heterostructure used in this work was grown by molecular beam epitaxy. A highly-doped n++ GaAs layer was grown 25 nm beneath the InAs quantum dot layer to serve as the back contact. The quantum dots were grown on a rotation stop such that a density gradient formed across the wafer, and then capped with

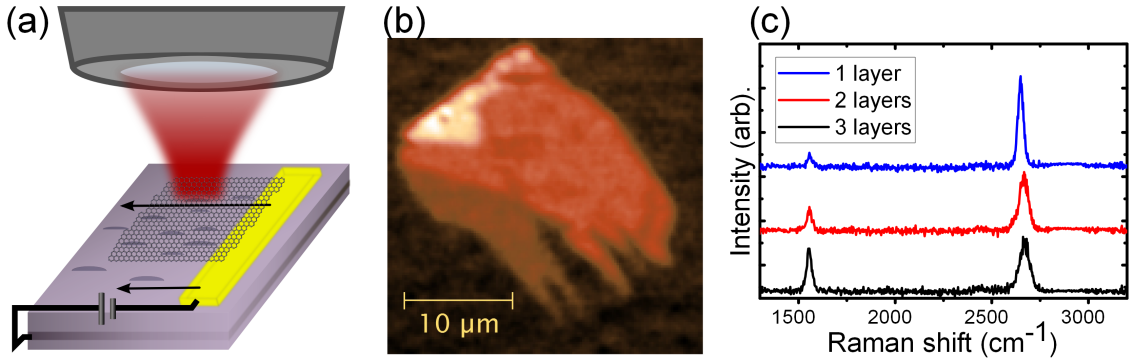

Figure 2.6: (a) Device schematic. The quantum dots are situated between a Schottky contact provided by the graphene, and a back gate formed during heterostructure growth. Ohmic contact to the graphene is made with a macroscopic gold contact. Arrows indicate the positions of hyperspectral photoluminescence measurements. (b) Confocal scanning Raman microscope image of graphene flake before transfer. Lighter colors represent thicker layers. (c) Raman spectra of graphene flake with excitation at 532 nm.

GaAs, followed by $Al_{(0.33)}Ga_{(0.67)}As$ barriers, to prevent holes from diffusing to the surface, and a final GaAs cap layer formed the surface of the device. Regions of low-QD-density (3 x 10^{10} cm^{-2}) were used to investigate single quantum dots. A Cr/Au layer (4 nm/50 nm) was evaporated onto the wafer surface to form a strip that served as electrical contact for the graphene, as shown in Figure 2.6(a). Ohmic contact to the n++ GaAs layer was made by diffusing indium through the heterostructure.

An all-dry viscoelastic stamping technique [31] was used to exfoliate and transfer graphene flakes onto the Cr/Au layer. Figure 2.6(b) shows a Raman image of the graphene flake before transfer to the GaAs. Raman spectroscopy on the flake was based on a scanning confocal microscope and laser excitation at 532 nm. A 620 nm band-pass filter was placed in front of an avalanche photo-detector to collect light at the 2D-band (1600 cm^{-1}) of the Raman signal for Figure 2.6(b). The lighter colors indicate thicker regions, and the Raman spectrum of the different layers in Figure 2.6(c) shows the three layers present in this flake to be single, bi- and tri- layer graphene. [35]

Before transfer, the surface was prepared by plasma cleaning in oxygen/argon plasma to remove organic contamination. Once the flake had been successfully transferred, the sample was annealed in nitrogen at 100°C for 10 minutes, to promote van der Waals bonding between the graphene flake and the GaAs surface. The sample was mounted in a closed-cycle optical cryostat for low-temperature (5 K) microphotoluminescence (μ-PL) measurements. A fiber-based confocal microscope was used to interrogate single quantum dots in the direction perpendicular to the plane of the QDs. μ-PL measurements were performed using a 780 nm diode laser, and the fluorescence was dispersed onto at 0.75 m spectrometer, then sent to a liquid-nitrogen cooled charge-coupled device (CCD) for low-light detection. The resolution of the μ-PL detection system was 50 μeV.

2.4.2 Spatial Characterization

As a first step to understand the graphene-based Schottky barrier in our device, we collected hyper-spectral μ-PL measurements from on and off the graphene flake, as indicated by the black arrows in Figure 2.6(a). In Figure 2.7(a), narrow-band, spatially localized emission is seen between 920 nm and 970 nm while moving the confocal laser spot above the graphene flake.

At approximately 14 μm from the gold contact, PL from the wetting layer is apparent, at 870 nm. For comparison, in Figure 2.7(b), the laser spot is moved over a comparable region of the sample, but away from the graphene flake. The dominant part of the spectra is the wetting layer luminescence, even though there are quantum dots present in this region of the sample.

The differences in hyperspectra are good evidence for the graphene-covered portion of the sample having an in-built electric field. The excitons are generated by

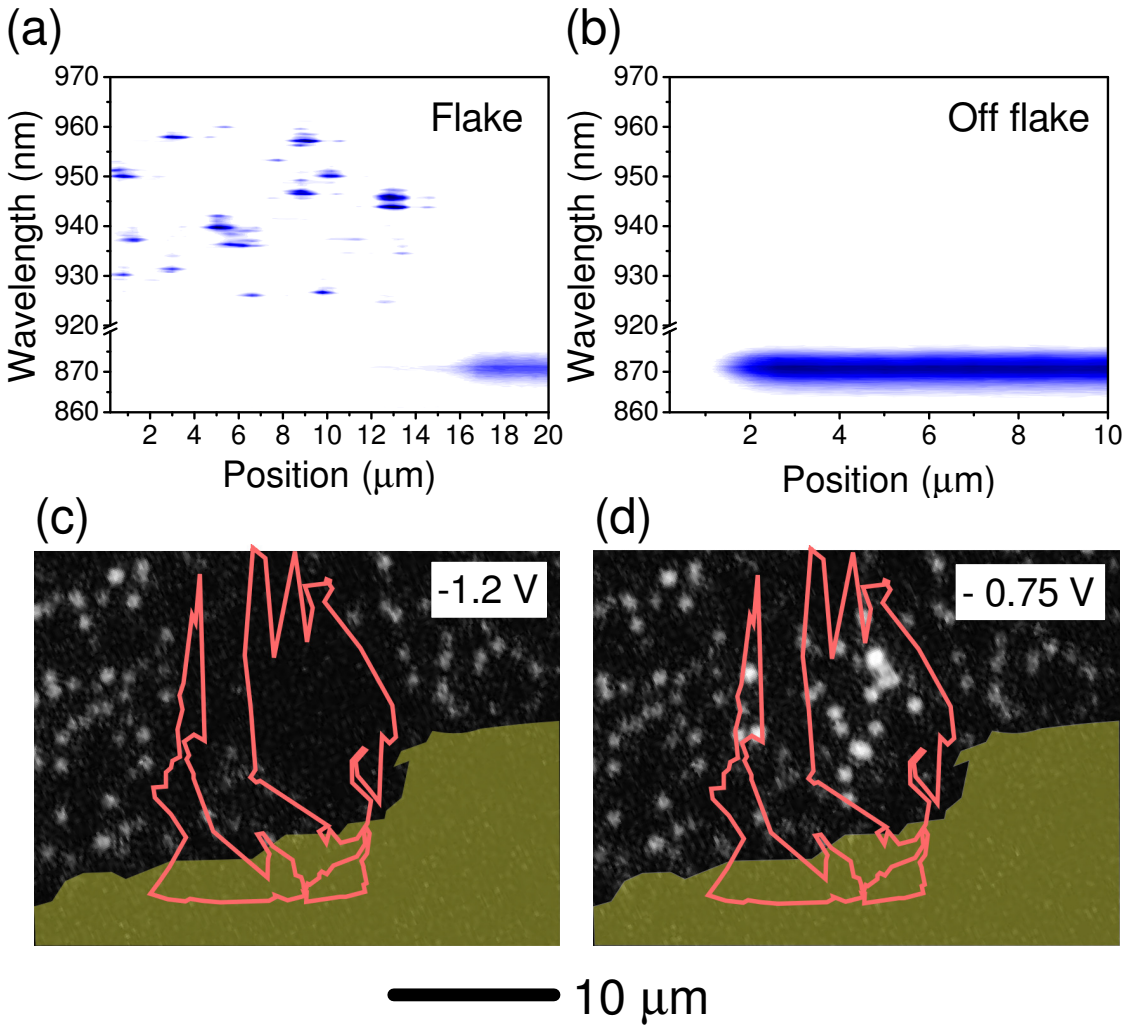

Figure 2.7: (a) Hyperspectra over the graphene flake at 0V. (b) Hyperspectra off of the graphene flake at 0 V. (c),(d) Wide-field images of the region surrounding the graphene flake at two different voltages. The gold contact completely absorbs the quantum dot photoluminescence, while the intensity is modulated under the graphene flake. The flake outline, derived from an SEM image of the device, is indicated by the solid line.

absorption of photons near 1.6 eV (780 nm), and non-radiatively relax into available states around the Fermi level until radiatively recombining. When there is no built-in electric field, radiative recombination is dominated by the short-lived wetting layer states. [36] Only at robust pumping rates (laser power) is luminescence from the quantum dots seen. However, when electrical contact to the surface is made and a Schottky barrier is present, the energy bands throughout the heterostructure are shifted, while the Fermi level is pinned by the back contact. This increases the tunneling rate into the quantum dots such that the wetting layer is effectively unpopulated until a large enough gate voltage is applied to counter the built-in field. The net effect is that even with no bias applied, narrow photoluminescence from fully confined quantum dot states dominate the spectral features when there is a built-in electric field. [37]

Further confirmation of the effect of the graphene flake is shown in the wide-field images of Figures 2.7 (c) and (d). The laser was defocused from the sample surface, and a 900 nm long-pass filter was placed in front of a second CCD camera to collect luminescence across the large emission range of the quantum dots, while blocking the emission from the wetting layer. The outline of the graphene flake (solid line) and position and edge of the gold contact (solid color background in bottom of image) was derived from a scanning-electron-microscope (SEM) image taken after transfer of the flake. The scale bar is the same for both images.

In Figures 2.7(c) and (d), the bright spots in the images indicate photoluminescence from 1 to 5 quantum dots. Application of a large negative gate voltage can completely suppress photoluminescence under the graphene flake, as seen in Figure 2.7(c) where the gate voltage is -1.2 V. Moving to a more positive gate voltage not only restore luminescence of the quantum dots under the flake, but it also enhances the emission, as the quantum dots are now more efficiently populated with excitons

than their non-gated counterparts. Figure 2.7(d) shows an example of this, with a bias of -0.75 V. The luminous intensity of quantum dots not under the graphene (outside of the flake border) remains unaffected at both gate voltages.

2.4.3 Voltage Dependence

In Figure 2.8(a) and (b) we present μ-PL spectra of a single quantum dot located under the graphene flake, as a function of applied gate voltage. We observe Coulomb-blockade plateaus indicating charge control over the ground state of the exciton emission, as well as Stark shifts on individual exciton features. [3] The linecuts in Figure 2.8 at the center of each charging plateau show resolution-limited linewidths for the neutral exciton and singly charged (both negative and positive) trions. We also observe higher charged excitons as well as the bi-exciton, but focus the comparison on the neutral and singly charged excitons. We contrast the graphene-gated quantum dot with a conventional NiCr thin-film (7 nm) device from the same wafer Figure 2.8(c) and (d).

In both devices, neutral and singly charged excitons can be observed with application of gate voltage, indicating tunneling of electrons between the quantum dot and the back contact. The differences in extent and location of the charge-dependent plateaus are due to specific dot-to-dot variations, as well as the slight difference in built-in voltage. Differences in the exciton charging energy match those described by previous spectroscopic observations. [3] Specifically, the negatively charged exciton emission is red-shifted by approximately 5 meV from the neutral exciton transition, and is found at a more positive gate voltage than the neutral exciton. The positively charged exciton is found to be blue-shifted by approximately 1 meV, and is populated at a more negative gate voltage.

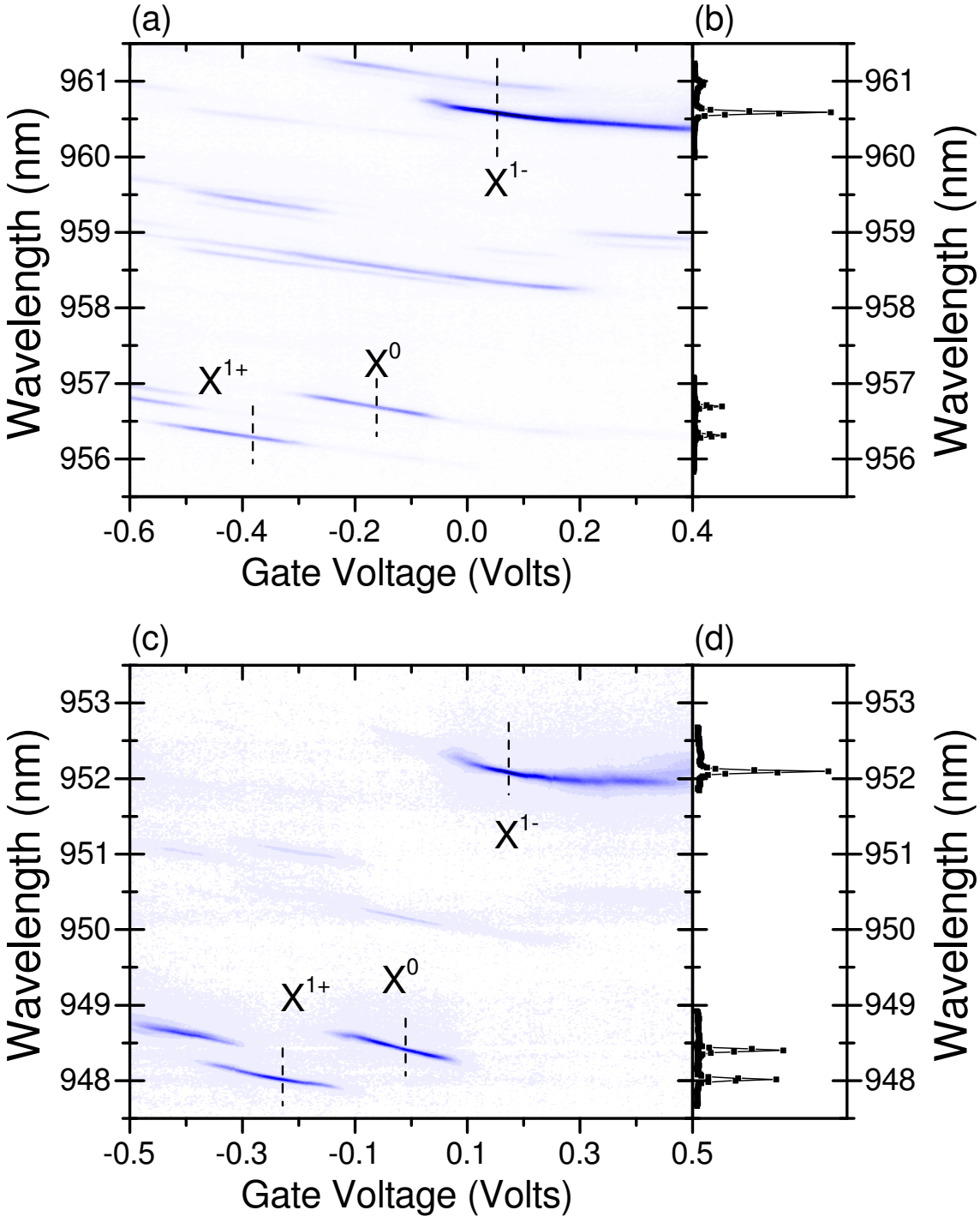

Figure 2.8: Gate-voltage dependent photoluminescence of a single graphene-gated quantum dot (a) and a NiCr-gated quantum dot (c). Indicated is the ground-state charge configuration. Both dots display Coulomb-blockade plateaus for charging the ground state and the quantum-confined Stark effect. The dashed line indicates the line cut for panels (b) and (d).

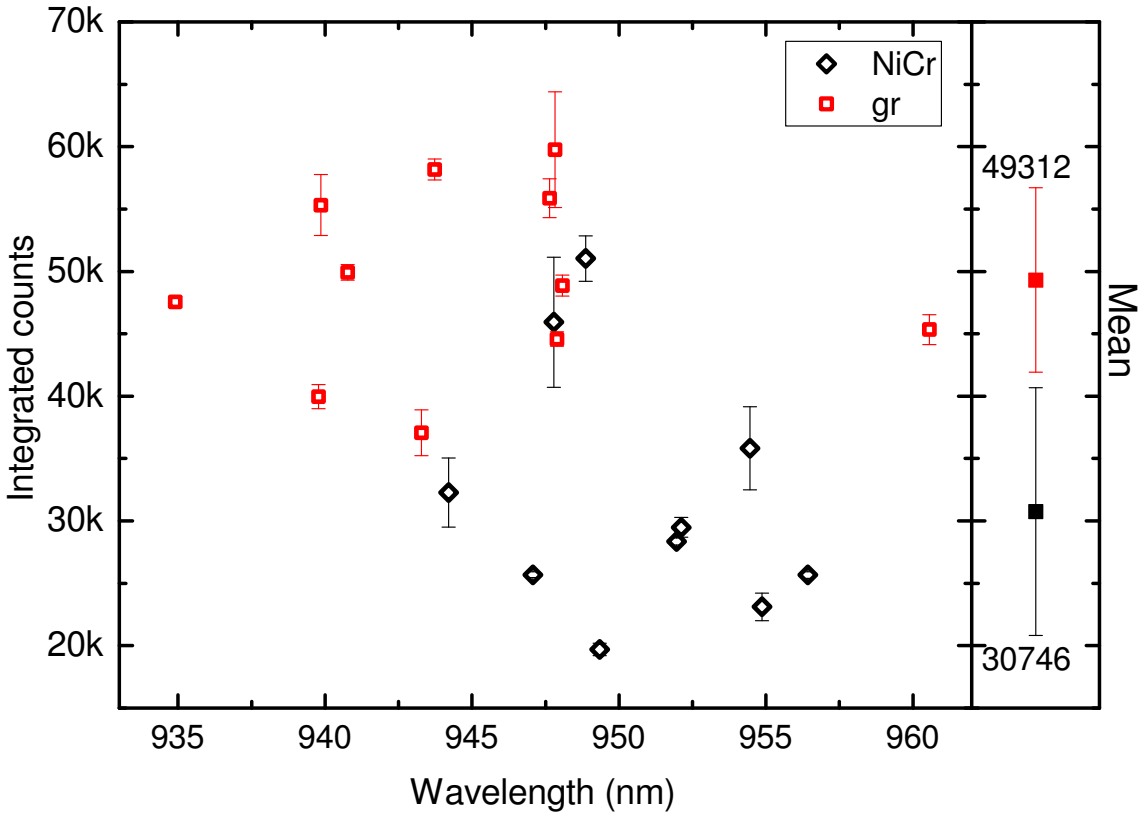

Figure 2.9: Maximum PL counts in 10 seconds, integrated across the FWHM of quantum dots underneath graphene (red squares) and NiCr (black diamonds). Absorption in the NiCr gate reduces the maximum counts on the detector by 30%, consistent with a 7 nm thick film.

Table 2.1: Permanent dipole moment, p/e (nm), and polarizability, β ($\mu eV\text{cm}^2/\text{kV}^2$), for InAs quantum dots, as measured by Stark-shifted photoluminescence for two Schottky materials.

	Graphene Flake (8 dots)		NiCr thin film (10 dots)	
Exciton	p/e	β	p/e	β
X^{1+}	-0.205±0.289	-0.027 ±0.412	-0.058 ±0.164	-0.685 ±0.539
X^{0}	-0.186 ±0.208	-0.205 ±0.535	-0.321 ±0.203	-0.238 ±0.518
X^{1-}	-0.184 ±0.125	-0.483 ±0.119	-0.153 ±0.134	-0.638 ±0.365

To quantitatively evaluate the graphene as a replacement for a metal electrode, we analyze the field dependence of the photoluminescence using Equation 2.3, applied to the neutral exciton and singly charged trions. [24, 38]. We used low-temperature photocurrent measurements to identify the flat-band condition(V_{bi}), and was 0.39 V for the NiCr device and 0.30 V for the graphene device. For 8 (10) QDs under the graphene flake (NiCr film), the measured dipole moments and polarizability for X^{1+}, X^{0} and X^{1-} are shown in Table 2.1. The two cases agree well, indicating that the capacitive relation $F = \frac{-(V-V_{bi})}{d}$ holds well for the graphene gate.

2.4.4 Single Photon Source Performance

Lastly, we considered the impact of a graphene gate as a means to minimize photon loss in the device. We measured both the NiCr and graphene device under identical operating conditions. For each device we recorded photon counts from ten different quantum dots. For each dot the excitation laser power was increased until the quantum dot light emission reached the saturation regime. 10 successive spectra were acquired to generate the mean and standard deviation in count rate for each dot. Figure 2.9 summarizes our findings, where we have integrated across the full-width-half-max for each spectra. We observe that the mean count rate from the NiCr device is approximately 30% lower than the graphene device. This is consistent with photon

loss due to absorption in a 7 nm thick NiCr film.

2.5 Conclusion

In conclusion, we demonstrate a new approach to electrical control of the photoluminescence from single InAs quantum dots, which involves replacing a metallic thin-film with single to few layer graphene. We have quantified the performance of the graphene device against a traditional device, and found that there is no difference in electrical control, and have quantified the gain in the amount of photons collected from the graphene device. Our method of electrical control will be advantageous in challenging environments such as photonic crystal nanocavities and miniaturized devices due to the inherent small size of exfoliated graphene flakes.

Chapter 3

Potential Energy Sensing from Single Quantum Dots

Metrology is the science of measurement, and the development of new techniques to acquire measurements. Recent work has demonstrated the high sensitivity of single InAs SAQDs for sensing both static and oscillating electric and magnetic fields. We build on this work to study variations in electric potential energy. Our long-term goal would be to develop InAs SAQDs into a platform for imaging metrology. This chapter will start by motivating the use of imaging metrology in electric transport physics, then detail which types of physics are currently addressed by various imaging methods.

With this detailed background, we then take the first steps to making an imaging sensor from an array of InAs SAQDs. We will examine what makes InAs SAQDs sensitive to variations in electric potential energy, then detail the measurement procedure for a single QD, and finally abstract the measurement scheme to an array of points.

Electron transport is a subject of great interest within solid state and condensed

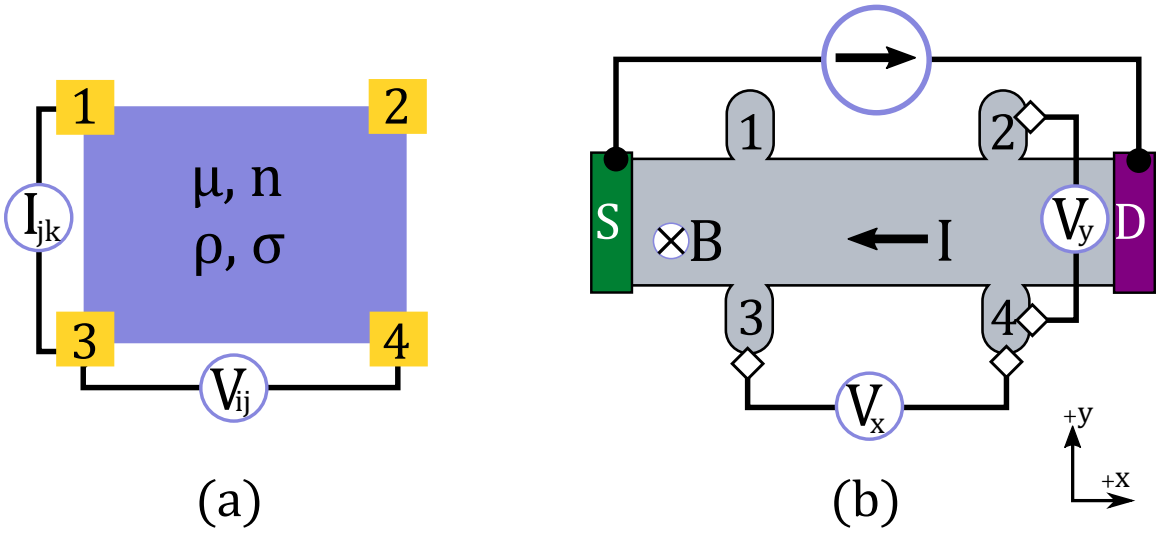

Figure 3.1: Example of transport measurements (a) van der Pauw geometry - ohmic contacts (gold) are made to the sample (gray). As current is injected through one pair of contacts, the voltage drop across a second pair of contacts is measured. When iterated, this gives accurate measurements of the resistivity of the sample. (b) Hall bar geometry - Current is injected through the contacts labeled source/drain. A magnetic field (out of plane) deflects charge carriers, such that a voltage (V_y) is measured in the orthogonal direction.

matter physics, as it reveals the central character of a material's band structure, and has led to several important physics discoveries such as superconductivity and the Quantum Hall Effect (QHE). Transport measurements are a standard set of tools used to measure how charges move through conductors, semiconductors, and most recently discovered - topological insulators. Connections to fundamental quantities can be seen in certain regimes of electron transport, such as the quantum hall effect (QHE). In the past 20 years, the National Institute of Standards and Technology adopted a resistance standard based on the fundamental quantum of resistance which is probed in the QHE [39]. Transport phenomena are a definitively interesting part of physics, yet there are still many challenges to simply relying on contact-based metrology.

A typical transport experiment would be to first make electrical contact at fixed

points on the outer edges of the material. Let's say that we were interested in measuring the superconducting transition temperature of aluminum foil. We know that superconductivity is a zero-resistance state of the material, thus we might attach electrical leads to pass current through the material, and measure the resistance of current flow. While keeping the current between the two leads fixed, we can then cool the entire experiment down, and plot the resulting resistance vs. temperature. However, the measured resistance is not equivalent to the intrinsic resistivity of the aluminum foil- there are many sources of resistance in our whole circuit, and this is the resistance we measure. For example, the leads we are using might be of copper with a different resistivity than the aluminum foil. Additionally, there is a contact resistance between the two materials (leads and foil), which will impede current flow. Depending on how exactly the experiment is set-up, we might not be able to measure the low resistance seen in the superconducting state.

To compensate for these problems (and many others we haven't mentioned), a few common geometries are used in studying superconductivity and the QHE. Figure 3.1(a) — known as a Van der Pauw technique — is used to quantify the sign and magnitude of charge carriers in the conducting region by attaching four leads around the edge of the sample. Note that although this cartoon has a square-shaped sample, the boundary of the material does not have to be well-defined. The placement of the contacts, however, should be symmetric and well-thought out. By iterating which pairs are used for sourcing and measuring, a set of 8 measurements can remove experimental artifacts, and accurately measure the resistivity of the material. In our example above, we can proceed with a measurement of superconductivity by repeating these measurements at various temperatures. Other realms of transport may vary the carrier density (through a gate voltage), magnetic field, or other external parameter. Another common geometry is shown in Figure 3.1(b), known as a Hall bar due to its

widespread use in measuring the classical and quantum Hall effects. The schematic shows a typical Hall experiment, where a current is passed through the main part of the sample in the presence of an out-of-plane magnetic field. Voltage probes at the sides of the current will probe the material resistance ($R = V_x/I$) and the Hall resistance ($R_B = V_y/(neB)$).

Although such contact-based transport measurements will always play a central role in metrology, they report global averages of electron (or hole) behavior. In some realms of physics, notably the fractional QHE and ballistic (wave-like) electron transport, there exists rich structure in the electron trajectories on the interior of the conductors. Although we could keep adding more contacts into a Hall-bar configuration to try and trace out these trajectories, this type of scaling would ultimately give a limited amount of additional information before inducing back-action on the electrons themselves. In particular, using point-based detection cannot easily distinguish between bulk and edge conduction in topological insulators.

As we mentioned in Chapter 2 , single-layer graphene has extraordinary transport behavior in part because of its high mobility, ambipolar carrier statistics, and access to different types of edge conduction. [26, 40–43] However, although high quality material is relatively easy to produce by exfoliation, the small and irregular shape sizes present a unique challenge for creating the well-defined geometries necessary for transport measurements.

We have established that the forefront of understanding electron transport in a variety of situations has exceeded the use of point-based contact metrology. There are a number of methods that have been developed for non-contact measurements of currents and electronic structure within a sample. Techniques to probe length scales smaller than the diffraction limit of light-based microscopy ($\approx$ 500 nm) have been successfully applied to materials characterization and physics of 2-dimensional

systems. These can be broadly split into three categories:

Non-contact metrology methods: Broad strokes

- Point-based probe which is raster-scanned across the sample
- Secondary system which is optically active and couples to the target system
- Intrinsic optical properties of the system which reflect electronic structure changes

Scanning probe microscopy (SPM) techniques are used for a wide range of metrology, and we will restrict our description to techniques used to probe the transport physics of 2-D systems [44–55]In general, a probe comprised of a cantilever is held (mostly) parallel to the plane of the sample with a metallic tip that reaches to the sample surface. The probe is held at an approximately fixed position by piezo positioners and active feedback electronics. The type of probe used will be determined by the type of measurement being made. For example, in magnetic force microscopy, a magnetized tip can be rastered across a sample surface to register different grain boundaries of nickel based on the resulting force felt by the tip. This is different than using a miniaturized magnetometer, which can directly measure magnetic flux or field strength. Versions of SPM relevant for transport measurements include scanning gate microscopy, scanning SQUID (superconducting interference device) microscopy, scanning capacitance microscopy, and scanning fluorescence microscopy.

The above techniques have been used to generate real-space images of the magnetic field from the currents of edge conduction in a topological insulator, edge transport in the QHE, coherent conduction in graphene, and cyclotron orbits in graphene. [56–60]

The scanning fluorescence technique we consider is the optically detected magnetic resonance of the nitrogen vacancy defect state in nano-diamonds [61]. This ‘color

center' is similar to InAs QDs in that it has discrete energy levels, hosts a spin-1 triplet system in its ground state, and can be optically addressed. A significant advantage of NV-centers as point-defects is the homogeneity in electronic structure — that is, all NVs are created equally. This allows for techniques such as optically detected magnetic resonance (ODMR) to be used. ODMR relies on the fluorescence count rate difference between the $m = +1$ and $m = -1$ fine structure, and has resulted in NVs widespread use as a sensitive magnetometer. When nanocrystals of diamond with NVs inside are attached to a scanning tip, the fluorescence can be read out and used to image vector magnetic fields in a variety of samples [62–64]. NVs can also be used to create stationary magnetic probes. An NV-imaging sensor can be created by forming a dense array of NV centers in electronically pure diamond. A sample with a varying magnetic field is then deposited above the color center array, and the ODMR read-out sequence is performed while a CCD images the entire diamond chip [63]. Similar to the SQUID scanning microscopy above, the NV sensor is used to detect magnetic fields due to current flow. In an exemplary study of graphene, vector magnetometry was used to re-construct vector current density along a 20 μm wide (500 μm long) channel of patterned CVD graphene. The only contacts to the sample in these diamond-imaging experiments were the source and drain to drive the current flow [62, 65].

Lastly, we consider measurements where the optical response of the sample is used to infer the electron transport dynamics [66–73]. Due to the variety of methods utilizing optical spectroscopy, we have restricted the examples to those which represent a pioneering link between an optical method and a type of transport physics. In an early version of imaging quantum hall plateaus in a 2DEG [70], the electro-optic effect was used to map the electrochemical potential of a GaAs/AlGaAs heterostructure. In this experiment, circularly polarized sub-bandgap light was focussed onto

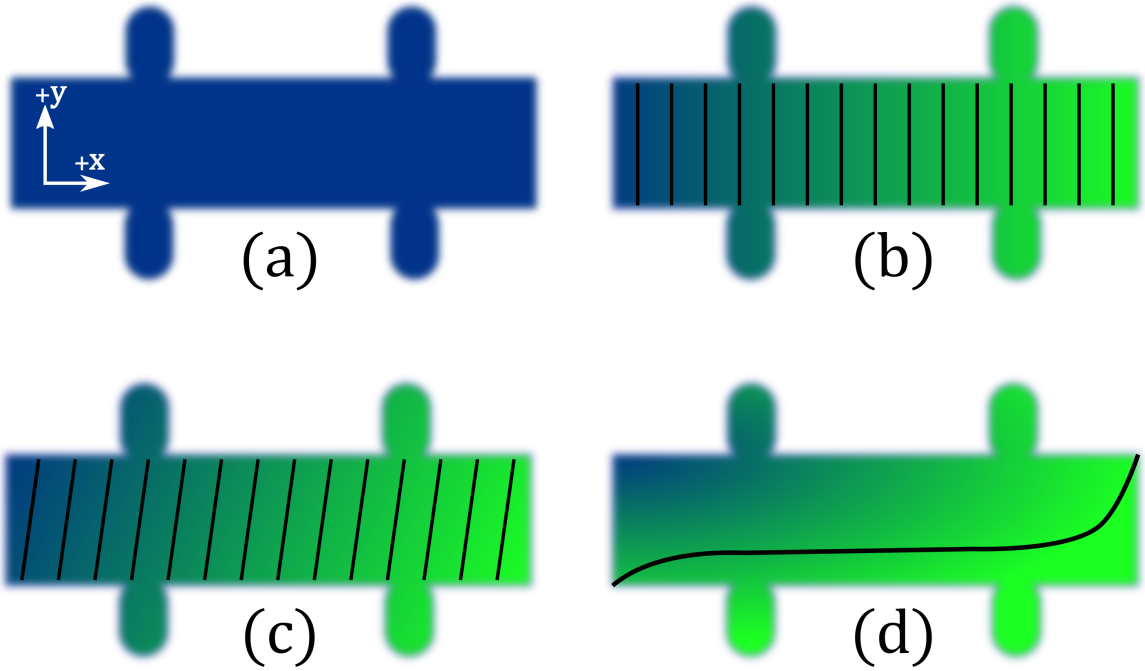

Figure 3.2: Simple voltage profiles based on the Hall Bar geometry. (a) Uniform potential everywhere (b) Linear potential drop along **x**, equipotential lines along **y** (c) Tilted potential, as seen in the classical Hall effect. Equipotential lines form at an angle to **y**, proportional to the strength of the driving current and magnetic field (d) Non-linear potential drop, as seen in the integer quantum Hall effect. Equipotenial lines follow an s-shape across the Hall bar.

the sample, and variations in the local (electrochemical) potential energy caused a rotation of the polarization angle. This change was detected and recorded as the laser beam was rastered across the sample. The experiment was able to image potential energy distributions similar to those shown in Figure 3.2 (b)-(d), where the black lines represent equipotential contours.

Photoluminescence spectroscopy of a 2DEG can also be used to observe changes in the electron transport. In a recent body of work [46, 71], spatially resolved PL of trion peaks was correlated to the existence of a fractional quantum hall spin liquid in different magnetic phases. The relative intensity of $S = 0$ vs. $S = 1$ spectrally distinct trions was the figure of merit, and how the authors translated the 2DEG

optical properties into a measurement. The intensity of these peaks maps to the electron spin polarization, thus relative changes were linked back to local magnetic fields acting on the unpaired spin in the ground state of the trion. Most recently, this technique revealed that the striped nature of a fractional quantum hall state can extend over several microns [71].

Thus far, our discussion of optical microscopy as applied to non-contact transport metrology has been through optical means (limited by the diffraction limit), or as in the case of NV-defect magnetometry, required complex inverse Biot-Savart calculations to arrive at the local current density from the measured magnetic field. Our goal in this chapter is to establish how optically active SAQDs will fit in this metrology realm, and we are not alone in applying QDs to metrology. In two similar measurements [74, 75], the spin population of a QD was related to the Fermi distribution of carriers in a Fermi sea, thus allowing the optical signal from the QD to relate to the temperature of the electron reservoir. In another well-executed experiment, [17] a time-trace of resonant PL was studied in the frequency domain, thus turning the QD into a noise sensor. This experiment used both neutral and charged excitons, and was able to distinguish the two noise primary noise sources as electric (low-frequency) and magnetic (high-frequency) noise.

Most promisingly, recent work has shown that InAs SAQDs are very sensitive electrometers [16]. By measuring an intensity change in resonant photoluminescence excitation, the presence of an extra electron approximately 12 nm away from the stationary probe QD was detected. The intensity change is based on the Stark effect described in Ch. 3, and the experimental sensitivity was achieved in part due to the use of resonant photoluminescence excitation. InAs SAQDs are therefore a good candidate to build an imaging sensor due to their small size which allows sub-diffraction limit spatial resolution on changes to the local electronic transport environment.

We have reviewed traditional transport metrology, and detailed a few ways in which non-contact methods have been developed to further the exploration of quantum transport. The remainder of this chapter is dedicated to developing SAQDs as a sensor for use in non-contact transport experiments. The first step in using SAQDs as a sensor is to describe the metric by which we measure a change in local potential energy through Stark Shift spectroscopy. The methods to collect the signal for the proposed metric will rely on confocal, non-resonant PL microscopy of single excitons in SAQDs, as described in earlier chapters.

Description of the sample We start with a Schottky-diode sample as shown in Chapter 3, which provides charged QD emission and a vertical electric field to impart a Stark shift on individual excitons. We add a second point of contact to the top Schottky material (NiCr). In principle, this will impart a lateral electric field on the SAQD as well. However, the distance between the lateral contacts is macroscopic, approximately 1.2 mm. In light of the small distance between the two vertical contacts (150 nm), the electric field in the in-plane direction is much less than that for the vertical direction. Thus, any energy shift due to the quantum confined stark effect is taken to be strictly due to the vertical electric field. This assumption is also quite valid because the in-plane dipole moment is much smaller (or non-existent) compared to the vertical dipole moment. [76, 77].

When we apply a DC voltage between the two lateral contacts, the potential energy drop across the thin film varies approximately linearly, as shown in the contour of Figure 3.3 (a). A QD at a particular spatial position along this voltage drop will have a PL signature which maps to this local voltage, V(x). However, because each QD has a unique emission energy and thus gate voltage response, the PL signature doesn't have a universal meaning, thus the voltage-dependent PL must be calibrated

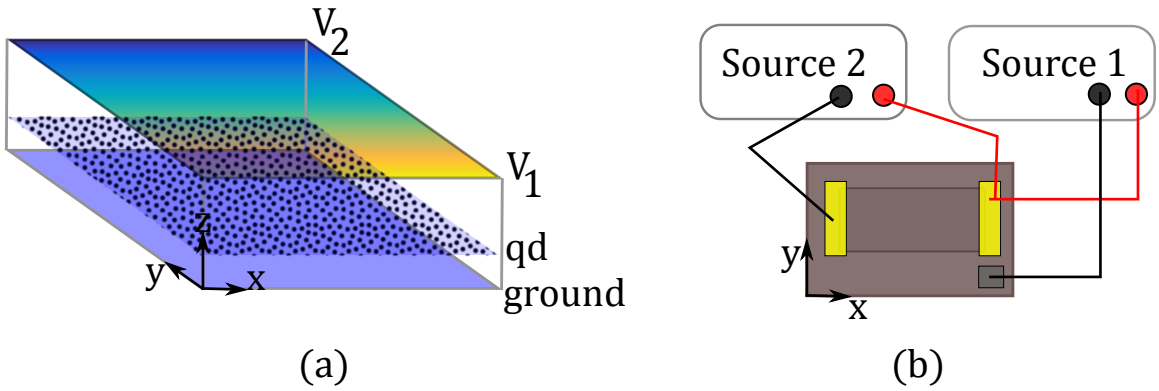

Figure 3.3: (a)Side-view schematic of layer structure with the top Schottky contact having a linear voltage drop. (b) Circuit configuration for two voltage sources and three contacts to the QD device. The right-most top contact serves as a common hi voltage, thus the local potential at a QD is V_1+V_2(x), where the spatially dependent voltage is produced by source 2. Source 1 it swept, as V_g in the gate-dependent photoluminescence experiments.

for each QD. The circuit diagram for the double-gating condition is shown in Figure 3.3 (b). Three contacts are made on the surface of the sample - two contacts (gold) to the surface Schottky contact at a distance L apart, and an Ohmic contact (grey) to the buried Fermi sea. When source 2 = 0 V, source 1 sweeps the top voltage in the same way as discussed in Ch. 3. When source 2 $\neq$ 0V, a linear potential drop

$$V(x) = \frac{V_{source2} \cdot x}{L} \tag{3.1}$$

is present across the two top contacts, and results in a variation of the local potential for each QD.

Therefore, the experimental procedure is to park at a location, map out the QD voltage response without a lateral potential ('gv1'), and then apply a fixed lateral potential and repeat the voltage mapping procedure ('gv2'). This procedure is repeated for several QDs between the two contacts, and the same fixed lateral potential is used. We then analyze the differences between the two gating situations. The

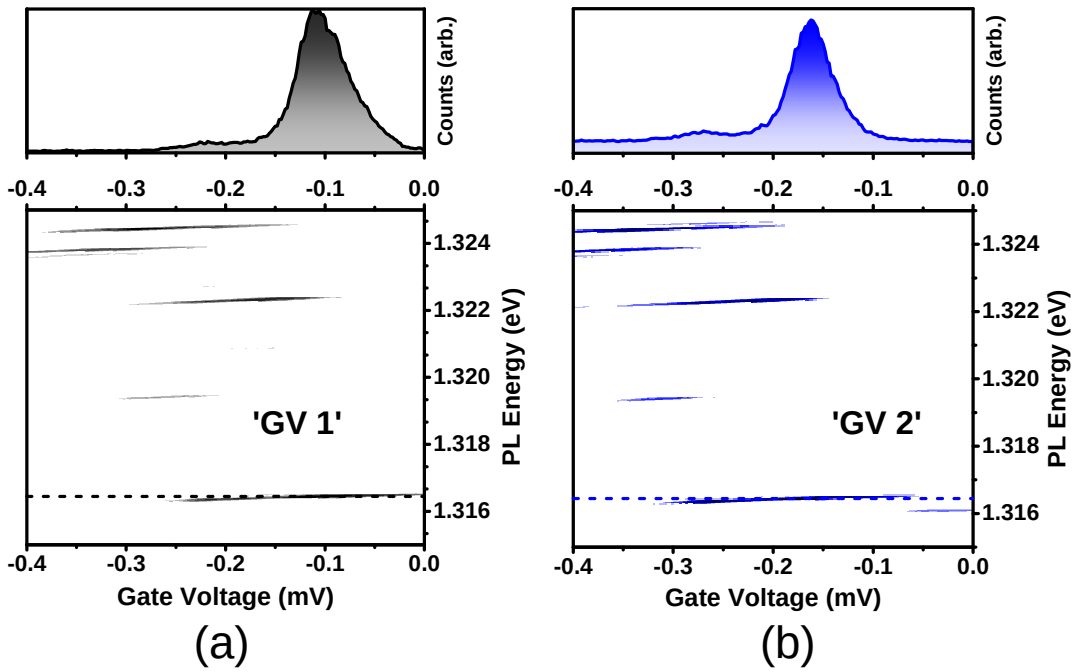

Figure 3.4: (a) Voltage-dependent PL map with source 2 set to 0V. This gating condition will be referred to as 'GV1'. (b) Same as (a) but with source 2 set to 50 mV. The PL features are shifted in the x- axis (source 1 voltage) due to the local change in potential energy imparted by source 2. (top) Linecut at constant energy, E =1.3165 eV for both gating conditions.

main experimental achievement in this chapter is to identify a procedure and measurement (metric) to read-out this local voltage. Sample positioning is achieved by piezo-electric positioners for all three axis, thus making this procedure similar to a scanning-probe microscopy. However, we are using an array of fixed probes similar to the NV ODMR sensor described above. Although the QDs used in this experiment are randomly positioned and have a wide range of PL energies, future versions of this experiment could take advantage of site-controlled QD growth to make a sensor which is well-calibrated in position.

3.1 QD Response at Fixed Point

To motivate the eventual analysis of these two gating conditions, we first present a side-by-side comparison of the PL spectroscopy maps for the two gating situations defined above. In Figure 3.4(a), we acquire PL as the vertical field is changed, in the normal situation without the lateral voltage. A linecut at constant energy (E=1.3165 eV) shows how the PL at that energy varies with gate voltage. The response is peaked due to a combination of Coulomb blockade and Stark shift effects. The counts peak at approximately -0.115 V. The lower-voltage, flat response is due to the presence of tunneling at those energies, but the main peak response is due to shifting the QD energy through this energy. Note that the energies we can choose for this constant linecut are limited by the resolution of our spectroscopy setup - in this case, $\approx 30\mu$eV. In Figure 3.4(b), we present the corresponding gated PL measurement, but with the additional lateral voltage of 50 mV. This QD is located at a position near the 'high' contact, thus we expect $I(V) = I(V + 0.05)$, where I(V) is the PL intensity response to an applied voltage. The constant energy linecut is clearly shifted, and peaks at approximately -0.16 V, consistent with the expected $V(x)$. For better comparison, in Figure 3.5, we present both linecuts side-by-side. The shift, δ is negative because in the second gating condition, we are taking $V \rightarrow V + 0.05$, and since V is our independent variable, this results in a negative shift for the dependent variable.

Thus far, our analysis procedure has been to identify a constant energy linecut within the charging plateau of the negative trion, where the PL counts have a well-peaked response. To analytically compare the original ('gv1') and shifted ('gv2') signals, we first cross-correlate the two signals, then find the maximum of the result. The voltage at which the maximum in the cross-correlation occurs is sensitive to the

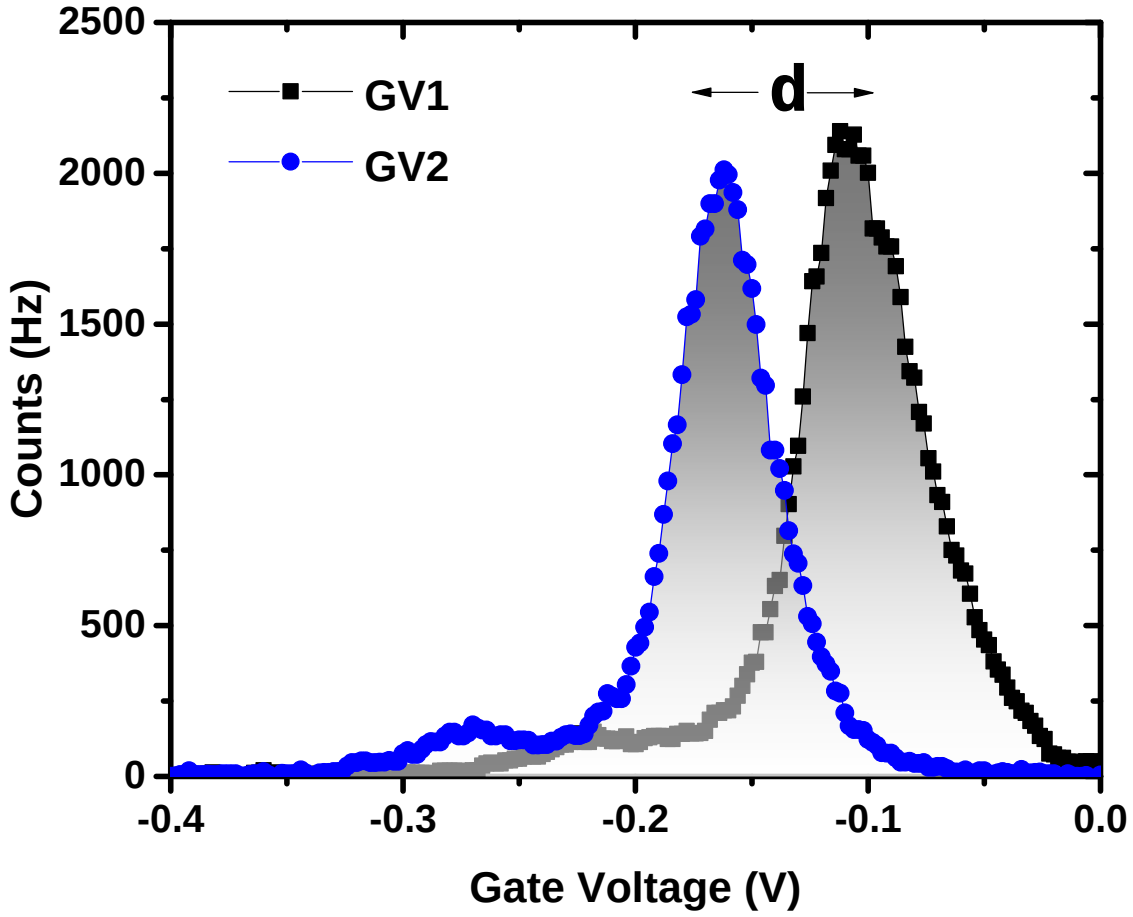

Figure 3.5: Linecuts from 3.4 showing a pronounced offset in the two gating conditions. Cross-correlation analysis is used to measure δ, which is 58 mV.

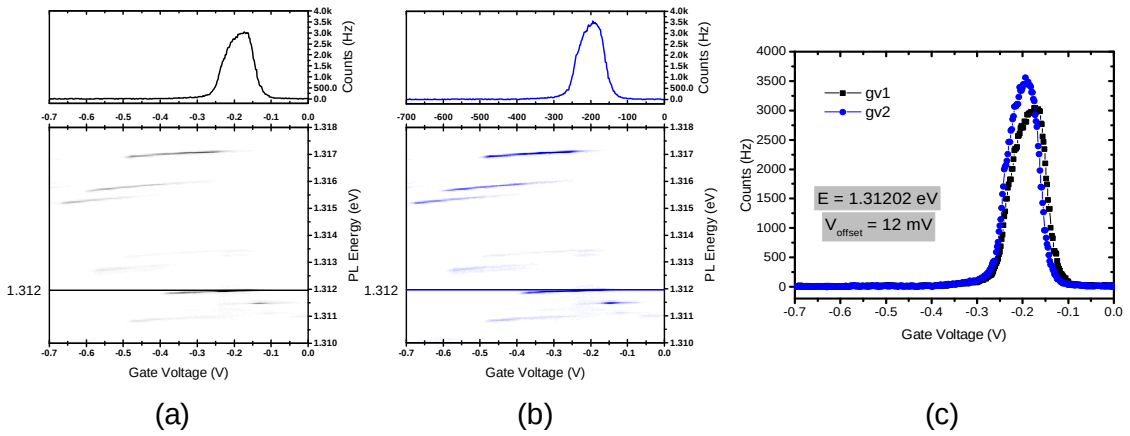

Figure 3.6: (a) Gate Voltage Dependence with source 2 = 0V, at a QD farther away from the hi contact (b) Same, with source 2 = 50 mV (c) Shifts between linecuts at constant energy are less pronounced due to the voltage profile

voltage 'delay' in the two signals.

$$V_{offset} = max(f * g)(V)$$

where signal 'f' is 'gv1', 'g' is 'gv2', and the $*$ represents the convolution of the two signals. For the QD in Figure 3.4 and 3.5, V_{offset} = 58 mV.

Note that the constant energy we chose is slightly arbitrary. In Figure 3.6 We present a correlation analysis across the entire GV plateau for a QD farther from the contact. Based on the position of this QD, for a top, lateral voltage of 50 mV, the QD should experience a local voltage of - we expect the local gv response to be 12.5 mV. The PL vs. gate voltage for this QD in both gating situations is shown in Figure 3.6(a) 0V and (b) +50 mV. The linecuts at constant energy E=1.31202 eV is shown in Figure 3.6(c), and the correlation analysis gives V_{offset}=12 mV. However, when we vary the constant energy linecut across the entire charging plateau, significant variations in V_{offset} are found.

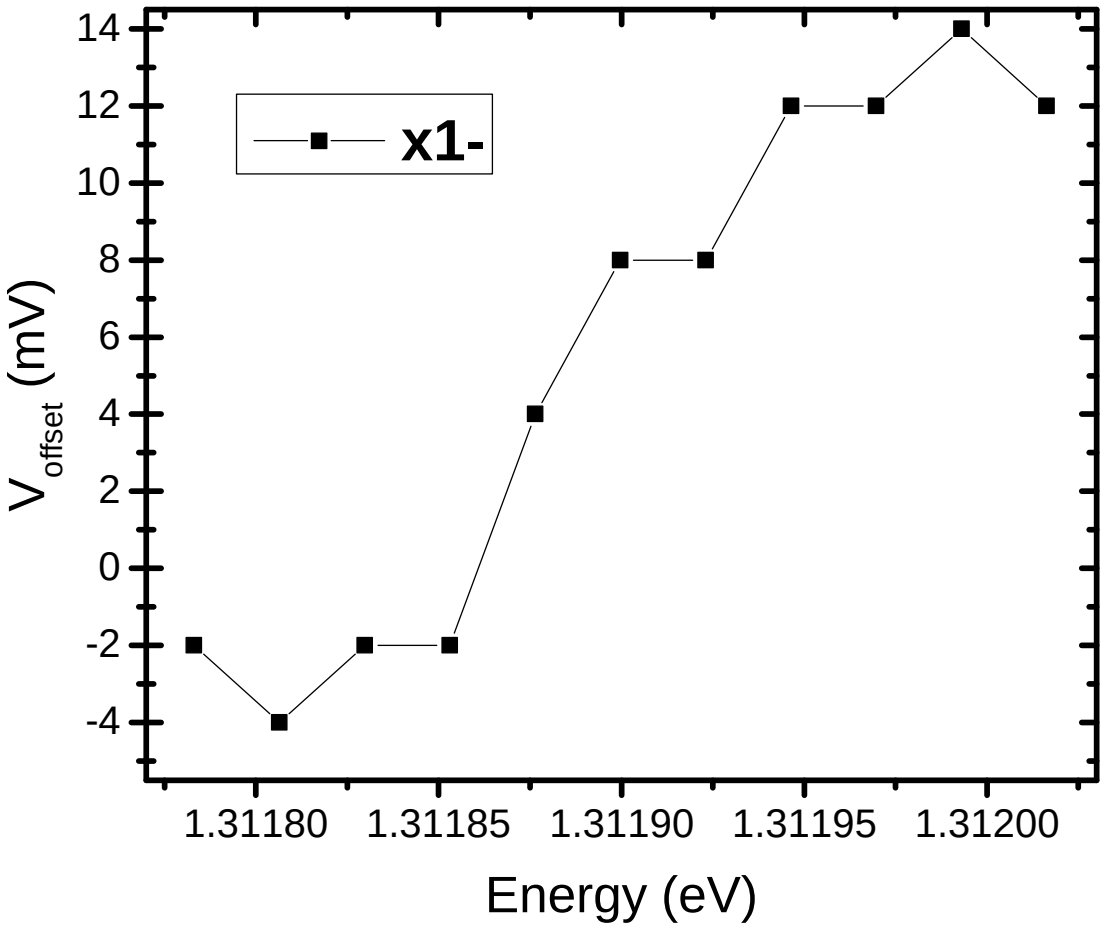

Figure 3.7: The measured offset is not constant as different PL energies are chosen for the constant-energy linecut. For consistency in measuring the voltage profile, energies at the blue-end of the charging plateau are chosen throughout the profile measurement.

3.2 Voltage Profile

Our overall goal in this experiment is to measure the profile imprinted on thin film at the surface of our QD device, which requires measuring the voltage response of several QDs at several location. In order to accomplish that, we constrain ourselves to the analysis above, and use a constant energy linecut which is towards the positive side of the charging plateau, and which has a Lorentzian-like peak shape. There have been several other analysis strategies considered, and a full review of them is not included here.

A voltage profile was built-up by measuring V_{offset} for several QDs along the length of the film between the two top contacts, and is shown in Figure 3.8, where we have included a measurement of V_{offset} from the neutral exciton charging plateau as well as the negative trion. The expected voltage profile was calculated by solving Poisson's equation in a thin film for DC conduction using MatLab's PDE solver environment. We can see the data matches the trend of the expected profile quite well. However, the level of uncertainty in the absolute measurement implies that further refinements should be made to the experimental technique or theoretical understanding of the measurement before being applied to an unknown voltage profile measurement.

3.3 Conclusion

In summary, we have explored the use of InAs quantum dots as a local, sub-diffraction limit sensor of potential energy variations. The procedure to measure a local voltage was described in detail, and demonstrated for a thin film approximately 100 nm away from the QD plane.

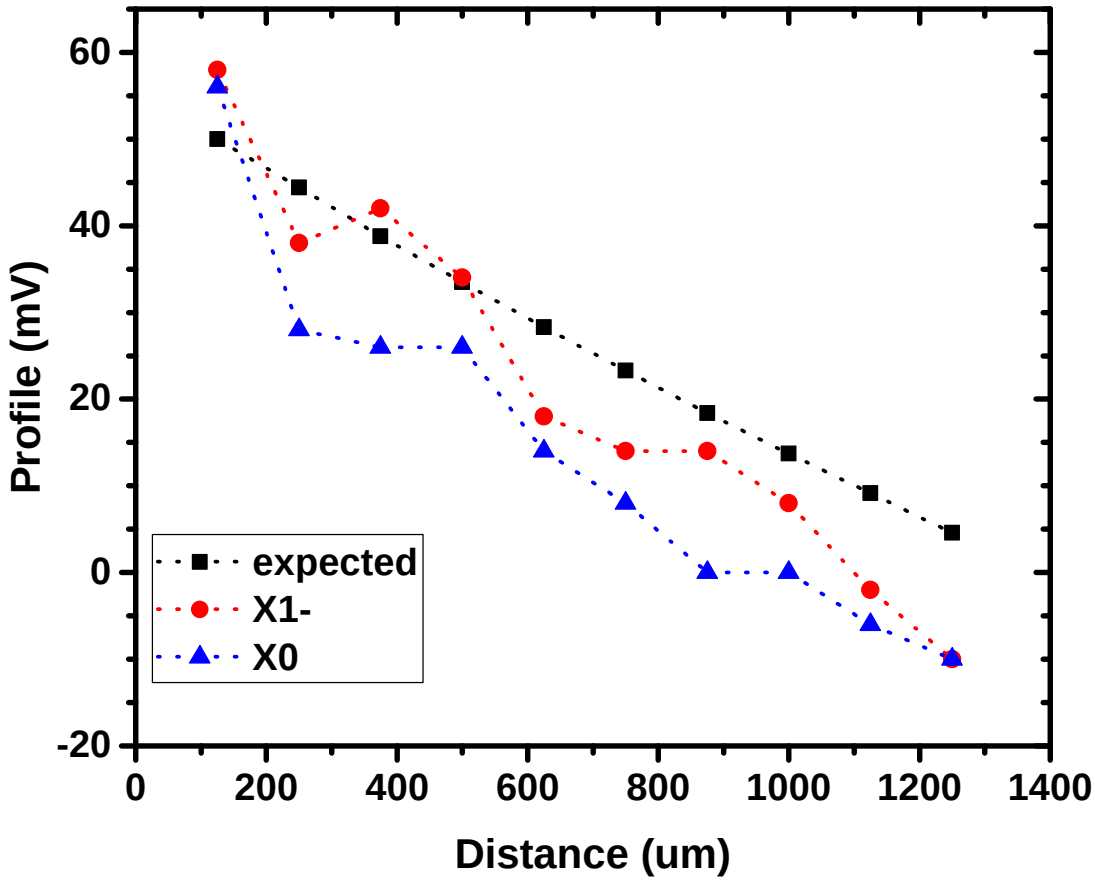

Figure 3.8: Quantum dot response to a voltage profile as described earlier. The offset voltage is used to measure local voltages, and when QDs are sampled systematically across the thin film, the voltage profile can be reproduced in the QD response.

Chapter 4

Spin-Photon Interfaces

Recent proposals of quantum computing have pointed out the usefulness of a confined single electron spin as a quantum bit (qubit) for storage of quantum information. [10, 11,78–80]. Spin qubits for quantum computing rely on manipulation of single particle spins with a magnetic field. Particularly interesting are spins that can reversibly connect to optical photons, generally through the polarization state of the photon which can then carry the spin information (via the photon's polarization state) to another location or computation. In this chapter, we describe how to realize a spin-photon interface in InAs quantum dots by understanding the QD response to an external magnetic field. We see how the X^{1-} transition of InAs QDs has both excited and ground state splitting in a magnetic field. A brief review the fine structure of the X^0 and X^{1-} transitions in a Faraday-oriented magnetic field begins our discussion, as described in [81].

Notation	Parameters	Effect
δ_0	$1.5(a_z + 2.25b_z)$	Splits M=1 and M=2
δ_1	$0.75(b_x - b_y)$	Fine structure of M=1
δ_2	$0.75(b_x + b_y)$	Fine structure of M=2

Table 4.1: Notation used in describing how the electron-hole exchange interaction leads to observable fine structure.

4.1 Theory of PL Evolution in a Magnetic Field

4.1.1 Eigenstates in Zero Field

In Ch. 2, the energy level picture of SAQDs was introduced briefly, and the interband dipole transitions were established to have polarization selection rules in either the linear or circular basis. In Figure 4.1 (a) we give a more detailed view of the neutral exciton fine structure, as it arises from the short-range exchange interaction:

$$H_{exchange} = -\sum_{i=x,y,z} (a_i J_{h,i} S_{e,i} + b_i J_{h,i}^3 S_{e,i}) \tag{4.1}$$

The initial eigenstates are taken as : $|+1\rangle, |-1\rangle, |+2\rangle, |-2\rangle$. When the perturbation is calculated through, the net effect is to always hybridize the $M = 2$ eigenstates, and only hybridize the $M = 1$ eigenstates if there is reduced symmetry in the confinement potential. The reduction in confinement is inferred when a zero-magnetic field splitting is seen in the neutral exciton photoluminescence, with a magnitude proportional to the asymmetry. The splittings are defined in Table 4.1, and depicted in Figure 4.1 (a) along with the zero-field eigenstates. In the absence of asymmetry, the exchange splitting δ_1 goes to zero, and unmixed angular momentum eigenstates $|+1\rangle$ and $|-1\rangle$ are the eigenstates of the exciton. The splitting between the 'dark' ($M = 2$) states remains, independent of the symmetry of the dot.

Note that polarization of the outgoing photon is linked to the eigenstates of the

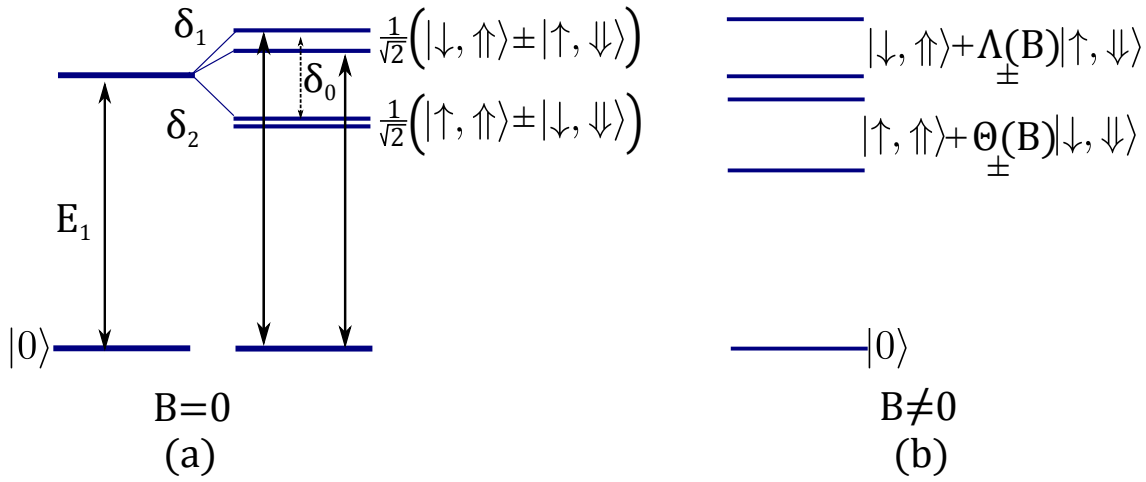

Figure 4.1: (a) The effect of the electron-hole exchange interaction on the energy and eigenstates of the neutral exciton. Even without a magnetic field, there is fine structure present in the PL spectra due to mixing of the bright states. (b) The evolution of the eigenstates depends on the strength of the magnetic field. Mixing angles Γ and Ω are defined in the text.

system. Since circularly polarized light carries spin angular momentum ± 1, we can see that right hand circularly polarized excitation, σ^+, connects to the $|+1\rangle$ state and left hand circularly polarized light, σ^- connects to $|-1\rangle$. Any mixing of the $|+1\rangle$ and $|-1\rangle$ states will be imprinted on the outgoing photon polarization - thus photoluminescence in a linear basis is to be expected for QDs with a finite fine-structure splitting.

4.1.2 Magnetic Field Evolution

When a DC magnetic field is applied along the growth axis (Faraday configuration), the Zeeman Hamiltonian describes how the zero-field eigenstates evolve:

$$H^F_{Zeeman}(B) = -\mu_B(g_{e,z} \cdot S_{e,z} - g_{h,z} \cdot J_{h,z})B_z \tag{4.2}$$

where μ_B is the Bohr magneton, g_i is the g-factor for the electron or hole, along the z-direction. We already know that the angular momentum states are not the

initial eigenstates, and the net effect of the magnetic field is to alter the hybridization of the ±1 and ±2 states within their own manifolds, as shown in Figure 4.1(b). The mixing coefficients are defined as:

$$\Lambda(B)_{\pm} = \frac{\beta_1}{\delta_1} \pm \sqrt{1 + (\frac{\beta_1 B}{\delta_1^2})^2} \tag{4.3a}$$

$$\Theta(B) = \frac{\beta_2}{\delta_2} \pm \sqrt{1 + (\frac{\beta_2 B}{\delta_2})^2} \tag{4.3b}$$

with (μ_B is the Bohr magneton):

$$\beta_1 = \mu_B(g_{e,z} + g_{h,z}) \tag{4.4a}$$

$$\beta_2 = \mu_B(g_{e,z} - g_{h,z}) \tag{4.4b}$$

The energy of the Zeeman-split transitions then becomes:

$$E_{bright} = \frac{1}{2}\delta_0 + \frac{1}{2}\sqrt{\delta_1^2 + (\beta_1 B)^2} \tag{4.5a}$$

$$E_{dark} = -\frac{1}{2}\delta_0 + \frac{1}{2}\sqrt{\delta_2^2 + (\beta_2 B)^2} \tag{4.5b}$$

Figure 4.2 shows the evolution in magnetic field (red= bright states, black = dark states) for a X^0 transition in a quantum dot where the electron/hole exchange (δ_0) is 200 μeV, the bright state splitting (δ_1) is 10 μeV, and the dark state splitting (δ_2) is 5 μeV.

The fine structure of singly charged excitons (Figure 4.3) follow the same general behavior as the discussion for neutral excitons above. However, because the electron-hole exchange interaction is more complex due to the three composite particles rather than two, there is very little perturbation of the degenerate states without a magnetic

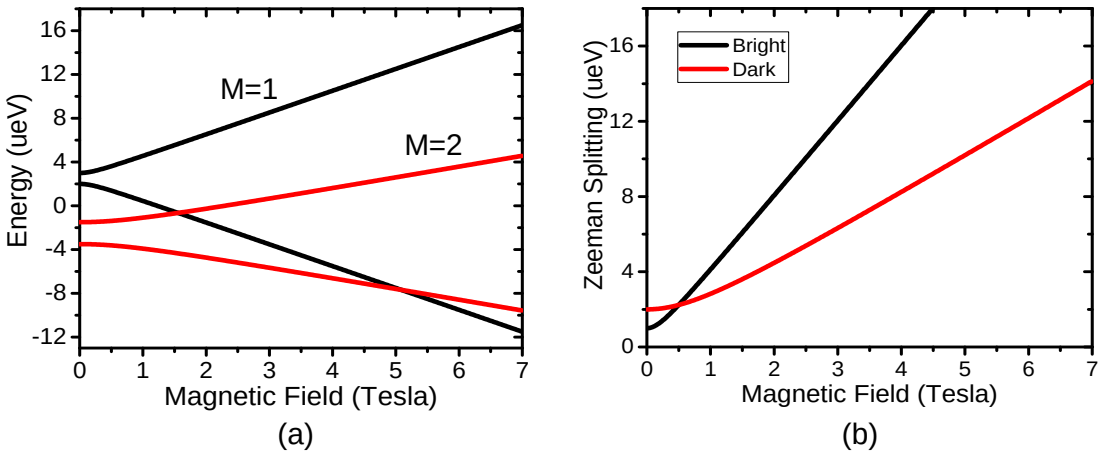

Figure 4.2: (a) Evolution of the four eigenstates of the neutral exciton in a vertical magnetic field. The M=1 and M=2 states are never mixed, but do cross each other. (b) Energy splitting between the M=1 and M=2 eigenstates. At low fields, the difference is quadratic. At high fields, the splitting is linear. The slope of the each curve is indicative of the combined (sum and difference) g-factors of the single-particle electron and hole g-factors.

field. Thus, as shown in Figure 4.3, the X^{1-} transition does not display any fine structure until a magnetic field is applied.

In its ground state, a singly charged exciton (either with an electron or a hole) has one charge carrier in the single particle s-shell configuration. It is this unpaired spin which interacts with the external magnetic field, thus causing a ground-state splitting as indicated in Figure 4.3. In the simplest excited state for the X^{1-}, eg., the two electrons form a closed spin system in the s-shell, and the hole spin dominates the interaction with a magnetic field. However, PL considers optical emission between the initial and final states which in this case are carried by opposite spins. Thus, the g-factor, which dominates the splitting and evolution of the spectral features, is identical ($g_e + g_h$) to that of the bright neutral exciton. Note that this assumes the excess charge is occupying its single-particle ground state, which is likely the case in a charge-tunable system such as described in previous chapters. There are many ways

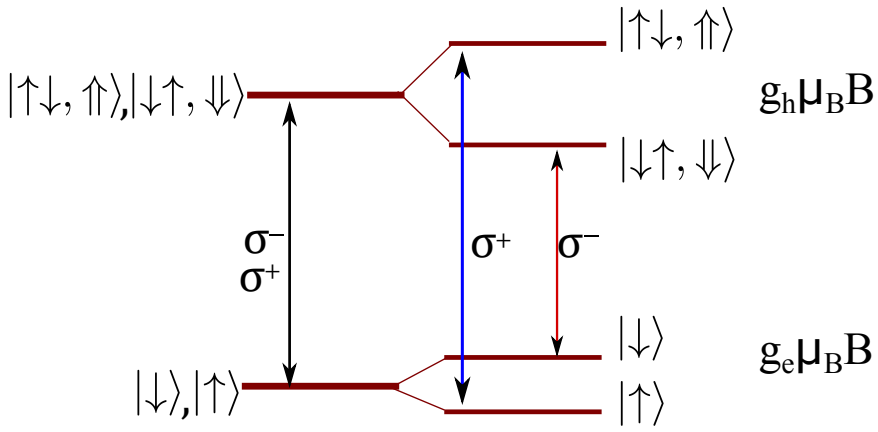

Figure 4.3: (left) The singly charged exciton is protected from the exchange interaction, and displays no fine structure in zero magnetic field. Two optically active transitions — corresponding to different spin projections – are degenerate in energy. (right) Magnetic field lifts the degeneracy in both the ground state and excited state. The two spin projections are addressed by optical fields of opposite polarization (in the circular basis).

for excess charge to enter the SAQD, however, and does not automatically guarantee the excess charge to be in the ground state. Thus, in un-gated samples, charged excitons may require careful consideration of the PL signatures.

4.2 Towards Telecom-band Emission

SAQD grown by strain-based methods [16] traditionally have optical transitions in the near-infra-red spectral region of 1.3- 1.2 eV (930 - 980 nm). The engineering of QD properties has focused on minimizing the X^0 fine structure to take advantage of the bi-exciton cascade. Commercial lasers have come into the market to serve this spectral range, allowing for the possibility of resonant driving. For some applications, however, it is advantageous to further explore the NIR wavelengths and push the understanding of QD physics out to the telecom bands (1260- 1675 nm for the entire band). In this chapter, we apply the QD physics discussed in Chs. 1 and above to

SAQD grown for PL emission near 1.1 eV (1000-1150 nm).

For the experiments presented in this chapter, we have used the microscope seen in APPENDIX, with an InGaAs camera as the sensor at the output of the spectrometer, and we used the attocube cryostat for magnetic field measurements.

4.2.1 Exciton Identification

The SAQDs are grown using the SK-technique mentioned in Chapter 1, and the heterostructure growth sequence is seen in Figure 4.4. In order to create emission at a longer wavelength, the InAs was made to be dome-like by giving it less time to re-flow. We first sample different regions of dot density to observe ensemble PL, as seen in Figure 4.4 (b). In the high density region, the PL from 1000 nm to 1125 nm has enough structure to identify the s- , p- and d- shell exciton populations. Once each electron and hole level is filled, there is a corresponding increase in energy as the next lowest energy states are filled. From the data, we can see that the charging energy for each of these is approximately 25 meV. In a medium-density region, we can still resolve the s- and p- shell emission, seen in Figure 4.4(c). This gives an indication of what energy range to monitor when looking for PL from single QDs, as the s-shell emission will be in roughly the same energy band, independent of QD density.

We are interested in studying PL from a single neutral exciton, and as we move to the low density region of the wafer, (seen in Figure 4.5(a)), we start seeing doublet features with a second peak approximately 2 meV away, reminiscent of the heuristics discussed in Chapter 1. To explore the excitonic origin of these lines, we next study the power dependence. The corresponding power dependence for the PL features highlighted in Figure 4.5(a) are shown in (b). One striking feature is the presence

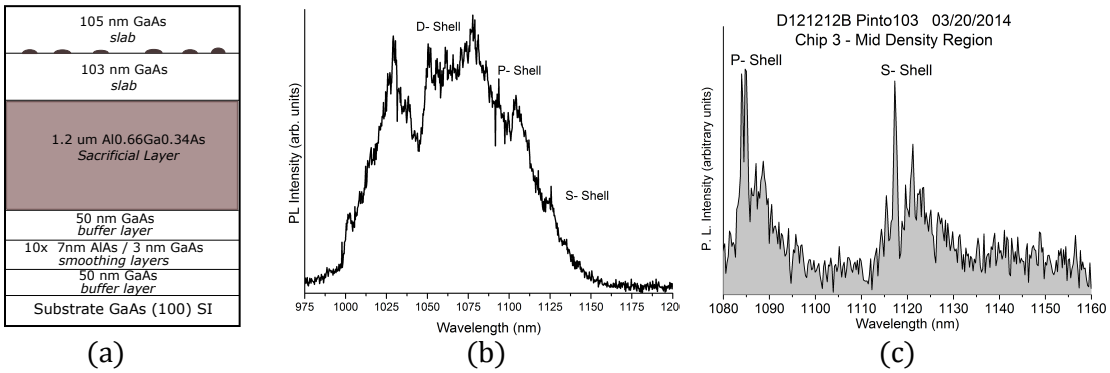

Figure 4.4: (a) Molecular beam epitaxy growth sequence for the sample investigated. (b)Photoluminescence (PL) spectra of high-density, ensemble quantum dots with pronounced atom-like shell sequence (c) PL spectra of a second region of the wafer, showing s-shell emission at 1120 nm.

of a satellite peak about 150 μ eV above the line labeled X^0. This is part of the fine structure of the X^0 transition. The SAQDs exhibit saturation behavior, with the low-energy part of X^0 displaying saturation well before the high-energy part. The fine-structure splitting, 100 μeV is much larger than that observed for higher energy SAQD, where the fine structure is $\sim 10\mu$eV. A large FSS suggests a large asymmetry in the confinement potential of the QDs, and this could indicate some bright-dark mixing in a magnetic field. The bi-exciton and positively charged exciton are also identified, due to both their saturation behavior and energy relative to the neutral exciton. The presence of excess holes — leading to the charged exciton PL— is not surprising as intrinsic GaAs tends to be lightly p-doped. This behavior was recorded in several (greater than ten) QDs across the low density portion of the sample.

4.2.2 Magnetic Field Behavior

The magnetic field behavior (up to 7 T) of 20 QDs was studied in order to understand the neutral exciton fine structure. A contour plot of magneto-photoluminescence data

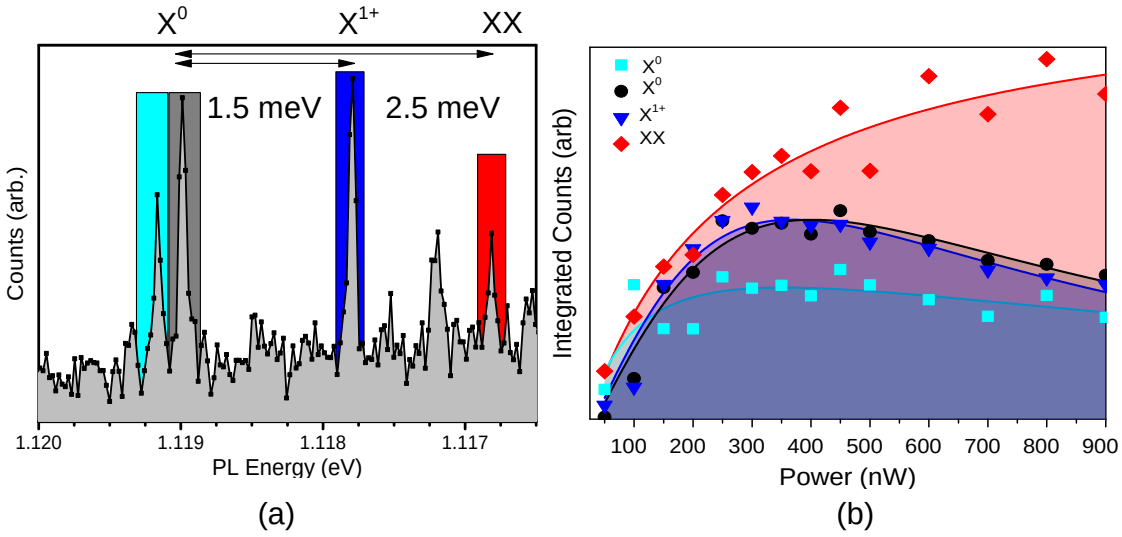

Figure 4.5: (a) Exciton identification for quantum dots grown for lower-enegy photoluminescence. The energy scales for positive trion and biexciton emission, relative to the neutral exciton, are found to hold. A large fine structure splitting (100 μeV) is seen in the neutral exciton doublet. Colored bars indicate peak area. (b) Increase in integrate PL counts for the spectral features identified in (a). The bi-exciton feature continues to increase as the single exciton features are saturated. Additionally, the high-energy side of the neutral exciton doublet (just above 1.119 eV) saturates with much lower integrated counts than the lower energy side.

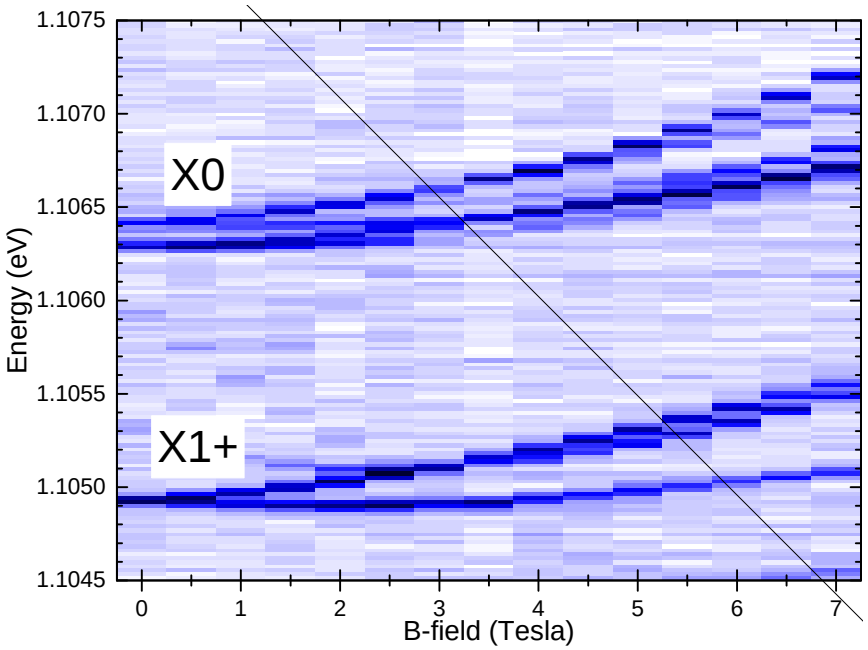

Figure 4.6: Contour plot of photoluminescence spectra in increasing magnetic field in the vertical **z** direction (Faraday configuration). Neutral exciton and positive trion features are identified at 0 T, and the magnetic field evolution is dominated by the quadratic, diamagnetic shift. Color scale: Darker blue indicates higher count rate; arbitrary scale.

is shown in Figure 4.6 for a single QD. This data is representative of a small (ten) sampling of QD magnetic field behavior. Although this is not the same dot as Figure 4.5, the neutral exciton and positive trion are easily identified at zero field. The most striking feature of the photoluminescence data is the quadratic component to the evolution- this is due to the polarizability of the InAs SAQD, and simply involves adding a quadratic term to our fitting above.

We first focus the analysis from the beginning of the chapter on the positive trion. Peak positions were extracted at each magnetic field, and plotted in Figure 4.7(a) , along with quadratic fit mainly to extract a polarizability of $\beta = 6\frac{\mu eV}{T^2}$. This was subtracted (along with a zero-field value of 1.1049eV) in Figure 4.7(b) in order to study the Zeeman interaction. Interestingly, the upper and lower branches have different slopes to their linearity which is not expected in the model above. This could be one of several things - in cases of sever asymmetry of the confinement potential, the dark exciton will hybridize with the bright exction, yet leave the energy structure without fine structure at zero magnetic field. In this case, we might expect the energy-increasing branch to have a bright-trion characteristic, and the energy-decreasing branch to have a dark-trion characteristic. Since we did not create this charged exciton through controlled (tunneling) mechanisms, the nature of the charging could have a significant impact on the magnetic field behavior. It is also clear that at the highest magnetic fields, 5 Tesla and above, the PL splits into more than just a doublet and we have neglected this from our analysis. This would be another part of the bright-trion PL branch. Ignoring the anomalous slopes of panel (b), Figure 4.7(c) is a plot of the energy difference between the peaks in (a). Fitting the slope of this line gives the g-factor for this trion to be 1.17.

The PL behavior of the neutral exciton in Figure 4.6 is shown in Figure 4.8, with the peak positions overlaid on the main data. What begins as a doublet in 0 Tesla,

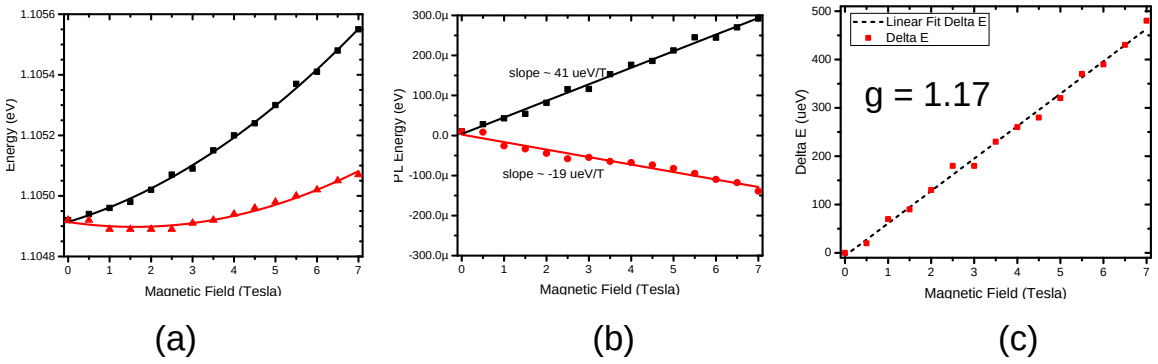

Figure 4.7: (a) Peak locations for X^{1+} shown previously. A quadratic fit gives a polarizability of $\beta = 6\frac{\mu eV}{T^2}$. (b) Subtracting the quadratic dependence allows for examination of the Zeeman Hamiltonian on the photoluminescence. The upper and lower Zeeman branches have different slopes, implying different angular momentum origins for each branch — if both sets of peaks were from the M=1 manifold, they would have the same slope. This suggests significant mixing between the M=1 and M=2 manifolds. (c) Energy difference in upper and lower branches. The g-factor of the observed PL is 1.17.

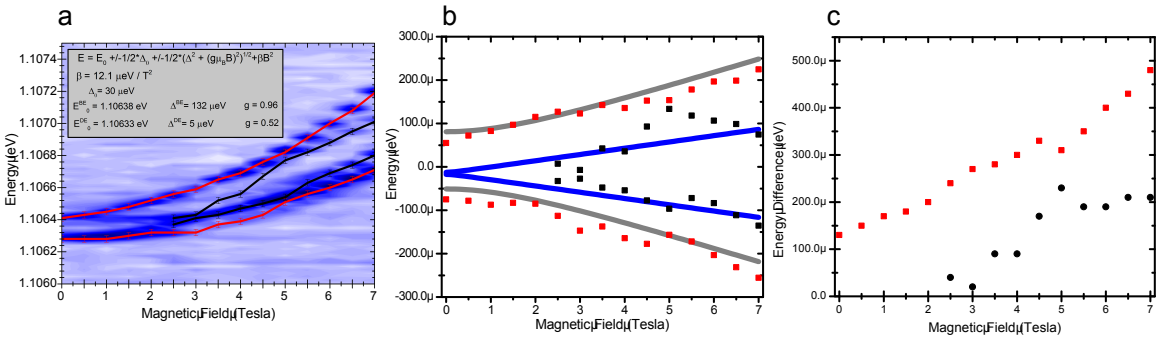

Figure 4.8: (a) Peak assignments for the observed spectra. Red is assigned to bright excitons, while black is assigned to the dark excitons. The shaded box contains the parameters used to fit the data. (b) The same data shown in (a) but with the quadratic diamagnetic shift subtracted, and the linear Zeeman splitting plotted according to the model discussed. (c) Energy difference between peaks in (a), used to assign peaks based on the linear character of the energy splitting.

around 3 Tesla, the doublet features each split so there are a total of four peaks. The quadratic dependence of the peaks makes peak identification difficult (which peaks split off from where), but looking at the energy differences in the peaks as shown in Figure 4.8(b), an estimate of peak assignments can be made. This is used in Figure 4.8(a) to show the outer-most branches as belonging to the bright (M=1) exciton, and the inner branches are attributed to PL from the dark excitons.The solid lines in Figure 4.8 are the Zeeman splittings calculated using Eqs. 5, with the parameters fit from Figure 4.8. While there is good agreement between the data and model at low fields, there appears to be further coupling between the bright and dark states around 6 Tesla, where the upper Zeeman branch of the dark states switches sign, and the lower Zeeman branch of the dark states also shifts in energy. Although different interpretations are possible, it is likely that past this magnetic field, the rotational symmetry destroyed completely such that there is an effective in-plane magnetic field, leading to behavior which significantly deviates from the above discussion. Note that the PL behavior in an in-plane magnetic field is well understood, but has not been discussed here. The large fine-structure splitting of the neutral exciton in the absence of a magnetic field also supports the idea that there is strong asymmetry in this system.

4.2.3 Towards Spin-Photon Interfaces

Lastly, we include a few measurements of polarization-resolved PL spectra at increasing magnetic fields, which is accomplished by adding a zero-order quarter wave plate ($\frac{\lambda}{4}$ at 1064 nm). At 0 Tesla, the spectra for both the positively charged and neutral excitons have no polarization dependence in the circular basis. For the positively charged exciton, this can be understood as the two circularly polarized transitions

being degenerate in energy. For the neutral exciton, this is a consequence of the re-normalized eigenstates having linear polarization selection rules - but was not confirmed with linearly-resolved polarization measurements. At 3.5 Tesla, we see the trion has formed a doublet with opposite polarizations, and the exciton doublet has achieved a reasonable degree of polarization in the circular basis. At 7 Tesla, the trion is about to form a quadruplet, while still showing a clear degree of circular polarization for all observed peaks. Meanwhile, the exciton has formed a quadruplet. The polarization structure of these 4 peaks is complex, with 3 showing clear preference for a circular basis, and the fourth having no polarization preference. We note that the input laser polarization was not characterized, thus could potentially be coupling to one polarization more than the other and confounding these measurements.

4.3 Resonant Excitation for Spin-Photon Interface

The main purpose of non-resonant excitation is to identify the energy range of exciton features. Coherent control using SAQD as either a qubit or mediator for photonic qubits relies on resonant driving. Previous experiments have relied on heterodyne techniques to distinguish the excitation light from the scattered light in the forward-scattered (differential transmission) and backwards-scattered (differential reflection) directions. However, the signal-to-noise level of this approach limits the feasibility of experiments that can be performed practically. Furthermore, the heterodyne approaches are based on changes in absorption of the driving laser, thus there is no direct detection of the resonantly scattered photons. Direct detection of the resonance fluorescence offers the possibly to observe time-resolved quantum jumps [82], as well as a better signal-to-noise background. The main obstacle for direct detection of resonance fluorescence is to separate the light scattered by the QD from the

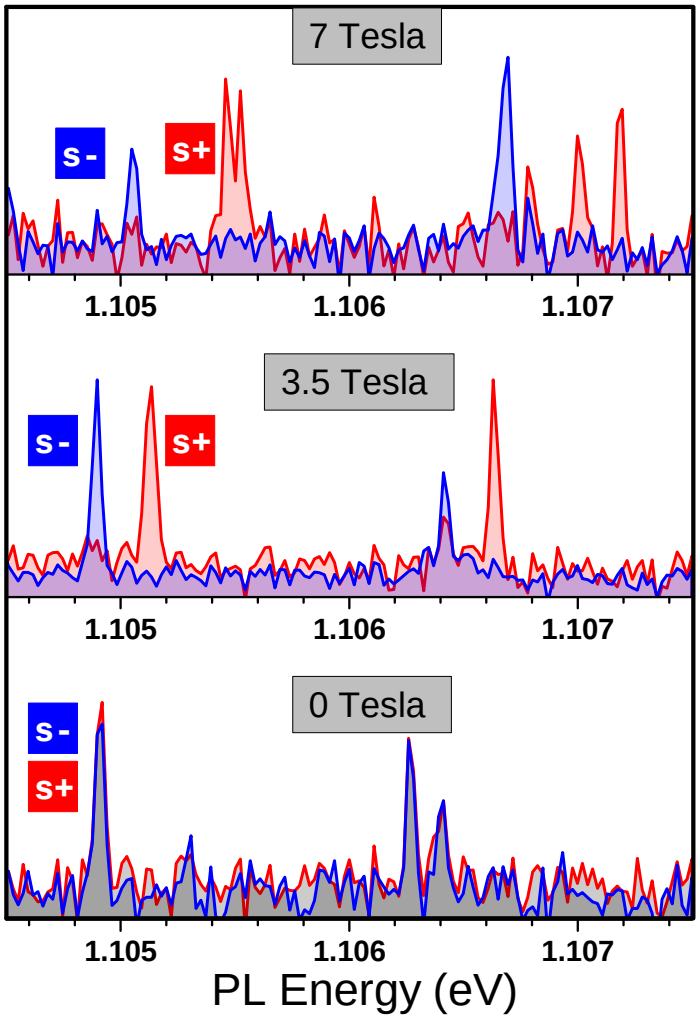

Figure 4.9: Evolution of the PL in the circular polarization basis. At 0 field, the PL is not polarized. As several peaks start to split off, the spectra become more circularly polarized. The neutral exciton features never become fully polarized, suggesting bright-dark exciton mixing.

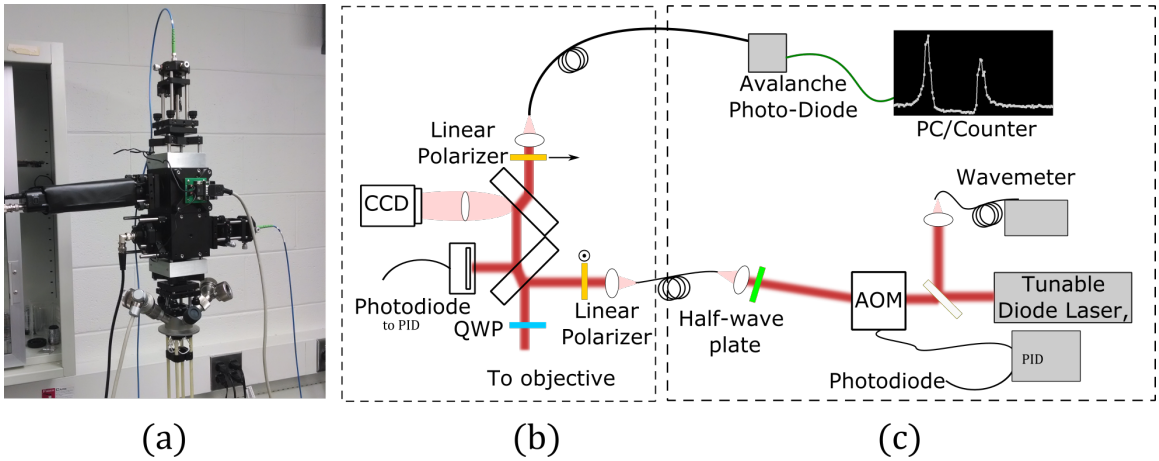

Figure 4.10: (a) Photograph of the fiber-based microscope head built for resonance fluorescence detection via polarization rejection. (b) Schematic of microscope components (c) Non-microscope components necessary to realize detection of resonance fluorescence, including tunable diode laser with feed-back stabilized intensity, wavemeter, and single photon avalanche detector.

excitation light. We have implemented a polarization-based dark field concept in the confocal microscope, as illustrated in Figure 4.10, and used it to study the resonance fluorescence of InAs QDs emitting in the 940-960 nm spectral range. A variation on this design [17] is to replace the plate beamsplitters with polarizing beamsplitter cubes. While this may offer higher background extinction, the disadvantage is in the cost of the optics (particularly the polarizing beamsplitter cubes) and increased dependence on driving wavelength.

4.3.1 Dark-field Microscope

The dark- field concept is as follows. Linear polarizers in separate excitation and collection channels are mounted such that light passing through the excitation path will be blocked at the collection path. This simple concept is difficult to implement in practice - in part because in order to see just the scattered light from the SAQD, an extinction ratio greater than 10^6 is required to eliminate most of the incident

laser drive. In this fiber-based confocal microscope design, paired with the attoDry 1000 at the vacuum port, we utilized cage-cube optomechanical mounts for compactness. All optics and optomechanics (with the exception of piezo-rotary positioners) were purchased off-the-shelf from Thorlabs. The design kept with glass surfaces for reflecting and beam-splitting, as the polarization state throughout the microscope needed careful compensation for extra phases in out-of-plane components acquired on reflection. Metal surfaces tend to convert a linearly polarized beam into a slightly elliptical beam which is hard to recover from. Additionally, the glass beamsplitter was chosen to be optically thick such that any ghost reflections could be blocked with an iris. The polarizers were nano-particle film linear polarizers (LP-NIR-050) with a quoted ER above 5 x 10^6. The quarter waveplate (WPQ05M-980) was used to correct elliptical polarization aberrations in the reflected light path. With this design, an extinction ration of $3x10^6$ was measured from fiber input to APD output. This allowed for resonant photoluminescence excitation spectra, wherein the laser was kept at a fixed frequency and the QD energy was scanned (via the DC stark shift discussed in earlier chapters) through the laser. Note that the sample/laser detuning can also be controlled by the laser frequency, however, the polarization extinction is strongly frequency dependent and will increase the background counts of the laser onto the APD by a factor of 10 when tuning the laser over 1 GHz.

4.3.2 Resonance Fluorescence Detection

Figure 4.11 (a) shows resonantly scattered light from a neutral exciton, which is fit to a double- Lorentzian curve. At zero field, fine-structure of the neutral exciton transition is apparent with the higher energy transition split from the lower energy transition by $\approx 20\mu$eV, just below the resolution limit of the spectrometer ($\approx 25\mu$eV

). There is a small amount of asymmetry in-between the two neutral exciton peaks, which is possibly due to polarization-based interference.

Figure 4.11(b) shows resonance fluorescence from X^{1-} in the same QD in zero magnetic field. Notice that fine structure is not apparent until a small DC magnetic field is applied (0.8 T along the growth direction), wherein two peaks emerge in the spectra as seen in Figure 4.11(c). We also studied the saturation behavior of X^{1-} with no magnetic field. Figure 4.12 shows the laser background (black) and fluorescence signal on resonance (red) for X^{1-} see in Figure 4.11(b). Since we are only addressing a single transition, the system behaves as a two-level system, and the saturation behavior will be slightly different than that seen for non-resonant excitation. A fit to the equation

$$I = I_{sat}\frac{P}{P+1} \tag{4.6}$$

shows that the saturation power is approximately 150 nW — that is, at 150 nW, the measured count rate is approximately 1/2 of saturation count rate (45 kHz here). Comparing the above saturation fit to the excited state population ($P_{a,ss}$) calculated from the optical Bloch equations [83], (where $\Omega = |\mu_{12}|\varepsilon/\hbar$ is the Rabi frequency, $\gamma = \gamma_1 + \gamma_2$ is the total decoherence rate, γ_1 is the radiative rate, γ_2 is the pure dephasing rate).

$$P_{a,ss} = \frac{1}{2}\frac{\Omega^2/(\gamma\gamma_1)}{1+\Omega^2/(\gamma\gamma_1)} \tag{4.7}$$

we can identify $S = \Omega^2/(\gamma\gamma_1)$ as the saturation parameter. For the quantum dot above, the fit parameters give the saturation to occur at a laser power of just 133 nW, or an intensity of 1.33 x 10^4 mW / cm^2. In comparison to atomic vapors, the QD needs a higher intensity to reach saturation, but since we are in a diffraction-limited environment (instead of a mm-wide beam), this is relatively straightforward to achieve with modest diode lasers. [84]

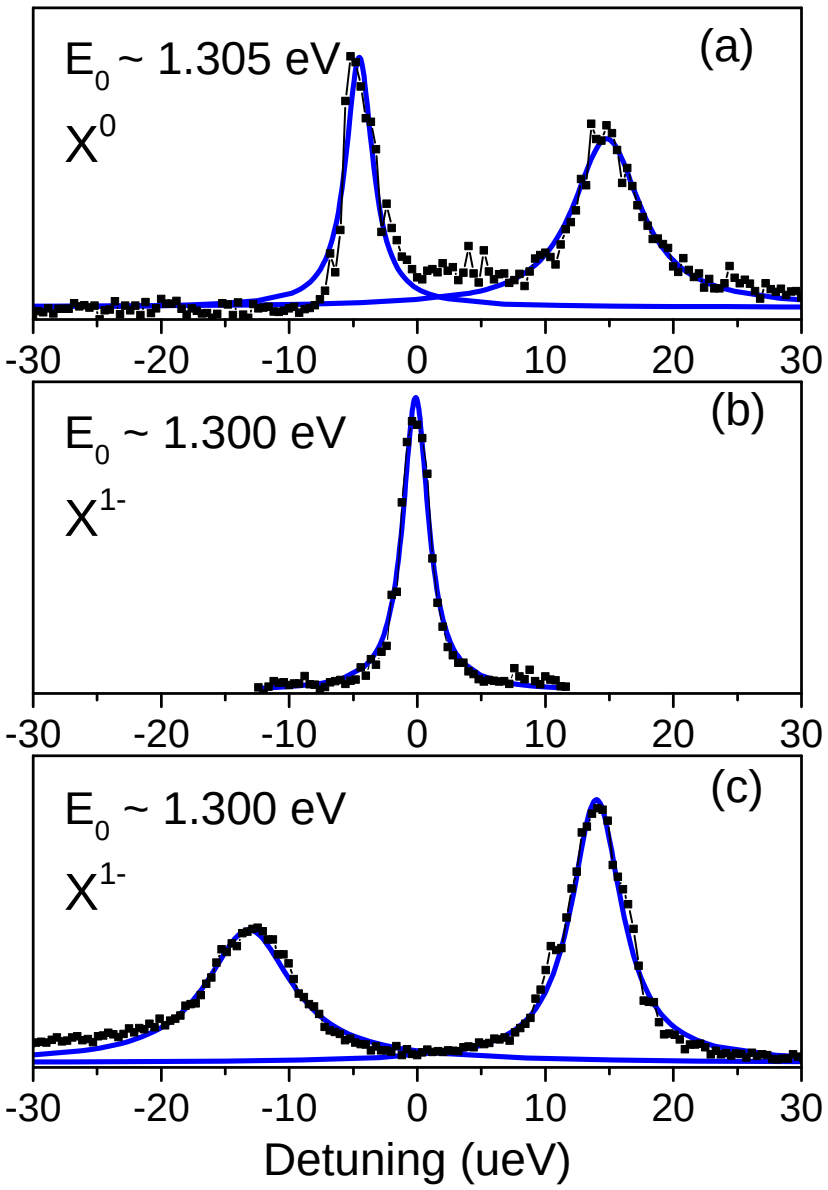

Figure 4.11: Resonant light scattering probes the fine structure of a neutral exciton and negatively charged trion in a single quantum dot. The laser was kept at a fixed frequency while the quantum dot energy was swept through the laser using the Stark Shift and an external gate voltage. Lorentzian lineshapes are used to fit the data. Fine structure of the neutral exciton is evident without a magnetic field (top), while X^{1-} has no fine structure (middle). A small magnetic field splits X^{1-} according to the Zeeman effect.

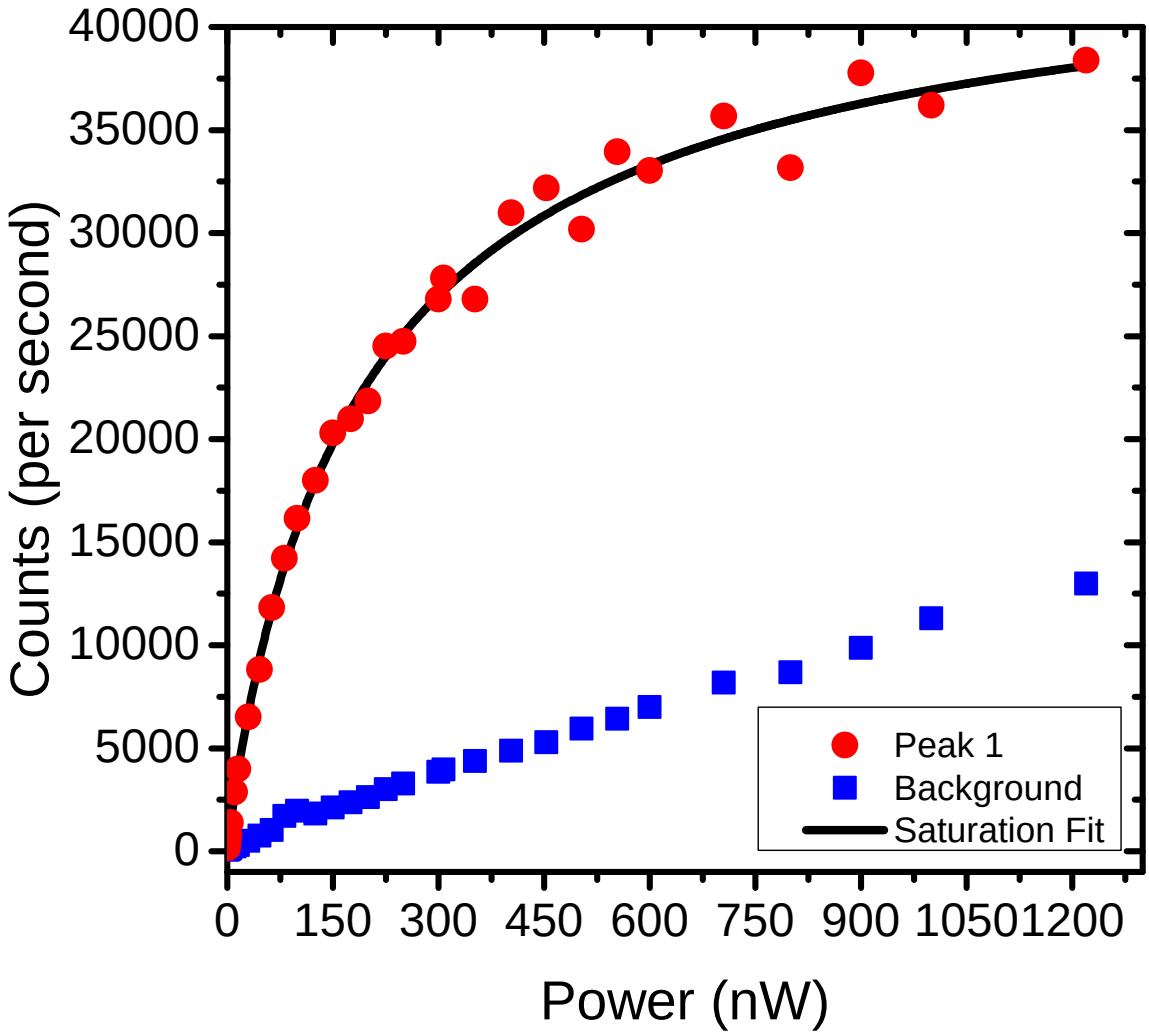

Figure 4.12: Saturation of resonance fluorescence from X^{1-}can be seen by increasing the resonant laser power. The saturation count rate is 45 kcts/sec, and the saturation power is 200 nW.

Chapter 5

Defects in Emergent Materials: WSe_2

Groundbreaking work on the electronic and optical properties of monolayer graphene flakes [25–29, 35, 41] has spurred intense interest in finding other atomically thin material systems with similarly appealing physical properties. As we saw in Chapter 2, graphene is a semi-metal, and much of the scientific excitement is derived from finding mono-layer materials which span the realm of conducting to insulating materials, including superconductors and semiconductors [85]. A number of layered materials comprised of a transition metal (tungsten (W), molybdenum (Mo)) and two chalcogenides (selenide (Se), sulfur (S)) have been shown to exhibit emergent photoluminescence when reduced to a single material layer [86–88]. This is due to the quantum well-like nature of exciton confinement in the single layer. These transition-metal dichalcogenides (or, TMDC) materials are direct-gap semiconductors when thinned to monolayer, and produced by exfoliation techniques similar to graphene. A new class of devices has been realized where these materials — in conjunction with graphene and insulating single layers such as hexagonal boron nitride — are first thinned to

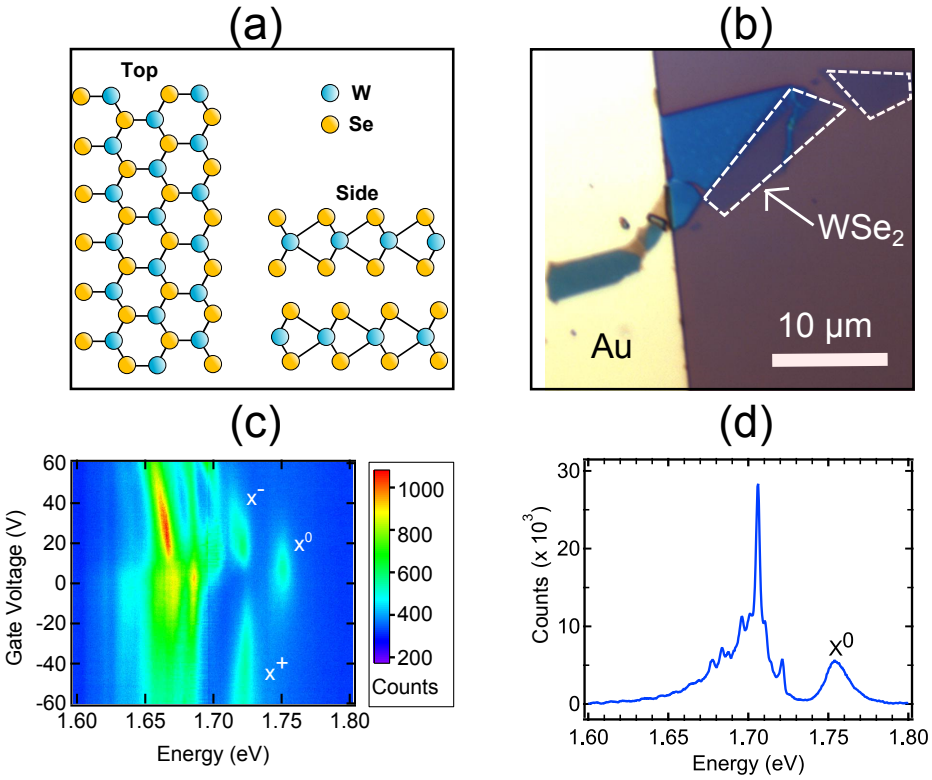

Figure 5.1: (a) Ball-and-stick model of single layer tungsten diselenide (WSe_2) (b) Optical micrograph of multilayered WSe_2 flake attached to gold electrode (c) PL spectra of single layer WSe_2, showing characteristic 2D neutral exciton emission

mono-layer, then stacked upon one another using transfer techniques discussed in Chapter 2 [31]. The term 'van der Waals heterostructure' was coined to refer to these devices, as the layers bind to each other due to the strong van der Waals forces. The design freedom promoted by such production methods will be a driving force for future quantum technologies [87, 89–97].

From this perspective, the potential for defects to further localize excitons in TMDC materials could enable novel sources of quantum light as well as provide a physical implementation of a stationary qubit. In previous chapters, we have explored one of the longstanding champions of optically active defects — namely, the InAs self-assembled QD – thus, it is natural to ask whether TMDCs can host their

own versions of an artificial atoms. In this chapter, we explore the quantum optical properties of light emission from as-yet unidentified defect states (which we preemptively call quantum dots) in mono-layer WSe_2. The work in this chapter is based on the publication found in Reference [98]. Note that during the preparation of the original manuscript, we became aware of three similar studies. [99–101]

Unlike graphene, the crystal structure of TMDC materials is composed of three atomic layers, shown in Figure 5.1(a). Figure 5.1(b) shows a micrograph of the exfoliated WSe_2 device - a silicon wafer with 270 nm of SiO_2, on top of which a gold electrodes are patterned, and finally exfoliated layers of the material tungsten diselenide (WSe_2) placed on top of the gold contact. A copper strip is placed on the backside of the wafer, enabling a gate voltage to be applied to the flake. Regions of darker color correspond to more layers, with the lightest contrast being a single layer. This is also identified by the white dashed boundary. The device is loaded into a magneto-optical cryostat on x-y-z positioners for sample positioning and kept at a temperature of 4 K. Light emitted from the material, following optical excitation at 532 nm, is directed to a spectrometer that sends the dispersed light to a charge-coupled device (CCD) array for spectral measurements or through an exit slit to filter the emission prior to measuring the second order intensity auto-correlation.

Figure 5.1(c) shows low-temperature photoluminescence spectra from the single-layer region of the flake against an applied voltage. The spectrum is dominated by 'bulk' excitons which exist in the plane of the single flake [102, 103]. The neutral exciton peak is seen at a bias of 0 V, while the (positive) negative trion appears at (negative) positive gate voltage bias. The spectral locations and voltage dependence of these bulk excitons are a benchmark for knowing that we are interrogating a monolayer of WSe_2. More interesting spectra is observed when the sample is positioned at an interface between the WSe_2 monolayer and the attached multilayer WSe_2. In

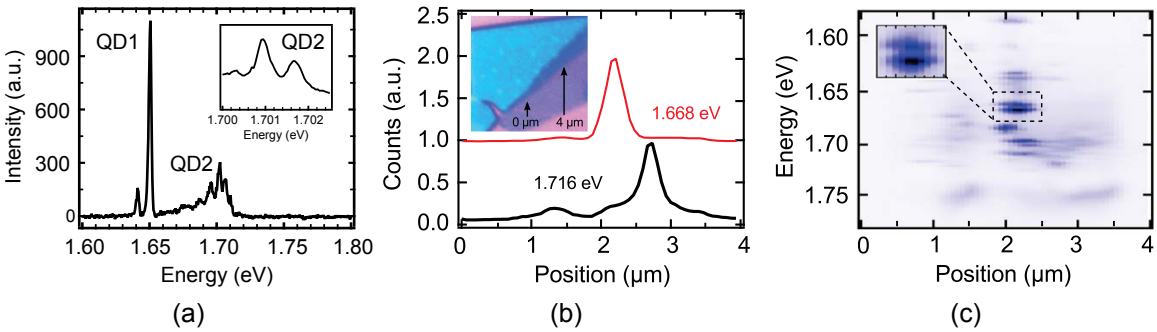

Figure 5.2: (a) Narrow emission lines identified as QD1 (1.65 eV) and QD2 (1.70 eV) in the photoluminescence spectrum around the interface of the single- and multilayer regions of the flake. (b) Spatially resolved PL from two quantum dots, showing diffraction-limited confinement of the PL. Inset: Optical micrograph of the flake with arrows indicating start and end points of spatial sampling (c) One-dimensional hyperspectral image of WSe_2 QD emission exhibiting spatial localization, using the same path shown in (b). Inset: Zoom-in of of the black dashed box in the main image showing co-localization of a doublet feature.

this configuration the spectrum in 5.1(d) is measured. In stark contrast to Figure 5.1, the emission now consists of a number of narrow emission lines that are bright when compared to the extended two-dimensional WSe_2 excitons even at an excitation power that is 20 times less than the excitation power used for spectra in5.1(c). For clarity, in the remainder of this work we will refer to these bright lines as QDs, thus labeling QD1 (1.65 eV) and QD2 (1.70 eV) - their PL are seen in Figure 5.2(a).

5.1 Defect Characterization

We first investigate the spatial extent of these features along the WSe_2 single layer/multilayer boundary identified in the inset of Figure 5.2(c). Linecuts from the hyperspectra, Figure 5.2(c), show the lateral extent of the confinement to be within the point-spread-function of the confocal microscope (NA=0.8), indicating strong confinement of excitons. This is typical of many of the emission lines observed, as shown in the contour plot of Figure 5.2(b)

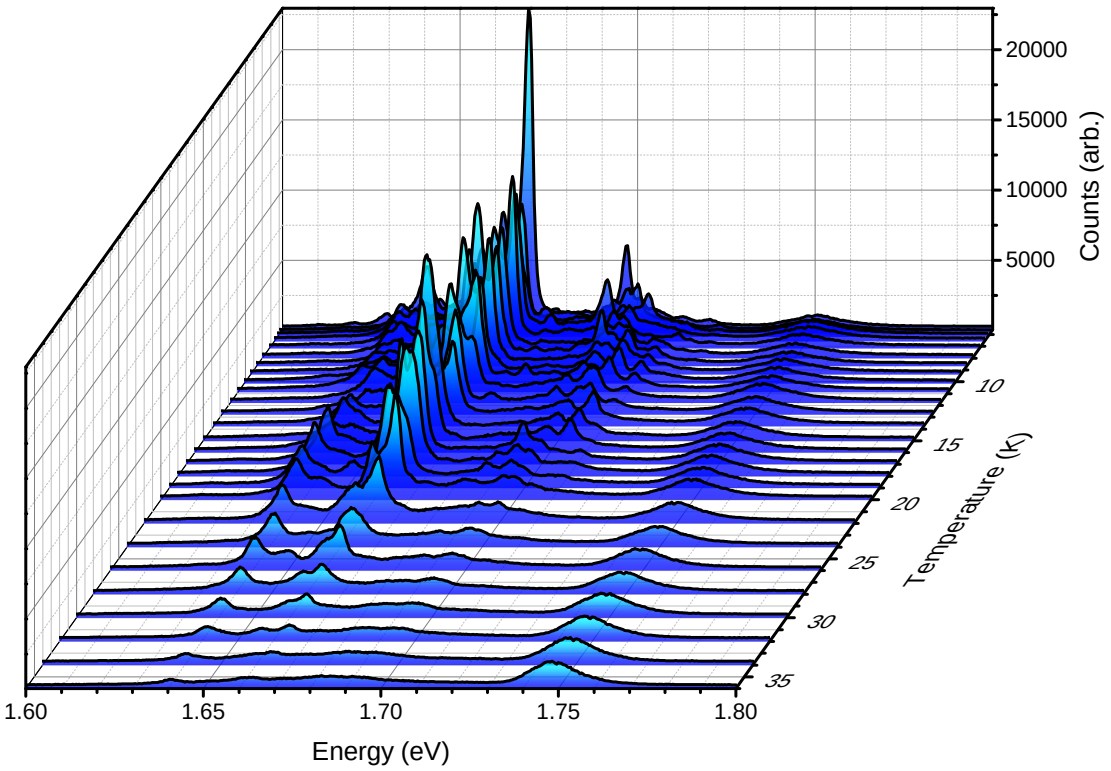

Figure 5.3: Temperature dependence of multiple QD emission lines showing a decrease in PL intensity with increasing temperature. Defect-related luminescence disappears around 30 Kelvin.

Temperature dependent photoluminescence is recorded for a number of WSe_2 QDs, shown in Figure 5.3. At low temperatures, we see light emission from both defect states (1.65 eV, 1.67 eV, 1.70 eV) as well as the bulk exciton (1.75 eV). As expected for defects [24], above a certain temperature, in this case $\sim$ 35K, the light emission is nearly suppressed and the bulk exciton luminescence has become the most prominent spectral feature. We further find that luminescence from the defects is restored when the temperature is lowered back to 4K, and is robust against temperature cycling.

Additionally, the quantum nature of the light emission is seen in the saturation of photon count-rates measured in the PL spectrum shown in Figure 5.2 (b) . More directly, the photon statistics are measured for several WSe_2 QDs, and found to display

the anti-bunching statistics consistent with single photon emission. A Hanbury-Brown Twiss interferometer is used to measure the second-order correlation function, $g^2(\tau)$. The principle underlying the interferometer is as follows: an optical signal enters through the beamsplitter, and the intensity is split equally into two paths (reflected and transmitted). Two detectors, one in each arm of the interferometer, are used to record the arrival times of photons in each arm. The time between photon arrivals, or delay time $\tau = t_r - t_l$ is recorded. A histogram reveals the number of occurrences for the photon in the lower arm to arrive at the delay time τ relative to the lower arm. Thus, the histogram directly reflects the intensity-intensity correlation function

$$g(\tau) = \frac{E^\dagger(t_r)E^\dagger(t_l)E(t_r)E(t_l)}{\langle|E(t_r)|^2\rangle\langle|E(t_l)|^2\rangle} = \frac{\langle a^\dagger(0)a^\dagger(\tau)a(\tau)a(0)\rangle}{\langle a^\dagger a\rangle^2}$$

where E is the electric field of a classical light source, and a ($a^\dagger$) is the photon lowering (raising) operator for a quantum light source. For a time delay $\tau = 0$, a single-photon source will have a correlation value of $g^2(0) = 0$, since there can be no simultaneous photon detect events with a single photon - a phenomena known as 'anti-bunching'. We incorporated such an interferometer at the output slits of the spectrometer used to measure PL spectra. In this way, we were able to filter out and record statistics from just a single narrow spectral feature. A schematic of this is shown in Figure 5.4.

Figure 5.5 (b) shows the second-order correlation measurement of the WSe_2 QD peak at 1.68 eV, with a pronounced anti-bunching dip at $\tau = 0$. Fitting the zero-time delay portion to $1-e^{-t/\tau}$ gives a lifetime τ =1.8 ns, and this lifetime ranges from 0.5-2 ns depending on the spectral feature studied. The lifetime for bulk excitons in single-layer WSe_2 is only 30ps [104]. Thus, increased lifetime of these narrow features over their bulk counterparts can be attributed to full three-dimensional confinement [14].

One of the main challenges when working with the PL spectra of these defect

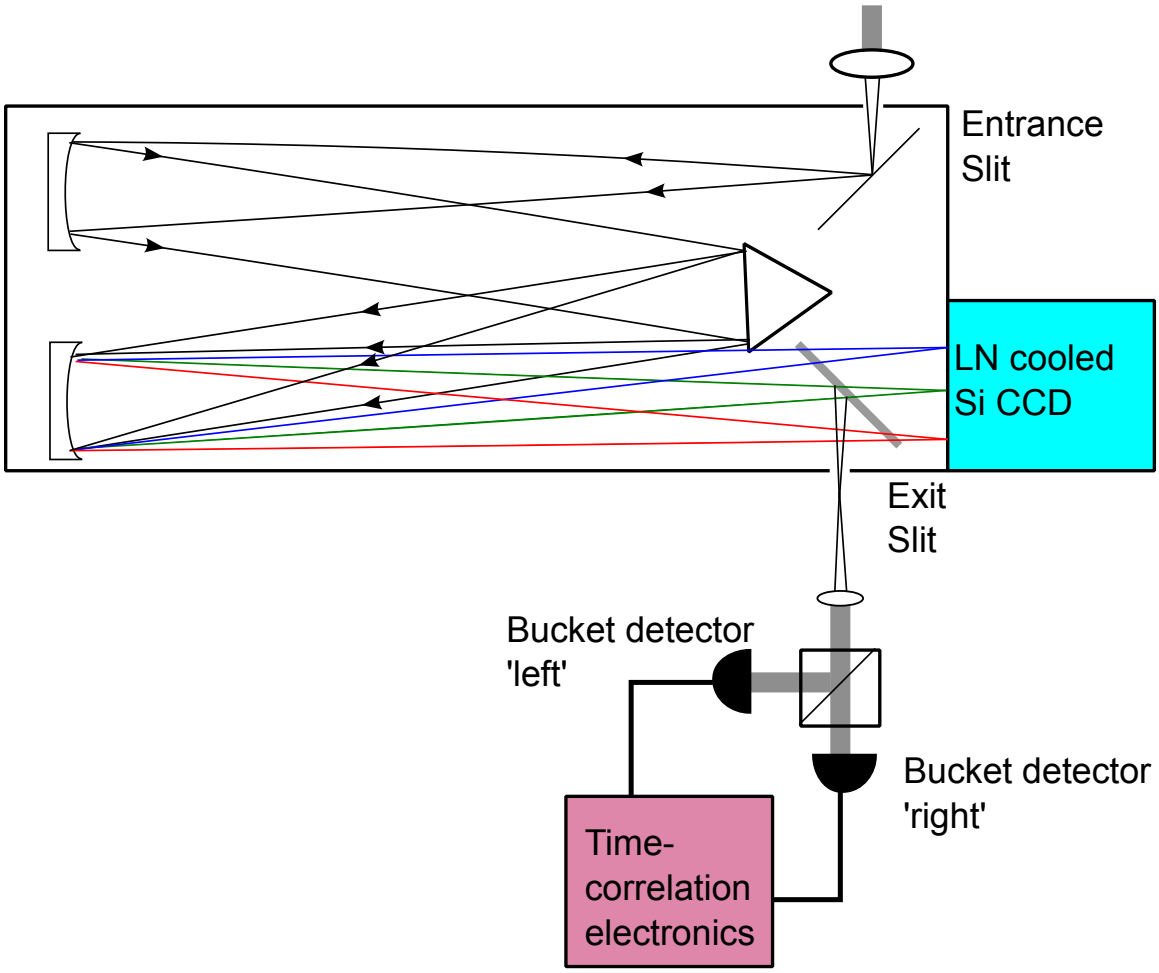

Figure 5.4: Spectrometer-monochromator ray diagram to filter single emission lines in the WSe_2 defect spectra. The movable grating (center turret) allows the monochromator to act as a tunable spectral filter, enabling sequential measurements of emission at different energies. The flip-mirror in the latter portion of the spectrometer sends light to the exit slit instead of the CCD camera, where it is re-collimated and sent to two bucket detectors via an intensity-splitting beamsplitter.

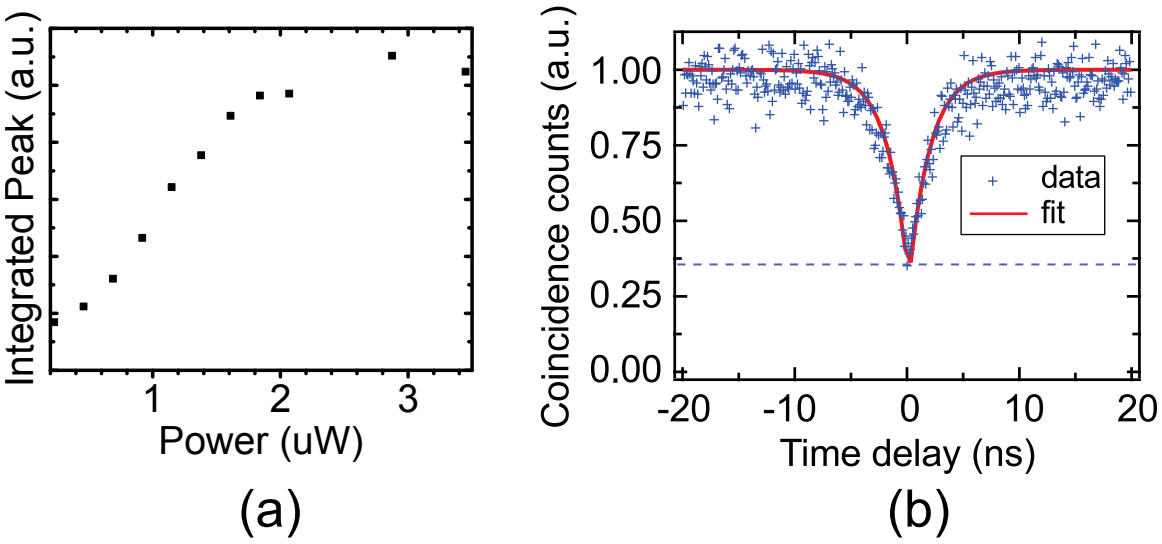

Figure 5.5: (a) Power saturation behavior of QD 2 (b)Intensity auto-correlation measured at 1.68 eV (QD3, spectra not shown). The horizontal dashed line corresponds to the zero-delay value of 0.36, indicative of quantum light emission statistics

states is the large spectral wandering of the observed emission lines. Figure 5.6(a) shows a contour plot time-trace of PL spectra recorded at a fixed position on the flake, and it is clear the peak wanders significantly. Figure 5.6(b) gives a quantitative feel for this, as the upper panel is a spectra acquired for 1 sec., while the lower panel is an average over all 300 spectra (acquired at 1 sec. intervals). The lineshape deviates from the data slightly, but the FWHM is clearly increased on the longer timescale, creating an obvious source of inhomogeneous broadening.

5.2 Gate-Voltage Controlled Emission

Bulk WSe_2 is known to support gate-voltage controlled emission [95], as seen in Figure 5.1(c), thus it is natural to suspect that a static electric field can modify the spectra and/or emission properties of the defect-related QDs. While in InAs QDs, the gate voltage produces a Stark Shift due to the confining nature of the band structure, this

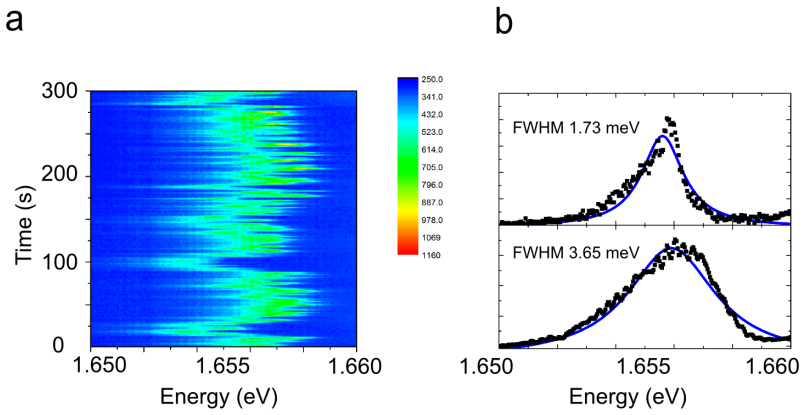

Figure 5.6: (a) Photoluminescence spectra of a WSe_2 QD showing spectral wandering over 3 minutes. (b) A linecut for a single spectra (top) and for the PL spectra integrated over 300 sec. The FWHM is significantly broadened by the spectral wandering.

is not likely to be the case for WSe_2 QDs.

We proceed by measuring spectra at a range of gate voltages, and observe two main QD features, labeled 'X' and 'Y' in Figure 5.7 (a). Figure 5.7 (b) and (c) shows linecuts of these spectrally distinct QDs, whose photoluminescence rates (counts acquired) are modified by the application of a gate voltage. Around 20V, the counts from Peak X have disappeared fully, while the count rate from Peak Y reaches its maximum value of 12 kHz. Linecuts at constant voltage are presented in Figure 5.7 (d)-(f) for clarity, and normalized the count rate in (e). It is likely the case that the defect stability is modified by changes to the local potential energy landscape - this could also relate to the observed spectral wandering of the features discussed in the previous section. Additionally, g^2 measurements (inset of Figure 5.7 (e) and (f)) of peak Y (X) at 0 V (-50V) indicate that the defect-based exciton lifetime can be modulated by the application of an electric field. The g^2 measurement in (e) features a very narrow anti-bunching peak, while the g^2 curve in (f) is more broad. Whether the decay time of an isolated WSe_2 QD can be deterministically controlled by a gate voltage is left for future experimentation.

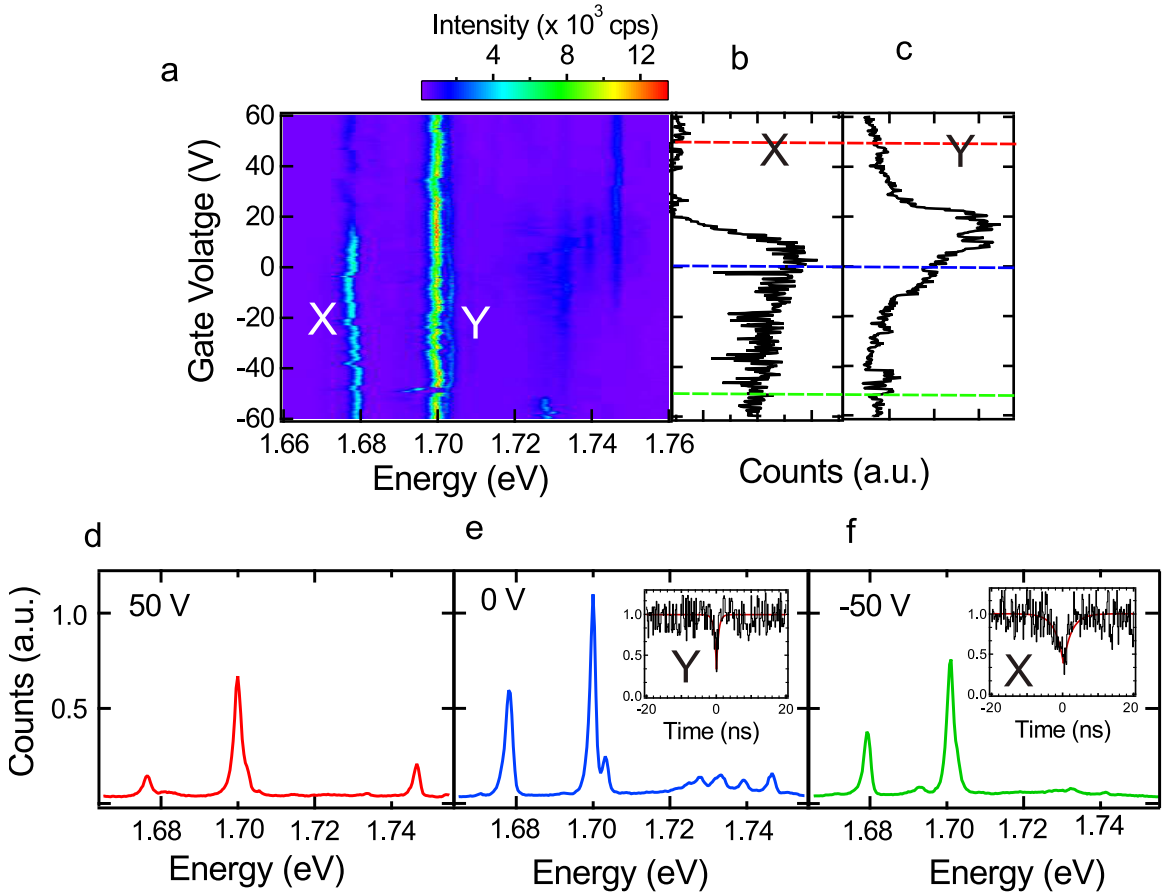

Figure 5.7: (a)Two-dimensional plot of emission energy vs gate voltage. Modulation of peaks labeled X and Y is most pronounced. (b)-(c) Integration of peaks X and Y shows a definite modulation. (d)-(e) Line-cuts at gate voltages indicated in (b) and (c). g2 measurements show a possible modulation of QD lifetime.

5.3 Magnetic Field Behavior

Finally, the magnetic field behavior of the WSe_2 QDs are studied. A QD exhibiting a doublet around 1.688 eV was chosen as a finite zero-field splitting would relate well to the model discussed in Chapter 4 — where 0-field fine structure was indicative of neutral exciton angular momentum selection rules. The PL spectra vs. magnetic field are shown in Figure 5.8(a), with the two peaks of interest lying within the shaded region. Spectral wandering is manifest again in the absolute positions of the peaks with increasing magnetic field, shown in Figure 5.8(b). However, the wandering of the doublet peaks is correlated, therefore we use the energy difference in the peaks to fit the magnetic field dependence. A hyperbolic dispersion (Figure 5.8(c) fits nicely to the observed splitting of the peaks [81]. This fit gives the zero-field splitting to be approximately 700 μeV, and the g-factor of this quantum dot to be 9.8, which is an order of magnitude large than what is observed in InAs QDs [81, 82].

5.4 Conclusions

In this chapter, we presented one of the first demonstrations of optically active quantum dot-like defects in atomically thin semiconductors. The localized emitters serve as a source of single photons that are correlated with the internal spin structure, much like NV centers in diamond briefly discussed in Chapter 3, and the InAs QD studies presented in Chapter 4. We envisage a number of future directions enabled by this demonstration. WSe_2 , along with graphene, is part of the growing family of 2-dimensional materials generated by exfoliation. Van der Waals heterostructures - made by Lego-like stacking of these materials- will provide a novel platform for the natural extension of the demonstrated gate voltage control and make WSe_2 electrically

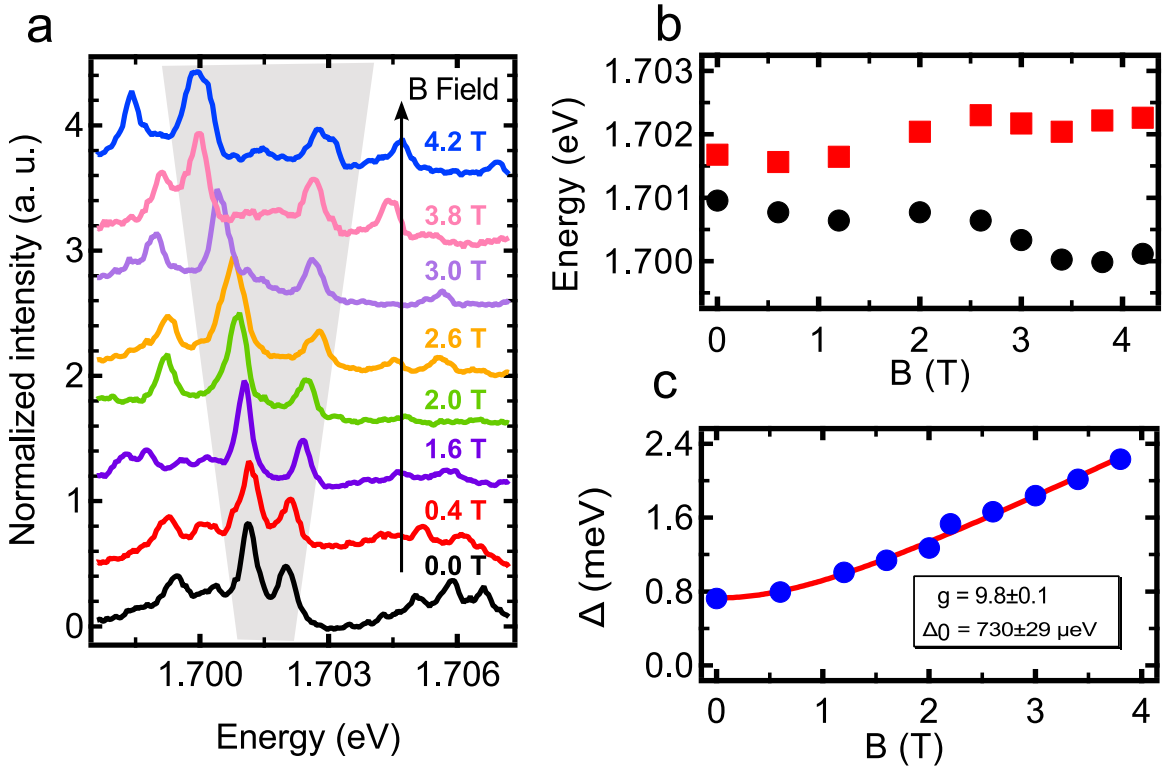

Figure 5.8: (a) Spectra at increasing magnetic field. The gray box indicates correlated peaks. (b)Integration of peaks from (a), exhibiting correlated wandering and definite Zeeman shift. (c) Zeeman energy shift as a function of magnetic field. The g-factor is an order of magnitude larger than InAs QDs, which is promising for spin applications.

controlled quantum dots a viable physical implementation for quantum information processing. In the context of spin physics, we have not covered the polarization of these features. As we saw with InAs strain-based QDs, the origin of exciton confinement can be imprinted in the polarization of different spectral features of the QD.

Chapter 6

Future Directions

This thesis has explored light emission from zero-dimensional structures, and has established a link between zero- and two- dimensional physics in a number of ways. We explored light emission from self-assembled quantum dots (SADQ), as well as establishing single photon emission in defects within the two-dimensional material WSe_2.

We established how to interpret the SAQD spectrum with respect to the number of charge carriers participating in light recombination. We demonstrated the use of a vertical electric field as a knob to tune the emission energy, as well as ground-state charge configuration. As part of this application, we provided the first demonstration of SAQD electrical control via single layer graphene. The performance of the graphene device was bench-marked against a traditional device. It was found that there is no difference in electrical control, and a modest photonic increase is attributed to the transparency of the graphene film. Further analysis of this device could incorporate the difference in s- and p- Fresnel coefficients to determine how the polarization of the input and output light is affect at the GaAs - metal - air interface, as the polarization degree of freedom is important for quantum information applications.

In Chapter 3, we paved a path for the use of SAQDs as a sensor array, where the local electrostatic potential can be mapped. This type of sensing mechanism could be especially useful for condensed matter investigations into two-dimensional physics, and the next set of devices could easily incorporate the unique electron physics in a graphene film device.

The spin physics of SAQDs was explored in two way. We reported on the spin physics of InAs QDs designed for near-telecom wavelength emission. The present measurements could be extended by adding an electric field for deterministic charge control, which would provide a more complete picture of the magnetic field evolution seen here. Additionally, we looked at key issues in demonstrating resonance fluorescence from a SAQD by building a polarization-based dark field microscope. The present microscope design provided in Chapter 4 would be especially useful for optically detected magnetic resonance studies in SAQD, however, an optimized photonic environment is necessary to achieve a reasonable photon count rate. Reasonable choices for such photonic improvements include a distributed Bragg cavity, photonic crystal cavity, or numerical-aperture increasing lens. With a few improvements, such as demonstrating crossed-polarization along multiple input polarizations, questions in quantum interference and coherence could be addressed, similar to reports see in other QD investigations (see [105]).

Lastly, this thesis presented one of the first demonstrations of optically active quantum dot-like defects in atomically thin semiconductors. The localized emitters serve as a source of single photons that are correlated with the internal spin structure, much like NV centers in diamond briefly discussed in Chapter 3, and the InAs QD studies presented in Chapter 4. We envisage a number of future directions enabled by this demonstration, including:

1. Incorporating the emitters into a charge-tunable heterostructure

2. Understanding the origin of spectral wandering

3. Studying the polarization dependence of the QD features

Bibliography

[1] R. J. Warburton, C. Schaflein, D. Haft, F. Bickel, A. Lorke, K. Karrai, J. M. Garcia, W. Schoenfeld, and P. M. Petroff, "Optical emission from a charge-tunable quantum ring," Nature **405**, 926–9 (2000).

[2] R. J. Warburton, B. Miller, C. Dürr, C. Bödefeld, K. Karrai, J. Kotthaus, G. Medeiros-Ribeiro, P. Petroff, and S. Huant, "Coulomb interactions in small charge-tunable quantum dots: A simple model," Physical Review B **58**, 16221 (1998).

[3] M. Ediger, P. A. Dalgarno, J. M. Smith, B. D. Gerardot, R. J. Warburton, K. Karrai, and P. M. Petroff, "Controlled generation of neutral, negatively-charged and positively-charged excitons in the same single quantum dot," Applied Physics Letters **86**, 211909 (2005).

[4] P. Dalgarno, J. M. Smith, J. McFarlane, B. D. Gerardot, K. Karrai, A. Badolato, P. M. Petroff, and R. J. Warburton, "Coulomb interactions in single charged self-assembled quantum dots: Radiative lifetime and recombination energy," Physical Review B **77**, 245311 (2008).

[5] E. Dekel, D. Regelman, D. Gershoni, E. Ehrenfreund, W. Schoenfeld, and P. Petroff, "Cascade evolution and radiative recombination of quantum dot multiexcitons studied by time-resolved spectroscopy," Physical Review B **62**, 11038–11045 (2000).

[6] A. Högele, S. Seidl, M. Kroner, K. Karrai, R. J. Warburton, B. D. Gerardot, and P. M. Petroff, "Voltage-controlled optics of a quantum dot," Physical Review Letters **93**, 217401 (2004).

[7] J. Dreiser, M. Atatüre, C. Galland, T. Müller, A. Badolato, and A. Imamoğlu, "Optical investigations of quantum dot spin dynamics as a function of external electric and magnetic fields," Physical Review B **77**, 075317 (2008).

[8] A. S. Bracker, E. A. Stinaff, D. Gammon, M. E. Ware, J. G. Tischler, A. Shabaev, A. L. Efros, D. Park, D. Gershoni, V. L. Korenev, and I. A. Merkulov, "Optical pumping of the electronic and nuclear spin of single charge-tunable quantum dots," Physical Review Letters **94**, 047402 (2005).

[9] X. Xu, B. B. Sun, P. R. Berman, D. G. Steel, A. S. Bracker, D. Gammon, and L. Sham, "Coherent optical spectroscopy of a strongly driven quantum dot," Science **317**, 929 (2007).

[10] M. Kroner, K. M. Weiss, B. Biedermann, S. Seidl, S. Manus, A. W. Holleitner, A. Badolato, P. M. Petroff, B. D. Gerardot, R. J. Warburton, and K. Karrai, "Optical detection of single-electron spin resonance in a quantum dot," Physical Review Letters **100**, 156803 (2008).

[11] J. McFarlane, P. A. Dalgarno, B. D. Gerardot, R. H. Hadfield, R. J. Warburton, K. Karrai, A. Badolato, and P. M. Petroff, "Gigahertz bandwidth electrical control over a dark exciton-based memory bit in a single quantum dot," Applied Physics Letters **94**, 093113 (2009).

[12] M. Atatüre, J. Dreiser, A. Badolato, A. Högele, K. Karrai, and A. Imamoğlu, "Quantum-dot spin-state preparation with near-unity fidelity," Science **312**, 551–553 (2006).

[13] A. N.Vamivakas, Y. Zhao, C.-Y. Lu, and M. Atatüre, "Spin-resolved quantum-dot resonance fluorescence," Nature Physics **5**, 198–202 (2009).

[14] A. N. Vamivakas and M. Atatüre, "Photons and (artificial) atoms: An overview of optical spectroscopy techniques on quantum dots," Contemporary Physics **51**, 17–36 (2010).

[15] S. G. Carter, T. M. Sweeney, M. Kim, C. S. Kim, D. Solenov, S. E. Economou, T. L. Reinecke, L. Yang, A. S. Bracker, and D. Gammon, "Quantum control of a spin qubit coupled to a photonic crystal cavity," Nature Photonics **7**, 329–334 (2013).

[16] A. N. Vamivakas, Y. Zhao, S. Fält, A. Badolato, J. M. Taylor, and M. Atatüre, "Nanoscale optical electrometer," Physical Review Letters **107**, 166802 (2011).

[17] A. V. Kuhlmann, J. Houel, A. Ludwig, L. Greuter, D. Reuter, A. D. Wieck, M. Poggio, and R. J. Warburton, "Charge noise and spin noise in a semiconductor quantum device," Nature Physics **9**, 570–575 (2013).

[18] Z. Yuan, B. E. Kardynal, R. M. Stevenson, A. J. Shields, C. J. Lobo, K. Cooper, N. S. Beattie, D. A. Ritchie, and M. Pepper, "Electrically driven single-photon source," Science **295**, 102–105 (2002).

[19] A. Faraon, A. Majumdar, H. Kim, P. Petroff, and J. Vucković, "Fast electrical control of a quantum dot strongly coupled to a photonic-crystal cavity," Physical Review Letters **104**, 047402 (2010).

[20] D. Pinotsi, J. M. Sanchez, P. Fallahi, A. Badolato, and A. Imamoğlu, "Charge controlled self-assembled quantum dots coupled to photonic crystal nanocavities," Photonics and Nanostructures - Fundamentals and Applications **10**, 256–262 (2012).

[21] K. G. Lagoudakis, K. Fischer, T. Sarmiento, A. Majumdar, A. Rundquist, J. Lu, M. Bajcsy, and J. Vu**c**ković, "Deterministically charged quantum dots in photonic crystal nanoresonators for efficient spin-photon interfaces," New Journal of Physics **15**, 113056 (2013).

[22] R. Bose, T. Cai, K. R. Choudhury, G. S. Solomon, and E. Waks, "All-optical coherent control of vacuum Rabi oscillations," Nature Photonics **8**, 858–864 (2014).

[23] L. Jacak, P. Hawrylak, and A. Wojs, *Quantum Dots* (Springer Science & Business Media, 2013).

[24] R. J. Warburton, C. Schulhauser, D. Haft, C. Schäflein, K. Karrai, J. M. Garcia, W. Schoenfeld, and P. M. Petroff, "Giant permanent dipole moments of excitons in semiconductor nanostructures," Physical Review B **65**, 113303 (2002).

[25] F. Bonaccorso, Z. Sun, T. Hasan, and A. C. Ferrari, "Graphene photonics and optoelectronics," Nature Photonics **4**, 611–622 (2010).

[26] J.-H. Chen, C. Jang, S. Xiao, M. Ishigami, and M. S. Fuhrer, "Intrinsic and extrinsic performance limits of graphene devices on SiO_2," Nature Nanotechnology **3**, 206–9 (2008).

[27] R. R. Nair, P. Blake, A. N. Grigorenko, K. S. Novoselov, T. J. Booth, T. Stauber, N. M. R. Peres, and A. K. Geim, "Fine structure constant defines visual transparency of graphene," Science **320**, 1308 (2008).

[28] A. Majumdar, J. Kim, J. Vuckovic, and F. Wang, "Electrical control of silicon photonic crystal cavity by graphene," Nano Letters **13**, 515–518 (2013).

[29] C. T. Phare, Y.-H. Daniel Lee, J. Cardenas, and M. Lipson, "Graphene electrooptic modulator with 30GHz bandwidth," Nature Photonics **9**, 511–514 (2015).

[30] J. W. Suk, A. Kitt, C. W. Magnuson, Y. Hao, S. Ahmed, J. An, A. K. Swan, B. B. Goldberg, and R. S. Ruoff, "Transfer of CVD-grown monolayer graphene onto arbitrary substrates," ACS Nano **5**, 6916–6924 (2011).

[31] A. Castellanos-Gomez, M. Buscema, R. Molenaar, V. Singh, L. Janssen, H. S. J. van der Zant, and G. A. Steele, "Deterministic transfer of two-dimensional materials by all-dry viscoelastic stamping," 2D Materials **1**, 011002 (2014).

[32] S. Tongay, M. Lemaitre, X. Miao, B. Gila, B. R. Appleton, and A. F. Hebard, "Rectification at graphene-semiconductor interfaces: Zero-gap semiconductor-based diodes," Physical Review X **2**, 011002 (2012).

[33] D. Tomer, S. Rajput, L. J. Hudy, C. H. Li, and L. Li, "Carrier transport in reverse-biased graphene/semiconductor Schottky junctions," Applied Physics Letters **106**, 173510 (2015).

[34] A. Imamoğlu, S. Fält, J. Dreiser, G. Fernandez, M. Atatüre, K. Hennessy, A. Badolato, and D. Gerace, "Coupling quantum dot spins to a photonic crystal nanocavity," Journal of Applied Physics **101**, 081602 (2007).

[35] A. C. Ferrari, J. C. Meyer, V. Scardaci, C. Casiraghi, M. Lazzeri, F. Mauri, S. Piscanec, D. Jiang, K. S. Novoselov, S. Roth, and A. K. Geim, "Raman spectrum of graphene and graphene layers," Physical Review Letters **97**, 187401 (2006).

[36] M. J. Conterio, N. Sköld, D. J. P. Ellis, I. Farrer, D. A. Ritchie, and A. J. Shields, "A quantum dot single photon source driven by resonant electrical injection," Applied Physics Letters **103**, 162108 (2013).

[37] B. Urbaszek, R. J. Warburton, K. Karrai, B. D. Gerardot, P. M. Petroff, and J. M. Garcia, "Fine structure of highly charged excitons in semiconductor quantum dots," Physical Review Letters **90**, 247403 (2003).

[38] A. J. Bennett, R. B. Patel, J. Skiba-Szymanska, C. A. Nicoll, I. Farrer, D. A. Ritchie, and A. J. Shields, "Giant Stark effect in the emission of single semiconductor quantum dots," Applied Physics Letters **97**, 031104 (2010).

[39] T. J. B. M. Janssen, S. Rozhko, I. Antonov, A. Tzalenchuk, J. M. Williams, Z. Melhem, H. He, S. Lara-Avila, S. Kubatkin, and R. Yakimova, "Operation of graphene quantum Hall resistance standard in a cryogen-free table-top system," 2D Materials **2**, 035015 (2015).

[40] K. Novoselov, A. Geim, S. Morozov, D. Jiang, Y. Zhang, S. Dubonos, I. Grigorieva, and A. Firsov, "Electric field effect in atomically thin carbon films," Science **306**, 666–669 (2011).

[41] Y. Zhang, Y.-W. Tan, H. L. Stormer, and P. Kim, "Experimental observation of the quantum Hall effect and Berry's phase in graphene," Nature **438**, 201–204 (2005).

[42] L. A. Ponomarenko, R. Yang, R. V. Gorbachev, P. Blake, A. S. Mayorov, K. S. Novoselov, M. I. Katsnelson, and A. K. Geim, "Density of states and zero Landau level probed through capacitance of graphene," Physical Review Letters **105**, 136801 (2010).

[43] A. Iagallo, S. Tanabe, S. Roddaro, M. Takamura, H. Hibino, and S. Heun, "Tuning of quantum interference in top-gated graphene on SiC," Physical Review B **88**, 235406 (2013).

[44] L. Banszerus, M. Schmitz, S. Engels, M. Goldsche, K. Watanabe, T. Taniguchi, B. Beschoten, and C. Stampfer, "Ballistic transport exceeding 28 μm in CVD grown graphene," Nano Letters **16**, 1387–1391 (2016).

[45] S. Bhandari, G.-H. Lee, A. Klales, K. Watanabe, T. Taniguchi, E. Heller, P. Kim, and R. M. Westervelt, "Imaging cyclotron orbits of electrons in graphene," Nano Letters **16**, 1690–1694 (2016).

[46] J. Hayakawa, K. Muraki, and G. Yusa, "Real-space imaging of fractional quantum Hall liquids," Nature Nanotechnology **8**, 31–35 (2012).

[47] M. König, M. Baenninger, A. G. F. Garcia, N. Harjee, B. L. Pruitt, C. Ames, P. Leubner, C. Brüne, H. Buhmann, L. W. Molenkamp, and D. Goldhaber-Gordon, "Spatially resolved study of backscattering in the quantum spin Hall state," Physical Review X **3**, 021003 (2013).

[48] K. C. Nowack, E. M. Spanton, M. Baenninger, M. König, J. R. Kirtley, B. Kalisky, C. Ames, P. Leubner, C. Brüne, H. Buhmann, L. W. Molenkamp, D. Goldhaber-Gordon, and K. A. Moler, "Imaging currents in HgTe quantum wells in the quantum spin Hall regime," Nature Materials **12**, 787–791 (2013).

[49] N. Paradiso, S. Heun, S. Roddaro, L. Pfeiffer, K. West, L. Sorba, G. Biasiol, and F. Beltram, "Selective control of edge-channel trajectories by scanning gate microscopy," Physica E: Low-dimensional Systems and Nanostructures **42**, 1038–1041 (2010).

[50] N. Paradiso, S. Heun, S. Roddaro, D. Venturelli, F. Taddei, V. Giovannetti, R. Fazio, G. Biasiol, L. Sorba, and F. Beltram, "Spatially resolved analysis of edge-channel equilibration in quantum Hall circuits," Physical Review B **83**, 155305 (2011).

[51] N. Pascher, C. Rössler, T. Ihn, K. Ensslin, C. Reichl, and W. Wegscheider, "Imaging the conductance of integer and fractional quantum Hall edge states," Physical Review X **4**, 011014 (2014).

[52] V. S. Pribiag, A. J. A. Beukman, F. Qu, M. C. Cassidy, C. Charpentier, W. Wegscheider, and L. P. Kouwenhoven, "Edge-mode superconductivity in a two-dimensional topological insulator," Nature Nanotechnology **10**, 593–597 (2015).

[53] E. M. Spanton, K. C. Nowack, L. Du, G. Sullivan, R.-R. Du, and K. A. Moler, "Images of edge current in InAs / GaSb Quantum Wells," Physical Review Letters **113**, 026804 (2014).

[54] C. Tao, L. Jiao, O. V. Yazyev, Y.-C. Chen, J. Feng, X. Zhang, R. B. Capaz, J. M. Tour, A. Zettl, S. G. Louie, H. Dai, and M. F. Crommie, "Spatially resolving edge states of chiral graphene nanoribbons," Nature Physics **7**, 616–620 (2011).

[55] M. Timmermans, T. Samuely, B. Raes, J. Van de Vondel, and V. V. Moshchalkov, "Dynamic visualization of nanoscale vortex orbits," ACS Nano **8**, 2782–2787 (2014).

[56] T. Wagner, D. Köhler, P. Milde, and L. M. Eng, "Probing the local surface potential and quantum capacitance in single and multi-layer graphene," Applied Physics Letters **103**, 023102 (2013).

[57] J. Martin, N. Akerman, G. Ulbricht, T. Lohmann, J. H. Smet, K. von Klitzing, and A. Yacoby, "Observation of electron–hole puddles in graphene using a scanning single-electron transistor," Nature Physics **4**, 144–148 (2007).

[58] J. Berezovsky, M. F. Borunda, E. J. Heller, and R. M. Westervelt, "Imaging coherent transport in graphene (part I): mapping universal conductance fluctuations," Nanotechnology **21**, 274013 (2010).

[59] J. Berezovsky and R. M. Westervelt, "Imaging coherent transport in graphene (part II): probing weak localization," Nanotechnology **21**, 274014 (2010).

[60] M. T. Allen, O. Shtanko, I. C. Fulga, A. R. Akhmerov, K. Watanabe, T. Taniguchi, P. Jarillo-Herrero, L. S. Levitov, and A. Yacoby, "Spatially resolved edge currents and guided-wave electronic states in graphene," Nature Physics **12**, 128–133 (2016).

[61] R. Beams, D. Smith, T. W. Johnson, S.-H. Oh, L. Novotny, and A. N. Vamivakas, "Nanoscale fluorescence lifetime imaging of an optical antenna with a single diamond NV center," Nano Letters **13**, 3807–3811 (2013).

[62] K. Chang, A. Eichler, J. Rhensius, L. Lorenzelli, and C. L. Degen, "Nanoscale imaging of current density with a single-spin magnetometer," Nano Letters **17**, 2367–2373 (2017).

[63] S. Hong, M. S. Grinolds, L. M. Pham, D. Sage, L. Luan, R. L. Walsworth, A. Yacoby, D. Le Sage, L. Luan, R. L. Walsworth, and A. Yacoby, "Nanoscale magnetometry with NV centers in diamond," MRS Bulletin **38**, 155–161 (2013).

[64] P. Wang, Z. Yuan, P. Huang, X. Rong, M. Wang, X. Xu, C. Duan, C. Ju, F. Shi, and J. Du, "High-resolution vector microwave magnetometry based on solid-state spins in diamond," Nature Communications **6**, 6631 (2015).

[65] J.-P. Tetienne, N. Dontschuk, D. A. Broadway, A. Stacey, D. A. Simpson, and L. C. L. Hollenberg, "Quantum imaging of current flow in graphene," Science Advances **3**, 1602429 (2017).

[66] P. F. Fontein, J. A. Kleinen, P. Hendriks, F. A. P. Blom, J. H. Wolter, H. G. M. Lochs, F. A. J. M. Driessen, L. J. Giling, and C. W. J. Beenakker, "Spatial potential distribution in GaAs/ $Al_xGa_{1x}As$ heterostructures under quantum Hall conditions studied with the linear electrooptic effect," Physical Review B **43**, 12090 (1991).

[67] F. Gibelli, L. Lombez, J. Rodière, and J.-F. Guillemoles, "Optical imaging of light-induced thermopower in semiconductors," Physical Review Applied **5**, 024005 (2016).

[68] C. Kastl, M. Stallhofer, D. Schuh, W. Wegscheider, and A. W. Holleitner, "Optoelectronic transport through quantum Hall edge states," New Journal of Physics **17**, 023007 (2015).

[69] Y. Kawano and T. Okamoto, "Imaging of intra- and inter-Landau-level scattering in quantum Hall systems," Physical Review B **70**, 081308 (2004).

[70] R. Knott, W. Dietsche, K. von Klitzing, K. Eberl, and K. Ploog, "Electrooptic imaging of potential distributions in the quantum Hall regime," Semiconductor Science and Technology **10**, 117–126 (1995).

[71] J. N. Moore, J. Hayakawa, T. Mano, T. Noda, and G. Yusa, "Optically imaged striped domains of nonequilibrium electronic and nuclear spins in a fractional quantum Hall liquid," Physical Review Letters **118**, 076802 (2017).

[72] A. J. Shields, M. P. O'Sullivan, I. Farrer, D. A. Ritchie, K. Cooper, C. L. Foden, and M. Pepper, "Optically induced bistability in the mobility of a two-dimensional electron gas coupled to a layer of quantum dots," Applied Physics Letters **74**, 735 (1999).

[73] R. J. F. Van Haren, F. A. P. Blom, W. De Lange, and J. H. Wolter, "Imaging of edge channels in the integer quantum Hall regime by the lateral photoelectric effect," Surface Science **361-362**, 267–269 (1996).

[74] F. Seilmeier, M. Hauck, E. Schubert, G. Schinner, S. Beavan, and A. Högele, "Optical thermometry of an electron reservoir coupled to a single quantum dot in the millikelvin range," Physical Review Applied **2**, 024002 (2014).

[75] F. Haupt, A. Imamoglu, and M. Kroner, "Single quantum dot as an optical thermometer for millikelvin temperatures," Physical Review Applied **2**, 024001 (2014).

[76] B. D. Gerardot, S. Seidl, P. a. Dalgarno, R. J. Warburton, D. Granados, J. M. Garcia, K. Kowalik, O. Krebs, K. Karrai, A. Badolato, and P. M. Petroff, "Manipulating exciton fine structure in quantum dots with a lateral electric field," Applied Physics Letters **90**, 041101 (2007).

[77] T. Nakaoka, Y. Tamura, T. Saito, T. Miyazawa, K. Watanabe, Y. Ota, S. Iwamoto, and Y. Arakawa, "Competing influence of an in-plane electric field on the Stark shifts in a semiconductor quantum dot," Applied Physics Letters **99**, 181109 (2011).

[78] A. Imamoğlu, D. D. Awschalom, G. Burkard, D. P. DiVincenzo, D. Loss, M. Sherwin, A. Small, and A. Imamoğlu, "Quantum information processing using quantum dot spins and cavity QED," Physical Review Letters **83**, 4204 (1999).

[79] D. Heiss, V. Jovanov, M. Bichler, G. Abstreiter, and J. J. Finley, "Charge and spin readout scheme for single self-assembled quantum dots," Physical Review B **77**, 235442 (2008).

[80] L. A. Webster, K. Truex, L.-M. Duan, D. Steel, A. Bracker, D. Gammon, and L. Sham, "Coherent control to prepare an InAs quantum dot for spin-photon entanglement," Physical Review Letters **112**, 126801 (2014).

[81] M. Bayer, G. Ortner, O. Stern, A. Kuther, A. A. Gorbunov, A. Forchel, P. Hawrylak, S. Fafard, K. Hinzer, T. L. Reinecke, S. N. Walck, J. P. Reithmaier, F. Klopf, F. Schäfer, and F. Scha, "Fine structure of neutral and charged excitons in self-assembled In (Ga) As/(Al) GaAs quantum dots," Physical Review B **65**, 195315 (2002).

[82] A. Vamivakas, C.-Y. Lu, C. Matthiesen, Y. Zhao, S. Fält, A. Badolato, and M. Atatüre, "Observation of spin-dependent quantum jumps via quantum dot resonance fluorescence," Nature **467**, 297–300 (2010).

[83] L. Allen and J. H. Eberly, *Optical Resonance and Two Level Atoms* (John Wiley & Sons, Inc., 1975).

[84] M. Citron, H. Gray, C. Gabel, and C. S. Jr, "Experimental study of power broadening in a two-level atom," Physical Review A **16**, 1507 (1977).

[85] K. S. Novoselov, A. Mishchenko, A. Carvalho, and A. H. Castro Neto, "2D materials and van der Waals heterostructures," Science **353**, aac9439 (2016).

[86] A. Kormányos, V. Zólyomi, N. D. Drummond, and G. Burkard, "Spin-orbit coupling, quantum dots, and qubits in monolayer transition metal dichalcogenides," Physical Review X **4**, 011034 (2014).

[87] K. F. Mak, K. He, J. Shan, and T. F. Heinz, "Control of valley polarization in monolayer MoS_2 by optical helicity," Nature Nanotechnology **7**, 494–498 (2012).

[88] A. Splendiani, L. Sun, Y. Zhang, T. Li, J. Kim, C.-Y. Chim, G. Galli, and F. Wang, "Emerging photoluminescence in monolayer MoS_2," Nano Letters **10**, 1271–1275 (2010).

[89] Q. H. Wang, K. Kalantar-Zadeh, A. Kis, J. N. Coleman, and M. S. Strano, "Electronics and optoelectronics of two-dimensional transition metal dichalcogenides," Nature Nanotechnology **7**, 699–712 (2012).

[90] A. K. Geim and I. V. Grigorieva, "Van der Waals heterostructures," Nature **499**, 419–425 (2013).

[91] A. Pospischil, M. M. Furchi, and T. Mueller, "Solar-energy conversion and light emission in an atomic monolayer p– n diode," Nature Nanotechnology **9**, 257–261 (2014).

[92] C.-H. Lee, G.-H. Lee, A. M. van der Zande, W. Chen, Y. Li, M. Han, X. Cui, G. Arefe, C. Nuckolls, T. F. Heinz, J. Guo, J. Hone, and P. Kim, "Atomically thin p–n junctions with van der Waals heterointerfaces," Nature Nanotechnology **9**, 676–681 (2014).

[93] K. M. Goodfellow, R. Beams, C. Chakraborty, L. Novotny, A. N. Vamivakas, K. E. M. G. Oodfellow, R. Y. A. N. B. Eams, C. H. C. Hakraborty, L. U. N. Ovotny, and A. N. V. Amivakas, "Integrated nanophotonics based on nanowire plasmons and atomically thin material," Optica **1**, 149–152 (2014).

[94] B. W. H. Baugher, H. O. H. Churchill, Y. Yang, and P. Jarillo-Herrero, "Optoelectronic devices based on electrically tunable p-n diodes in a monolayer dichalcogenide," Nature Nanotechnology **9**, 262–267 (2014).

[95] J. S. Ross, P. Klement, A. M. Jones, N. J. Ghimire, J. Yan, D. G. Mandrus, T. Taniguchi, K. Watanabe, K. Kitamura, W. Yao, D. H. Cobden, and X. Xu, "Electrically tunable excitonic light-emitting diodes based on monolayer WSe_2 p–n junctions." Nature Nanotechnology **9**, 268–272 (2014).

[96] H. Zeng, J. Dai, W. Yao, D. Xiao, and X. Cui, "Valley polarization in MoS_2 monolayers by optical pumping," Nature Nanotechnology **7**, 490–493 (2012).

[97] M. B. Lundeberg and J. A. Folk, "Harnessing chirality for valleytronics," Science **346**, 422–423 (2014).

[98] C. Chakraborty, L. Kinnischtzke, K. M. Goodfellow, R. Beams, and A. N. Vamivakas, "Voltage-controlled quantum light from an atomically thin semiconductor," Nature Nanotechnology **10**, 507–511 (2015).

[99] A. Srivastava, M. Sidler, A. V. Allain, D. S. Lembke, A. Kis, and ImamoğluA., "Optically active quantum dots in monolayer WSe_2," Nature Nanotechnology **10**, 491–496 (2015).

[100] M. Koperski, K. Nogajewski, A. Arora, V. Cherkez, P. Mallet, J.-Y. Veuillen, J. Marcus, P. Kossacki, and M. Potemski, "Single photon emitters in exfoliated WSe_2 structures," Nature Nanotechnology **10**, 503–506 (2015).

[101] Y.-M. He, G. Clark, J. Schaibley, Y. He, M.-C. Chen, Y.-J. Wei, X. Ding, Q. Zhang, W. Yao, X. Xu, C.-Y. Lu, and J.-W. Pan, "Single quantum emitters in monolayer semiconductors," Nature Nanotechnology **10**, 497–502 (2015).

[102] A. M. Jones, H. Yu, N. J. Ghimire, S. Wu, G. Aivazian, J. S. Ross, B. Zhao, J. Yan, D. G. Mandrus, D. Xiao, W. Yao, and X. Xu, "Optical generation of excitonic valley coherence in monolayer WSe_2," Nature Nanotechnology **8**, 634–638 (2013).

[103] K. He, N. Kumar, L. Zhao, Z. Wang, K. F. Mak, H. Zhao, and J. Shan, "Tightly bound excitons in monolayer WSe_2," Physical Review Letters **113**, 026803 (2014).

[104] G. Wang, L. Bouet, D. Lagarde, M. Vidal, A. Balocchi, T. Amand, X. Marie, and B. Urbaszek, "Valley dynamics probed through charged and neutral exciton emission in monolayer WSe_2," Physical Review B **90**, 075413 (2014).

[105] D. Chen, G. R. Lander, G. S. Solomon, and E. B. Flagg, "Polarization-dependent interference of coherent scattering from orthogonal dipole moments of a resonantly excited quantum dot," Physical Review Letters **118**, 037401 (2017).